NTNU

Norwegian University of
Science and Technology

All oxide thermoelectric device based on $Ca_{0.931}Mn_{0.98}Ta_{0.02}O_{3-\delta}$-$Ca_3Co_4O_9$ pn-junction

Sara Hizon Kolobekken

Chemical Engineering and Biotechnology
Submission date: June 2017
Supervisor: Mari-Ann Einarsrud, IMA
Co-supervisor: Kjell Wiik, IMA
Nikola Kanas, IMA

Norwegian University of Science and Technology
Department of Materials Science and Engineering

Preface

This thesis is submitted to the Norwegian University of Science and Technology (NTNU), as part of the requirements for the degree of Master of Science. The work presented in this thesis has been carried out at the Department of Materials Science and Engineering at NTNU between 20 January and 16 June, 2017. Professor Mari-Ann Einarsrud has supervised the work, and Ph.D. candidate Nikola Kanas and Professor Kjell Wiik have served as co-supervisors.

I would like to thank my supervisor Professor Mari-Ann Einarsrud and co-supervisors PhD Nikola Kanas and Professor Kjell Wiik for valuable guidance and for sharing their knowledge through out this work. Always motivating me and guiding me on how to approach scientific problems in order to obtain the best results has helped me immensely. A special thanks to Nikola Kanas for conducting measurements of the thermoelectric output of the device at Leibniz University in Hannover, Germany.

I would also like to acknowledge the rest of my co-workers associated with the Ceramics group. The sharing of experiences and knowledge is tremendous and I feel I have learned a great deal over the past semester. Further, I would like to thank the technical staff at the department, for giving me equipment training and helping me with various practical problems.

Financial support from The Research Council of Norway under the program Nano2021 to the project (Number 228854) "Thermoelectric materials: Nanostructuring for improving the energy efficiency of thermoelectric generators and heat-pumps" (THELMA) conducted by NTNU, UiO, SINTEF, FFI, UiS and UiA, is gratefully acknowledged.

Abstract

Metal oxides are promising thermoelectric (TE) material candidates for TE modules operational in a range of 300-1200 K in air. In this work a TE oxide module was fabricated by co-sintering the p-type material $Ca_3Co_4O_9$ (CCO), the n-type material $Ca_{0.931}Mn_{0.98}Ta_{0.02}O_{3-\delta}$ (CMTO) and the insulator material $LaAlO_3$ (LAO) by the spark plasma sintering (SPS) method.

Nanosized spray pyrolysed powders of CCO, LAO and CMTO were spark plasma sintered (SPS) for 2 min at 880 ℃. Sub-micrometer grain sizes were observed for the CMTO and LAO ceramics, and they reached a density of of 68 % and 41 % of the theoretical density respectively. The $Ca_3Co_4O_9$-derived ceramic is a multi-phase composite due to partial decomposition of the starting powder during sintering. The ceramic reached a density of 96% and had a grain size of $\sim$ 1.2 μm. Increased residence time in the SPS showed little influence on the grain size.

By studying diffusion couples of two and two materials sintered in SPS at 850 ℃, chemical interaction was evidenced by the formation of reaction layers at the different interfaces. The thickness of the layers varied in the range of 2 - 55 μm across the samples. Energy dispersive X-ray spectroscopy mapping in a scanning electron microscope (SEM) revealed that $Ca_3(Co_xMn_{2-x})O_6$ was formed at the interface between CCO and CMTO, while decomposition of CCO resulted in a cobalt oxide layer the interface between CCO and LAO. Increased residence time did not appear to have a significant effect on the thickness of the formed layers, which is promising in terms of the rough conditions a TE device is subjected to during operation.

SEM investigations of TE couples sintered at a temperature of 880 ℃ revealed formation of micro cracks in the devices due to thermal expansion mismatch between the materials. The cracks are detrimental to the mechanical strength and stability of the device. The cracking was most prominent in the CMTO phase, and the correlation between CMTO thickness and tensile stresses in the sample was investigated through theoretic calculations. It was found that an increase in thickness caused a decrease in the stresses developed.

The TE device consisting of a single TE couple was characterized at two different temperatures and achieved a maximum electrical power output of 1.9 mW when the hot side temperature was 900 ℃ and a temperature difference of 130 ℃ was applied.

Sammendrag

Metalloksider er lovende materialer til bruk i termoelektriske (TE) moduler som kan benyttes mellom 300-1000 K i luft. I dette arbeidet har en TE modul blitt produsert ved å co-sintre p-type $Ca_3Co_4O_9$ (CCO), n-type $Ca_{0.931}Mn_{0.98}Ta_{0.02}O_{3-\delta}$ (CMTO) og isolator materialet $LaAlO_3$ (LAO) ved hjelp av spark plasma sintringsmetoden (SPS).

Spray pyrolisert pulver av CCO, CMTO og LAO ble spark plasma sintret i 2 min ved 880 ℃. Kornstørrelser på under 1 µm ble observert for CMTO og LAO, og materialene oppnådde en tetthet på henholdsvis 68 % og 41% av den teoretiske. $Ca_3Co_4O_9$ dekomponerte delvis under sintring og dannet en multi-fase kompositt. Keramen oppnådde en tetthet på 96% og hadde en kornstørrelse på $\sim$ 1.2 µm. Økt oppholdstid i SPS hadde liten påvirkning på kornstørrelsen.

Ved å studere diffusjonspar av to og to materialer sintret i SPS ved 850 ℃ i 2 min, ble det påvist kjemisk interaksjon mellom materialene gjennom dannelsen av reaksjonslag på de forskjellige grenseflatene. Tykkelsen på lagene varierte mellom 2 - 55 µm gjennom prøvene. Energidispersiv spektroskopi undersøkelser i skanning elektronmikroskop (SEM) viste at $Ca_3(Co_xMn_{2-x})O_6$ ble dannet på grenseflaten mellom CMTO og CCO, mens dekomponering av CCO førte til dannelsen av et Co_3O_4-lag på grenseflaten mellom CCO og LAO. Økt oppholdstid i SPS maskinen hadde ikke en betydelig effekt på tykkelsen av de dannede lagene, noe som er positivt med tanke på de tøffe forholdene en TE generator utsettes for under bruk.

SEM undersøkelser av TE par sintret ved 880 ℃ avdekket dannelsen av mikrosprekker i modulene, forårsaket av forskjeller i termisk utvidelseskoeffisient mellom materialene. Dette er ødeleggende for den mekaniske styrken og stabiliten av modulen. Sprekkene var spesielt fremtredene i CMTO fasen, og korrelasjonen mellom tykkelsen av CMTO og strekkspenninger i materialet ble undersøkt gjennom teoretiske beregninger. Beregningene viste at en økning i tykkelsen førte til en senkning i utviklet spenning.

Den termoelektriske modulen som bestod av et enkelt TE par ble karakterisert ved to forskjellige temperaturer og oppnådde maksimal elektrisk output på 1.9 mW når den varme siden hadde en temperatur på 900 ℃ og en temperaturforskjell på 130 ℃ ble påført.

Contents

Chapter 1

Background

1.1 Motivation

The global energy demand is constantly increasing. In order to meet this energy demand the world is relying on fossil fuels. However, somber forecasts predict that the earth will run out of petrol, natural gas and uraninum in 40 to 60 years, and out of coal in 200 years. [1] Also, CO_2 exhaust in these processes contribute to the green house effect. Climate scientists have documented a rise in average surface temperature of 0.9 ℃ in the time period 1881 to 2012, which can have damaging effects if the increase in temperature were to continue.[2] Such damage would include increased extinction rate of various plant and animal species, shifts in patterns of agriculture and rising sea levels.

The challenges that lie ahead have generated an enormous and not to mention necessary focus on the development of regenerative energy sources. Thermoelectric phenomena are expected to play an increasingly important role in meeting the future energy demand. Thermoelectric (TE) devices make it possible to convert both solar energy and waste heat directly into electricity. Heat represents an abundant and sustainable energy source and as the waste heat from many industrial processes often go unused, it is a field with a large potential for energy saving. [3]

A thermoelectric generator (TEG) is a device that consists of a large number of thermoelectric couples sandwiched between two ceramic substrates. Each thermocouple consists of a p- and a n-type material, an insulator and a connector joining the two legs. The TE couples are connected

electrically in a series and thermally in parallel between the two ceramic plates to form a module as illustrated in Figure 1.1. It produces a voltage when there exists a temperature difference between the hot and the cold side of the device because of the Seebeck effect. [4] TE devices have several advantages like being small and lightweight, having no movable parts, being acoustically silent and "electrically" quiet, as well as being low maintenance and environmentally friendly. [5]

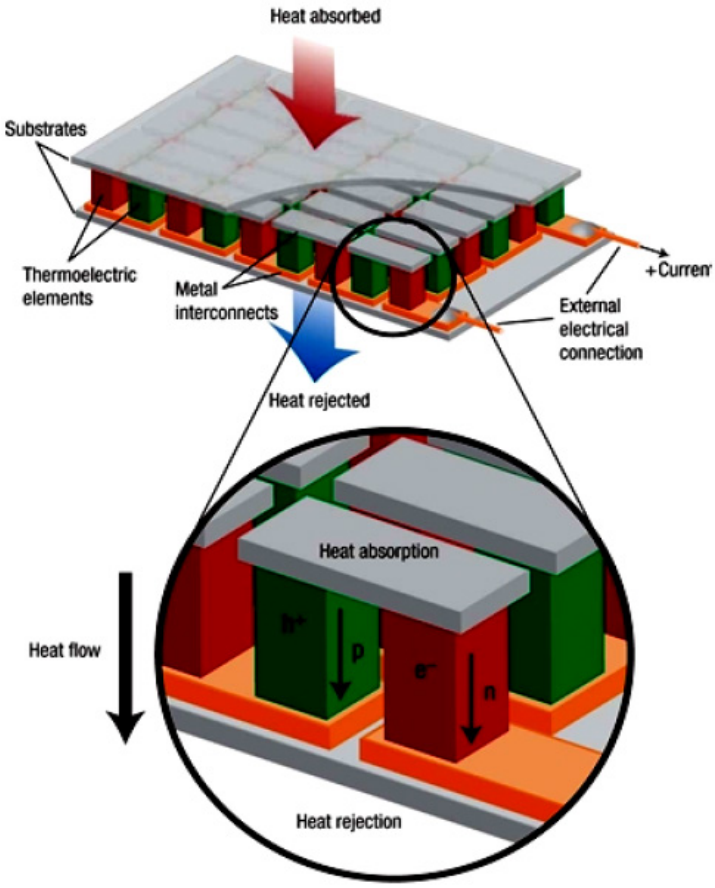

Figure 1.1: Shematic illustration of a TE-device.[6]

Most commercialized TEGs use state of the art materials like Bi_2Te_3, Si–Ge and Pb-Te based alloys.[7]. But shortages of these conventional materials, such as surface oxidation and vaporization at high temperature, and containing harmful or scarce elements, have limited widespread applications of these materials. In addition to this, the conventional set-up shown in Figure 1.1

limits the maximum operating temperature of the TEG due to decomposition of the metallic connectors joining the thermocouples. An interest has therefore grown for the development of an all oxide thermoelectric generator (Figure 1.2). The resulting oxide pn-junction from this alternative set-up will make it possible to operate the TEG at much higher temperatures than conventional TEGs. Possible material candidates for such high-temperature applications are $Ca_3Co_4O_9$ [8], $NaCoO_2$ [9], Li-doped NiO [10], $CaMnO_3$ [11], and $SrTiO_3$ [12], because of their promising TE properties, high chemical stability and environmental friendly nature. [5]

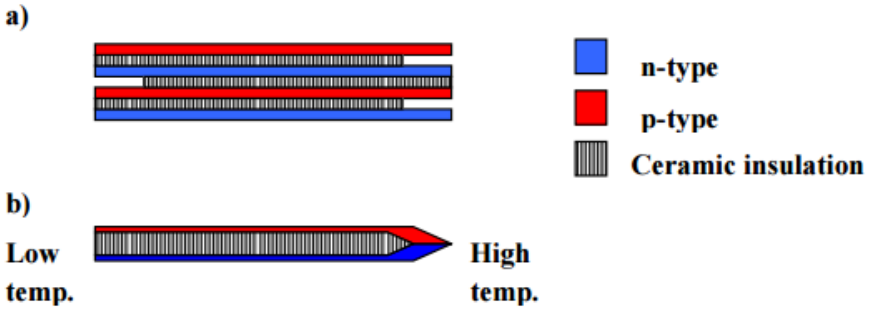

Figure 1.2: Schematic illustration of set-up of an all oxide thermoelectric generator, (a) shows stacking of p- and n-type materials with ceramic insulator in between prior to lamination and co-sintering, while (b) shows one co-sintered n- and p-couple resulting in a pn junction. [13]

1.2 Aim of work

The focus of this thesis is to develop a technology for the preparation of an all-oxide thermoelectric device using spark plasma sintering (SPS). In the family of oxide based thermoelectric materials, the systems of perovskite type structures of $CaMnO_3$ (n-type) and layered cobaltite structures of $Ca_3Co_4O_9$ (p-type) have shown promising thermoelectric properties. Hence, for this work the materials of choice are $Ca_{0.931}Mn_{0.98}Ta_{0.02}O_{3-\delta}$ (CMTO) and $Ca_3Co_4O_9$ (CCO). $LaAlO_3$ (LAO) is chosen as the insulating material. Non-stoichiometric CMTO is chosen as calcium deficiency introduces a secondary spinell phase $CaMn_2O_4$ (Marokite), which improves the thermoelectric properties of the perovskite material by lowering the thermal conductivity. [14]

The motivation behind the work is the development of an all-oxide thermoelectric generator

for application at high temperatures. For all-oxide thermoelectric devices, the properties of the resulting pn-junction will be of great significance for the performance the device. By using SPS, a very short sintering time is possible and some of the challenges related to traditional co-sintering can be minimized.

The powders used in this work are prepared by spray pyrolysis and provided by CerPoTech. The powders will be characterized with respect to morphology and phase purity. Diffusion couples of the materials will be sintered in order to evaluate phase compatibility and the formation of secondary phases, interdiffusion between the materials and reaction kinetics will be discussed. Finally, a thermoelectric device will be prepared and characterized with respect microstructure, interface properties as well as thermoelectric effect. Characterization of the thermoelectric output will be done in collaboration with partners. Characterization methods will include X-ray diffraction (XRD), scanning electron microscopy (SEM) and energy dispersive X-ray spectroscopy (EDS).

Chapter 2

Introduction

2.1 Thermoelectric effects

The conduction of heat and the conduction of electricity are closely linked. How they affect each other is described through the phenomena of thermoelectric effects. Thermoelectric effects is the direct conversion of temperature difference to a voltage or vice versa. All materials that contain mobile charge carriers can exhibit thermoelectric effects during heating. [4] The term encompasses the following three identified effects; Seebeck effect, Peltier effect and Thomson effect.

2.1.1 Seebeck effect

The German physicist Thomas J. Seebeck discovered the first thermoelectric effect in 1821. In a circuit made up of two dissimilar conducting materials, with the two junctions exposed to different temperatures, an electromotive force, or voltage, arises. This force is proportional to the temperature difference between the junctions. [4] The effect is generally observed by breaking the circuit and observing the voltage generated using a potentiometer. The set-up is illustrated in Figure 2.1.

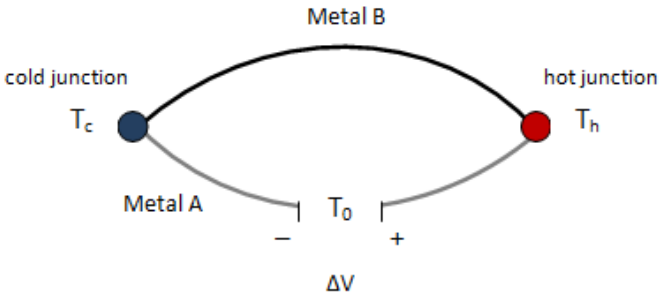

Figure 2.1: Shematic illustration of The Seebeck effect

The voltage generated, ΔV_{AB}, is given by:

$$\Delta V_{AB} = \Sigma_{AB} \Delta T \tag{2.1}$$

where Σ_{AB} is the *thermoelectric power* or overall *Seebeck coefficient* and ΔT is the temperature difference between the junctions. The overall Seebeck coefficient is the difference between the Seebeck coefficients of the materials forming the junction.

2.1.2 Peltier effect

The complementary effect of the Seebeck effect is the Peltier effect. It was discovered in 1834 by the French physicist Jean-Charles Athanase Peltier. It is described in the following manner: when a current is maintained in a circuit consisting of two dissimilar conductors, it will result in a temperature rise of one junction and a temperature drop of the other depending on the current flow. See Figure 2.2. The amount of heat produced or absorbed, ΔQ, is given by:

$$\Delta Q = \Pi_{AB} I t \tag{2.2}$$

where Π_{AB} is the *Peltier coefficient*, I is the current and t is the time.[4]

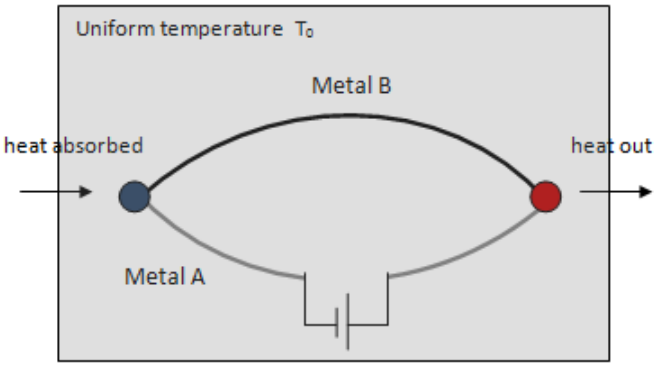

Figure 2.2: Schematic illustration of the Peltier effect

2.1.3 Thomson effect

A British physicist named William Thomson (Lord Kelvin) discovered the last thermoelectric effect in 1854. He discovered that if a temperature difference exists between any two points of a conducting rod, heat is either absorbed or liberated along the length of the rod depending on the direction of current and material. The amount of heat energy absorbed or liberated, ΔQ, is given by:

$$\Delta Q = \tau I t \Delta T \tag{2.3}$$

where τ is the *Thomson coefficient*, I is the current flowing for a time t, and ΔT is the temperature difference between the points of measurements. [4]

2.2 Thermoelectric generators

There are several advantages with the use of TEGs. Thermoelectric devices are solid state mechanics, which means they have no moving parts. This reduces their susceptibility to mechanical failure, offering high reliability and allowing for prolonged periods of operation without much maintenance. They are also reasonably small in size and weight and can be used in an adverse environment, as well as over a large temperature range. However, the widespread application of thermoelectric modules has been limited by a relatively low conversion efficiency ($sim5\%$) [15]

The operating principle of the thermoelectric generator (TEG) is based on the Seebeck effect described in Section 2.1. Specifically, when a temperature gradient is maintained across a thermoelectric material, the carriers seek a state with minimal chemical potential energy, thus diffusing to the cold side generating an electric potential. A thermoelectric module requires two thermoelectric materials to function: a n-type semiconductor (negatively charged, charge carriers are electrons) and a p-type semiconductor (positively charged, charge carriers are holes). The n- and p-type semiconductors form a thermoelectric couple. The thermocouples are linked together by strips of a good electrical conductor, such as copper, and are held together with insulating plates that conduct heat well. A TEG can consist of an array of several to hundreds of p-type and n-type thermocouples joined together electrically in series and thermally in parallel between a common heat source and heat sink. The temperature difference between the two sides of the device makes each thermocouple generate an electric potential and sum of these potential is referred to as the device's electromotive force. [16] The essential features of such a thermoelectric module are illustrated in Figure 2.3.

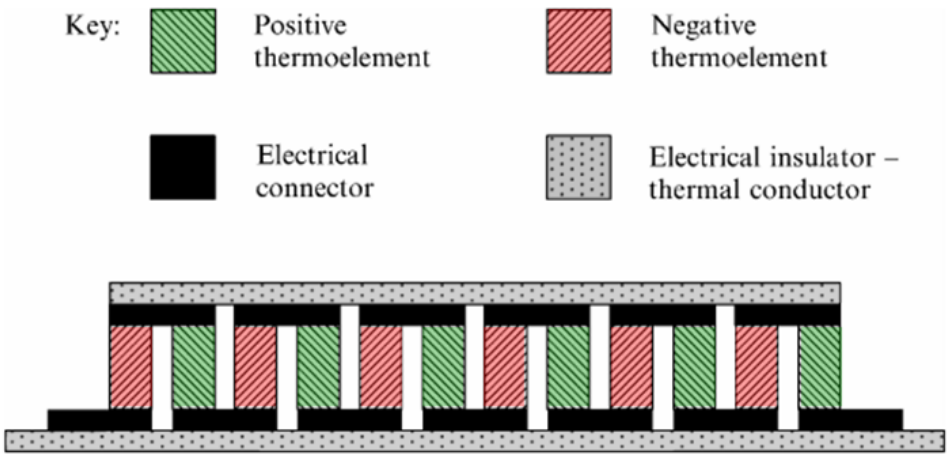

Figure 2.3: Schematic representation of a thermoelectric module. [16]

The device can also be used for the inverse process, as a thermoelectric cooler. When a current is supplied to this device, it produces the difference in temperatures between its two sides, also know as the Peltier effect.

A thermoelectric module for power generation will be subjected to large thermally induced stresses and strain for long periods of time, due to operation in a large temperature gradient. It must also withstand thermal cycles, which can cause problems with mechanical fatigue. Using TE devices to recover industrial waste heat sets high demands in terms of robustness and efficiency of devices. Overcoming challenges with material development and system engineering is necessary if these devices are to provide the heat transfer and power output required in industrial applications.

2.3 Characterization of thermoelectric generators

2.3.1 Thermoelectric figure of merit

In 1911, the physicist Altenkirch discovered that the thermoelectric properties of a material are directly controlled by the electrical conductivity, σ, the thermal conductivity, κ and the Seebeck coefficient, α. This correct relationship later developed and was denoted the materials thermoelectric figure of merit, ZT. It was presented by Abram Fediriwuch Ioffe in 1949 and is given in Equation 2.4. [17]

$$ZT = \frac{\alpha^2 \sigma}{\kappa} T \tag{2.4}$$

From the definition of ZT a good TE material must have a low thermal conductivity and a high electrical conductivity and Seebeck effect. All three properties are functions of charge carrier concentration. As seen in Figure 2.4 the Seebeck coefficient decreases with increasing carrier concentration, while the electrical conductivity increases. The two are not independent, and hence the materials TE power factor, $\alpha^2\sigma$, is optimized by adjusting the carrier concentration. The maxiumum power factor is achieved with a carrier concentration of approximately $\sim 10^{19}$ cm^{-3}.

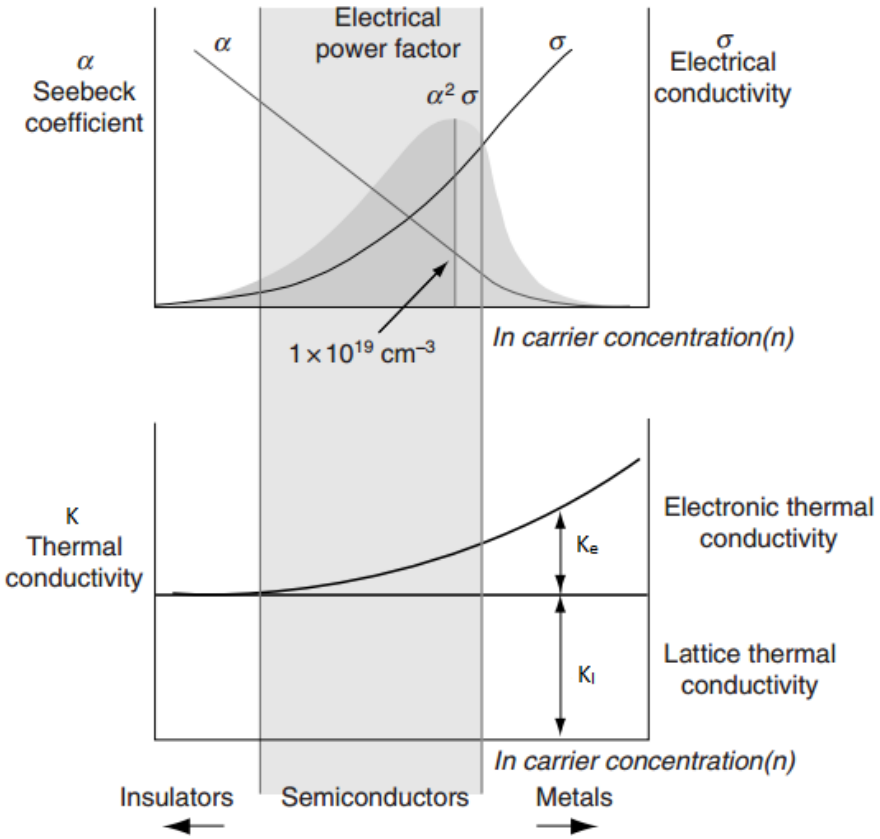

Figure 2.4: Schematic illustration of the dependency of electrical conductivity, thermal conductivity and Seebeck coefficient on carrier concentration. [18]

The thermal conductivity of the material has two contributions, one from electrons and holes transporting heat, κ_e, and one from phonons travelling through the crystal lattice, κ_l. [6] The materials thermal conductivity can therefore be described as:

$$\kappa = \kappa_l + \kappa_e \tag{2.5}$$

Phonons and charge carriers can undergo scattering due to other phonons, lattice defects, impurities, electrons, grain boundaries and interfaces. [19]. The electronic contribution also increases with carrier concentration, as seen in Figure 2.4. Thus, considering the behaviour of the

three material properties the figure of merit optimizes at carrier concentrations corresponding to that of semi-conductors. Semi-conductors are for this reason the most researched TE materials.

2.3.2 Energy conversion efficiency and electrical power output

A generator is like all other heat engines governed by the laws of thermodynamics. Ideally, the generator would have no heat loss during operation, and the efficiency would be defined as the ratio between the electrical power delivered to the load and the heat absorbed at the hot junctions. An expression for the thermoelectric efficiency of a generator can be derived by considering the simplest generator consisting of a single thermocouple with p- and n-type semiconducting materials, shown in Figure 2.5.

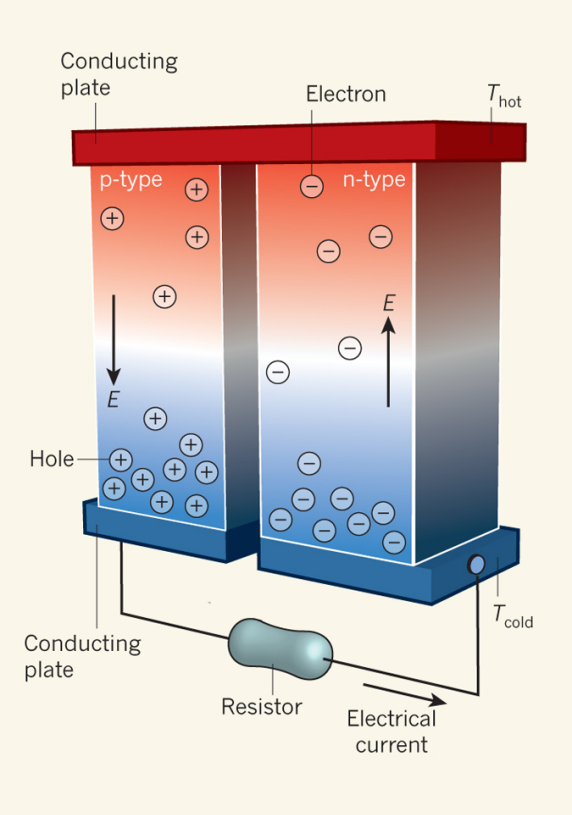

Figure 2.5: Illustration of a simple thermoelectric generator. [20]

Assuming that the Seebeck coefficients, thermal conductivities and electrical conductivities are constant within the material at a given temperature, and that the contact resistance at the hot and cold junction is negligible, the efficiency, η, can be given by Equation 2.6.

$$\eta = \frac{\Delta T}{T_h} = \frac{\sqrt{1+ZT}-1}{\sqrt{1+ZT}+\frac{T_c}{T_h}} \tag{2.6}$$

ΔT is the temperature difference between the junctions, T_h and T_c is the temperature at the hot and cold side of the junction respectively and ZT is the devices figure of merit. The efficiency is thermodynamically limited by the Carnot efficiency, $\frac{\Delta T}{Th}$. [6]

The power output, P, of the module can be expressed as

$$P = \frac{U_{\mathrm{OC}}^2}{4 \cdot R_{load} \cdot \frac{U_{\mathrm{OC}}-U_{\mathrm{load}}}{U_{\mathrm{load}}}} \tag{2.7}$$

where U_{OC} is the open circuit voltage, R_{load} is the load resistance in the external circuit, U_{load} is the load voltage and R_{device} is the internal resistance of the device. The maximum electrical power output, P_{max}, show in Equation 2.8 is a load-resistance dependent parameter and is maximized when $R_{load} = R_{device}$ and $U_{load} = \frac{1}{2}U_{\mathrm{OC}}$. [21]

$$P_{max} = \frac{U_{OC}^2}{4R_{device}} \tag{2.8}$$

2.4 Thermoelectric materials

In 1945, Ioffe developed a theory that semiconductors resulting from groups IV-VI in the periodic system will have the best thermoelectric properties. [22] The principle said that these heavily doped semi-conductors with a carrier concentration, n, on the order of 10^{18} cm^{-3} - 10^{20} cm^{-3} and with band gap of $\sim 10 k_{\mathrm{B}}\mathrm{T}$ would exhibit high figures-of-merit. [23] This lead to the further research and discovery of several compounds exhibiting good thermoelectric properties. From the 1960s tellurides have been extensively studied and optimized, and remain state-of-the-art materials to this day.

These well-established thermoelectric materials can be divided into three categories depending on which temperature range they can operate on. Bitmuth telluride and its alloys are known

to have high figures-of-merit, with a maximum operating temperature of around 177 ℃. Alloys based on lead tellurides generally have lower values for the figures of merit and can operate at temperatures up to 727 ℃. The silicon germanium alloys have the lowest figures-of-merit and a upper operating temperature of 1027 ℃. [7]. Obtained values for the figure-of-merits of these materials can be seen in Table 2.1.

Table 2.1: Maxium obtaines values for figure-of-merit for both n- and p-type elements for state-of-the-art commercial TE materials.

Material	**Maximum operating temperature**	**Maximun obtained ZT-values [23]**
Bi-Te based alloys	177 ℃	n-type: 0.97 at 50 ℃ p-type: 1.35 at 100 ℃
Pb-Te based alloys	727 ℃	n-type: 1.25 at 400 ℃ p-type: 1.5 at 600 ℃
Si-Ge based alloys	1027 ℃	n-type: 0.96 at 880 ℃ p-type: 0.6 at 750 ℃

Although these materials are the most commercialized and used in practical applications, a large amount of effort has gone into the development and research of alternative materials, due to problems with their practical application. Their constituents will easily decompose, vaporize or melt at high temperatures. They contain toxic elements like Pb, Te and Sb which should be avoided as far as possible due to their hazardous nature and negative effect on the environment, as well being low in abundance in nature.

Next generation thermoelectric materials

In the search of next generation thermoelectric materials, there were two research approaches developed in the 1990s. One focused on the use of advanced bulk thermoelectric materials, while the other focused on utilizing low-dimensional materials. The advanced bulk materials approach investigated materials which contained heavy-ion species with large vibrational amplitudes at partially filled structural sites. These heavy-ion centers work like effective phonon scattering sites,

which reduce the lattice thermal conductivity. Among these materials partially filled skutterudites based on alloys of $CoSb_3$, so called phonon-glass electron crystal (PGEC) materials, are the most prominent. [24]

The other approach focuses on the use of low-dimensional structures like quantum wells (2D structures), quantum wires (1D structures) and quantum dots (0D structures). The idea is that as the dimensionality and length scale decreases, new physical phenomena create new opportunities to vary S, κ and σ, and hence opportunities of enhancement of the figure-of-merit arises. The introduction of nanoscale constituent also introduces many new interfaces which scatter phonons more effectively than electrons. [24] This recognition has lead to studies of individual nanostructures like nanowires and superlattices, and studies on bulk nanostructures. The figure-of-merit over the temperature range of 0 - 1000 ℃ for some of the current TE materials is depicted in Figure 2.6.

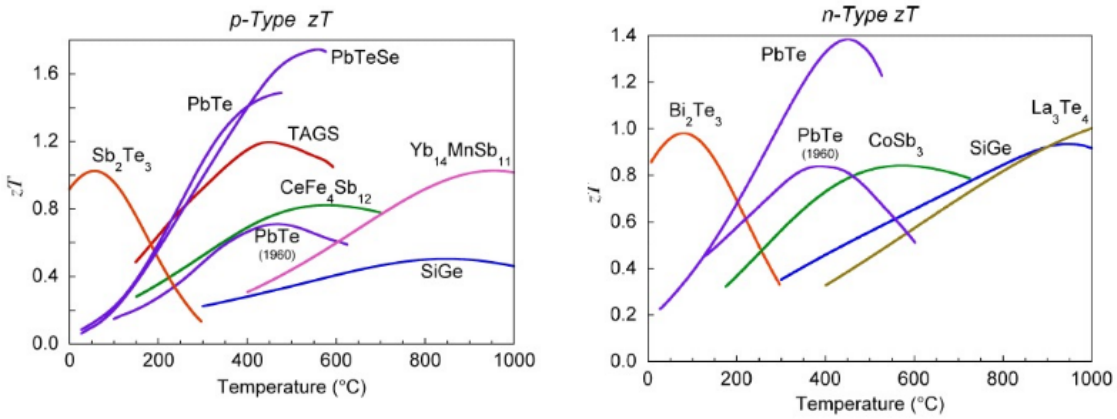

Figure 2.6: Figure of merit (ZT) for current TE materials (p-type and n-type) over the temperature range of 0–1000°C [25]

2.5 Thermoelectric oxides

According to Ioffe's theory, metal oxides are poor candidates for thermoelectric applications. They have ionic bonds, which causes them to have smaller orbital overlap than covalent inter-metallic alloys. These polarized metal-oxide bonds gives a strong tendency of carrier localization with a

carrier mobility much lower than for the case of covalent bonds. However, the lattice thermal conductivity is high, caused by higher vibrational frequencies in the crystal lattice due to the small atomic mass of oxygen and large bonding energy. [23]

Despite having lower ZT than state-of-the-art materials, oxides have several advantages making them viable candidates for TE applications. Firstly, oxides are more suited for high temperature applications, usually above 1000 ℃ due to their chemical and structural stability (Figure 2.7 (a)). This allows for a larger thermal gradient to be applied across the materials, resulting in a high Carnot efficiency in Equation (2.6). Secondly, their chemical versatility and structural features offer good flexibility in terms of structural and compositional tailoring. Finally, their low cost utilizing naturally abundant elements, easy manufacturing and environmental friendliness makes them attractive for large-scale applications. (Figure 2.7 (b)).[23][26]

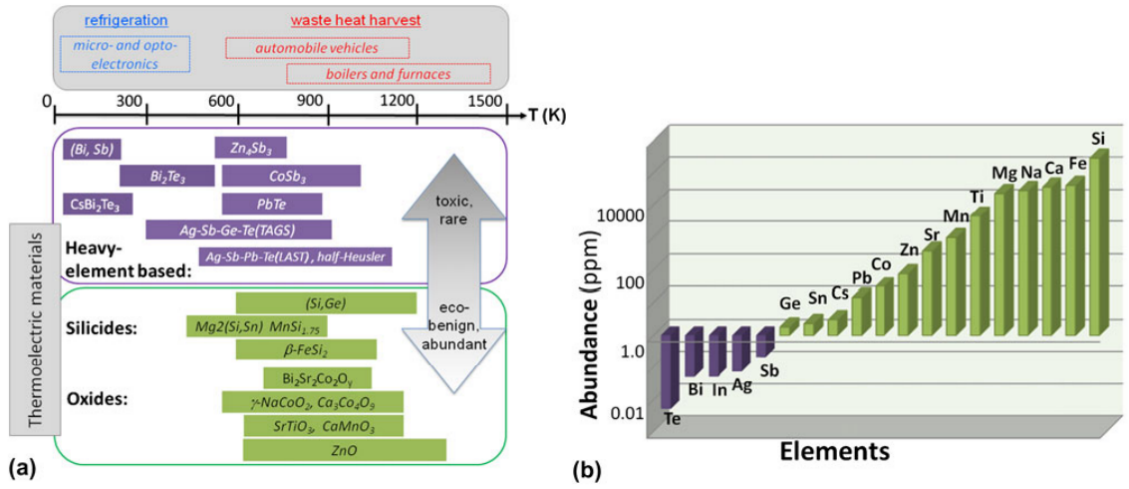

Figure 2.7: (a) Overview of the application of some TE materials in terms of temperature range and abundance and environmental friendliness. (b) Relative abundance of the chemical elements used in TE materials. [26]

A breakthrough for oxide materials was in 1997, when Tarasaki et al. [27] presented $NaCoO_2$ as a potential thermoelectric material. The material had a large positive Seebeck coefficient and despite α being lower than the value obtained for many of the other traditional TE materials ($\alpha \approx 100\ \mu V\ K^{-1}$ at 300 K), $NaCoO_2$ also had a low resistivity to make the power factor comparable. The

low dimension cobaltites that include $NaCoO_2$ and $Ca_3Co_4O_9$ have attracted considerable attention because of the co-existence of large Seebeck coefficient and low lattice thermal conductivity.

However, the development of n-type oxide-based bulk materials is far behind the p-type materials, such as Na_xCoO_2, and $Ca_3Co_4O_9$. [28] Among the n-type oxides materials perovskite-type strontium titanate, $SiTiO_3$ and perovskite-type calcium manganese oxide, $CaMnO_3$ have shown promising TE properties. At room temperature $SiTiO_3$ has a power factor comparable to that of Bi_2Te_3. A rather high thermal conductivity of 8 W $m^{-1}K^{-1}$, results in a low ZT of ~ 0.08 at room temperature. The addition of lanthanum increases the electrical conductivity and Seebeck coefficient with only small changes in thermal conductivity and thus improves the figure of merit. The thermal conductivity of $SiTiO_3$ is high, but a large effective mass and low mobility makes it possible to reduce the lattice conductivity without affecting the electrical conductivity. [16] Compared to traditional state-of-the-art materials, pure $CaMnO_3$ shows a low performance due to its low electric conductivity. The σ of pure $CaMnO_3$ is just $\sim$10 S/cm and ZT is less than 0.04 at 900 K. [29] However, doping has proven to enhance the conductivity of $CaMnO_3$ and the most commonly used dopants are ytterbium on the calcium site and niobium on the manganese site.

2.5.1 Calcium manganite

Perovskite-based oxides are well know for a variety of physical properties such as ferroelectricity, colossal magnetoresistance, high-temperature superconductivity and thermoelectric properties due to flexible crystal structure. The ideal perovskite oxides are represented by the general formula ABO_3, where A is typically a rare-earth, alkaline earth or alkali cation and B is a $3d$, $4d$ or $5d$ transition metal. [23] The structure illustrated in Figure 2.8 (a) can be described as a three dimensional array of corner-shared $[BO_6]^{8-}$ octahedra forming a dodecahedral void in which the A cations are situated. Goldshmits tolerance factor can be used to estimate the optimal size of A- and B type cations and deviations from the optimal size can result in a distortion of the octahedra of other distortions lowering the symmetry from cubic. [30] The structure of $CaMnO_3$ is a orthorombic structure with space group Pnma at room temperature and is distorted by tilting of the MnO_6 octahedras as illustrated in Figure 2.8 (b).

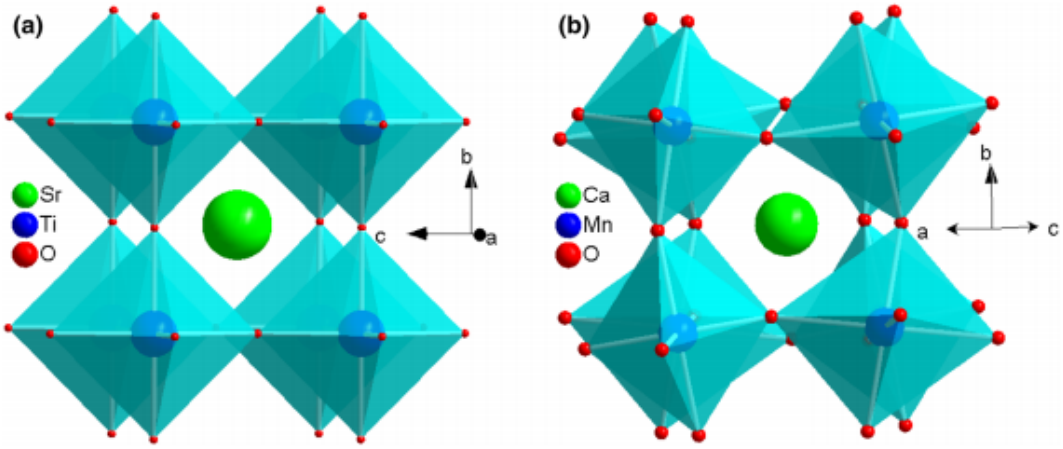

Figure 2.8: (a) Ideal cubic undistorted perovskite structure $SrTiO_3$ (Pm-3m) and (b) orthorombic structure of $CaMnO_3$. [23]

The structure of of $CaMnO_3$ allows for tailoring of the electrical and thermal properties. For example, doping with pentavalent cations such as Ta^{5+}, Ru^{5+} and Nb^{5+} on the Mn^{4+} site has been found to effectively reduce the electrical resistivity. [31][32]

2.5.2 Calcium cobaltite

Recent years, the misfit-layered cobalt oxides have received much attention due to their large thermopower, low thermal conductivity and good chemical stability. [27] In this family $Ca_3Co_4O_9$ considered one of the most promising candidates for energy harvesting. The crystal structure of $Ca_3Co_4O_9$ can be characterized as being comprised of two subsystems, the distorted NaCl-type sublattice, Ca_2CoO_3, and the CdI_2 -type sublattice, CoO_2, stacked along the c-axis. An illustration of the crystal structure can be seen in Figure 2.9. The first layer is a layer comprised of edge-sharing CoO_2 octahedras, where each Co-atom is surrounded by six O-atoms, while the second layer forms a triple rock-salt layer Ca_2CoO_3. [28]

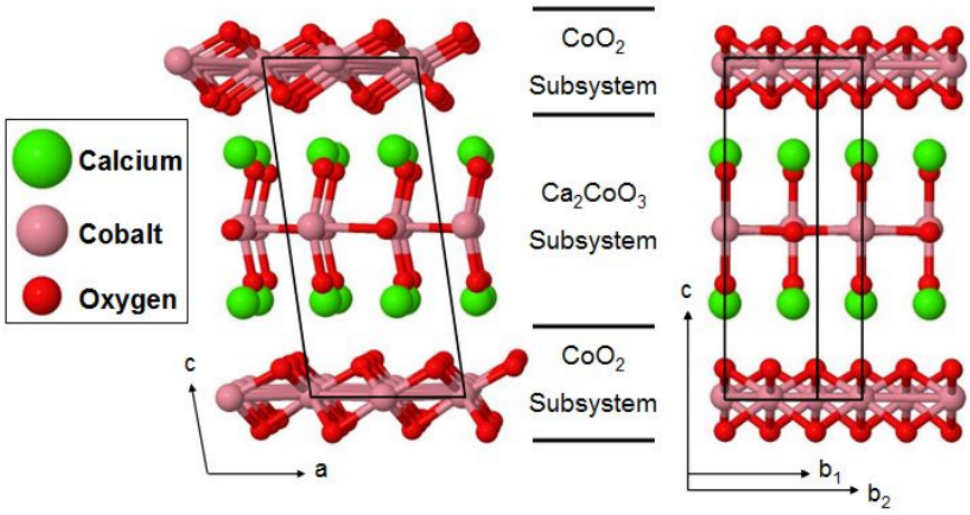

Figure 2.9: Schematic crystallograpic structure of $Ca_3Co_4O_9$ along [010] and [100] zone axes. [33]

The CoO_2-planes provide a route for p-type electronic conduction, while the calcium cobalt oxide misfit layers serve as phonon scattering regions to give low thermal conductivity. Hence, the electron system and phonon system can be independently controlled giving rise to high thermoelectric performance.

2.6 Oxide-based high temperature thermoelectric modules

Research and commercialization of oxide thermoelectric modules are still in their infancy. Although the ZT-values for oxides often are lower than the benchmark value set (ZT = 1) for viable TE materials, oxide TE modules still have been produced and researched. On an international level, Japan has played an important role, with capable devices reported for different pn couples. [34][10] In recent years, work has also been published in Europe. [35][36]

The modules are constructed with bar-shaped p- and n-type thermoelements connected electrically in series and thermally in parallell. Authors have presented various jointing techniques to join the TE legs electrically, most widely applied is the use of metallic pastes. The thermoelements are pressed between two alumina substrates to ensure thermal contact. The power generation characteristics of different oxide modules are summarized in Table 1.1.

Table 2.2: Development of oxide modules.

Author	**Year**	**Materials**	**p-n couples**	**Jointing technique**	$\mathbf{T_H}$ [K]	$\mathbf{T_C}$ [K]	$\mathbf{\Delta T}$ [K]	$\mathbf{V_0}$ [V]	$\mathbf{P_{max}}$ [mW]
Shin et al. [10]	2001	p- Li-doped NiO n- $BaPbO_3$	4	Sintering	1164	625	539	0.39	34.4
Matsubara et al. [34]	2001	p- $(Ca,Ga)_3Co_4O_9$ n- $CaMnO_3$	8	Pt paste	1046	656	390	0.988	63.5
Urata et al. [37]	2006	p- $Ca_{2.7}Bi_{0.3}Co_4O_9$ n- $CaMn_{0.98}Mo_{0.02}O_3$	8	Au paste	897	332	565	1	170
Funahashi et al. [38]	2006	p- $Ca_{2.7}Bi_{0.3}Co_4O_9$ n- $La_{0.9}Bi_{0.1}NiO_3$	140	Ag paste	1027	521	551	4.5	150
Choi et al. [39]	2011	p- $Ca_3Co_4O_9$ n- $(ZnO)_7In_2O_3$	44	Au-paste	1023	823	200	1.8	423
Tomes et al. [36]	2010	p- $GdCo_{0.95}Ni_{0.05}O_3$ n- $CaMn_{0.98}Nb_{0.02}O_3$	4	Au/CuO composite	800	300	500	0.34	40
Feldhoff et al. [35]	2014	p- $Ca_3Co_4O_9$ n- $Zn_{0.98}Al_{0.02}O$	5	Au paste	1023	823	200	0.19	0.55
Bittner et al. [21]	2016	p- $Ca_3Co_4O_9$ n- $In_{1.95}Sn_{0.05}O_3$	5	Au paste	1073	960	113	217	4.8

As seen in Table 2.2, a number of pn couples have been employed in oxide modules, but compared to traditional modules utilizing metallic alloys they still have a long way to go in terms of performance. The voltage and current output is relatively low in comparison.[40] The performance of these devices has not been as good as expected. This is due to several challenges with high contact resistance at the metal/oxide junctions, large differences in thermal expansion between oxide and metal and the compatibility of p- and n-type materials.[26]

2.7 Spark plasma sintering method

Spark plasma sintering (SPS) is an advanced sintering technique which has developed rapidly over the past decades. The method is a solid consolidation sintering process which has enabled effective sintering of metals and ceramics, joining of metals, consolidation of polymers, crystal growth and facilitation of chemical reactions.[41] Figure 2.10 shows materials covered by SPS processing.

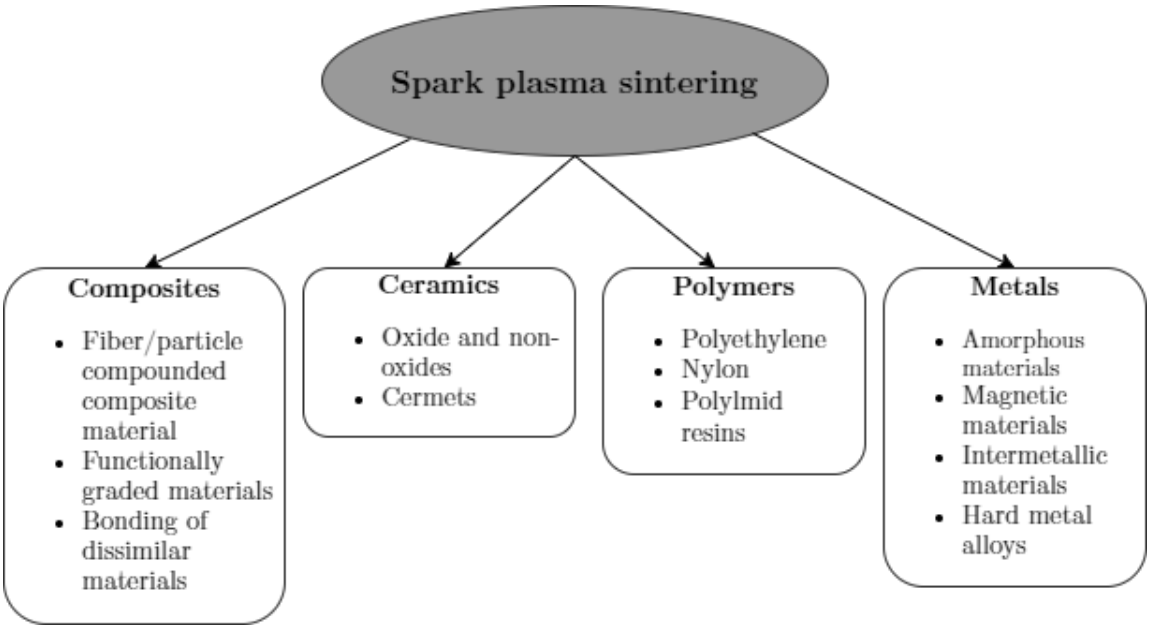

Figure 2.10: Materials for SPS processing. Figure adapted from [42].

In the SPS method powders are consolidated in a carbon die by applying a direct current pulse voltage and pressure. The temperature quickly rises $\sim$ 1000 - 2500 ℃ and results in a highly dense material in a matter of minutes. A schematic of the SPS process is shown in Figure 2.11. It consists of a vertical uni-axial pressurization system. The powder mixture is placed in a graphite die and placed between two punch electrodes, where a minimum pressure is applied in order to ensure good electrical contact. During sintering the current passes through the electrodes and graphite punches which are in contact with both powder and die. For conductive samples the current passes through powder and heats it directly, while for non-conductive samples the current

pathway is through the die and the powder is heated indirectly. The processing is performed inside a vacuum chamber with controllable atmosphere and the temperature is measured by using a pyrometer on a black body cavity on the die wall or by inserting a thermocouple in the die wall.

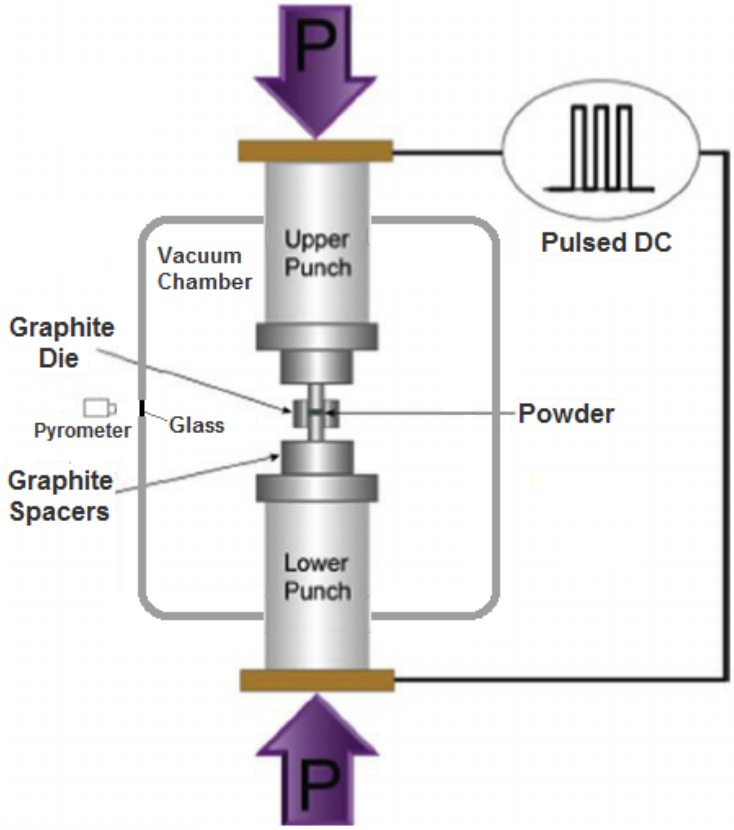

Figure 2.11: Shematic illustration of the spark plasma sintering method. The figure is adapted from [43]. Powder in a conductive die (normally graphite) is heated by a pulsed dc current, simultaneously being subjected to an electric field and uni-axial pressure. The temperature is measured using a thermocouple or optical pyrometry.

The process offers significant advantages compared to conventional sintering methods including hot pressing (HP), hot isostatic pressing (HIP) and sintering in atmospheric furnaces. Among these advantages are lower sintering temperature, shorter holding time and superior material properties. There are a number of mechanisms that are proposed in order to explain the

enhanced sintering abilities of the SPS.

Heat generation in the SPS is internal (joule heating, for conductive samples) as opposed to external like in conventional methods. This facilitation of very high heating and/or cooling rates allows for the sintering process to be very fast. The application of pressure is also aiding particle re-arrangement, which contributes to enhanced sintering. This offers opportunities for densification of nanosized powders while avoiding grain growth promoting diffusion mechanisms which accompanies most standard densification routes (see Figure 2.12). SPS is therefore a suited method for preparation of ceramics based on nanopowders with excellent thermoelectric, optical and piezoelectric properties. [44][45][46]

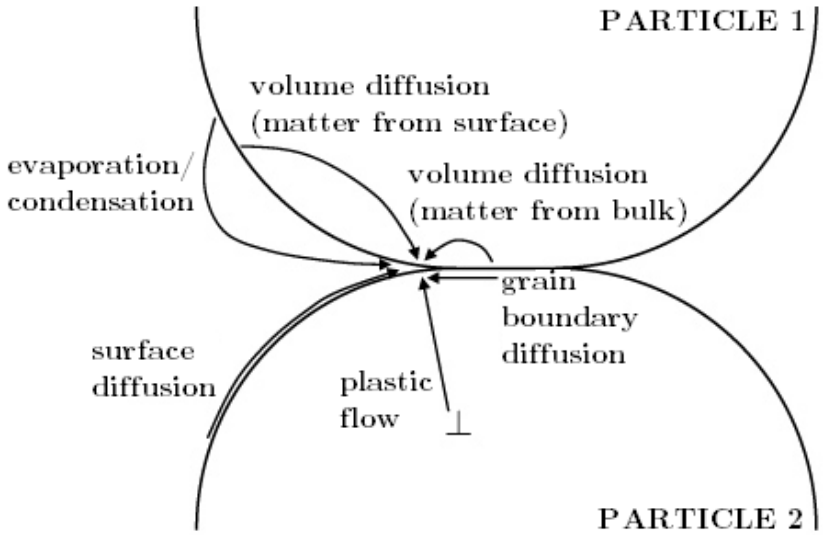

Figure 2.12: Diffusion mechanisms in solid state sintering. The figure is adapted from [47].

Another mechanism proposed is that the on-off dc current in the initial stage of the sintering process generates spark discharge between the particles. [41][48] The generation of spark plasma between the particles during processing is perhaps the most controversial and most widely discussed mechanism. It is believed that high temperature sputtering phenomena generated by spark plasma and spark impact ionises the absorptive gases and eliminates the oxide layers on the surface of the particles activating the sintering process. This role of the current has been advocated by many. [49][50] Work has been presented by Xie et al. [51] where the improved sintering of

alumia with SPS compared to conventional sintering is attributed to the presence of plasma. However, a study of Hulbert et al. [52] using experiments with *in situ* atomic emmission spectroscopy, direct visual observation and *in situ* voltage measurements gave no evidence of plasma during the SPS process. The low voltage and conductive pathway make the presence of an arc or plasma unlikely.

Several authors have presented work on spark plasma sintering of oxides [53][54][55][56][57]. Liu et al. [54] found that the SPS technique could greatly improve the TE properties of $Ca_3Co_4O_9$ ceramics, mainly owing to grain orientation and high bulk density. The reported ZT value of ceramics sintered by SPS was 0.16 at 700 ℃, which was over three times higher than those reported for conventionally sintered samples. Noudem et al. reports improved TE properties of the electron-doped $Ca_{0.95}Sm_{0.05}MnO_3$-oxides compared with a conventional sintering route [55], as well as significantly improved mechanical properties of p-type $Ca_3Co_4O_9$ and n-type $Ca_{0.95}Sm_{0.05}MnO_3$ by SPS [58].

Co-sintering by SPS - Challenges

Co-sintering can be used as an economic fabrication method for multi-layered structures. Therefore, it has been researched in many fields such multilayer co-sintered ceramics (HTCC or LTCC) for electronic sensors [59], solid oxide fuel cells (SOFC) [60] and ceramic membranes [61]. Thermal mismatch between layers/materials will be a common key problem during the co-sintering process.

Spark plasma sintering (SPS) is a promising technology for co-sintering, mainly due to the benefits of pressure assisted sintering, fast heating, short sintering time and slightly lower sintering temperature in comparison to alternative techniques. There exists very little research on the co-sintering process in SPS, but some work has been presented [62][63]. Construction of an all oxide device in the manner illustrated in Figure 1.2 will involve the co-sintering of three different materials. Each layer is made from ceramic powder and/or tape which has different compositions, particle size and not to mention sintering behaviour. In order to produce a device with good bonding between the material and sufficient mechanical stability, the thermal expansion coefficients (TEC) of CCO, CMTO and LAO need to be considered. The larger the thermal mismatch between the materials, the more build-up of stresses in the device. The thickness of each layer in the device

is another important factor during the co-sintering process and will investigated in the following section.

2.8 Residual stresses in multilayer systems

Faalands [64] has published a simplified model for calculation of the residual stresses in a multilayer system, see Figure 2.13. The model is based on the force balance method and several authors have presented calculations based on this method previously [65][66][67]. The method is normally applied for symmetric composites, but can be generalized to asymmetric composites as well. It is assumed that the support material is thick, so that bending of the structure is impossible, hence the strain is constant in the whole composite. Each layer is considered isotropic and linearly elastic. The stress normal to the layers is zero, σ_z = 0, while the stresses in the x- and y-direction are equal, $\sigma_x = \sigma_y$.

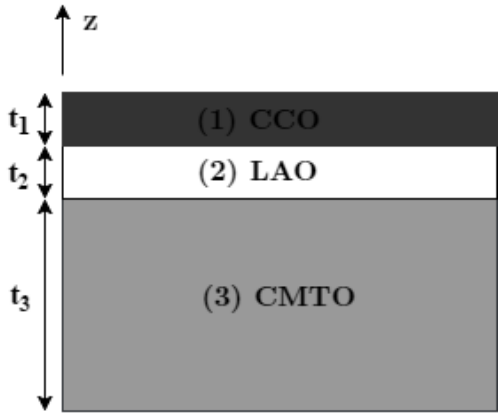

Figure 2.13: Schematic of a multilayered structure based on a material system composed of CCO, CMTO and LAO. Figure based on information from Faaland [64].

Hooke's law combined with the assumptions above gives the following equation for the elastic stresses in the layers:

$$\sigma_i = \frac{E_i}{1 - \upsilon_i}(\epsilon_i - \alpha_i \Delta T) \tag{2.9}$$

where i is the layer index, E_i in the Youngs modulus, υ_i is the Poisson's ratio, ϵ_i is the overall biaxial strain, α_i is the thermal expansion coefficient and T is the absolute temperature.

The strains in each layer have two contributions, one from the expansion of a volume element not allowed to expand freely, as it is constrained as a part of an elastic body and one due to thermal expansion. Thus, the strain in each layer is given by:

$$\epsilon_i = \frac{1-\upsilon_i}{E_i}\sigma_i + \alpha_i \Delta T \tag{2.10}$$

Since the strain is constant in the entire composite, the following relation applies:

$$\epsilon_1 = \epsilon_2 = \epsilon_3 \tag{2.11}$$

Resulting in two independent equations:

$$\frac{1-\upsilon_1}{E_1}\sigma_1 + \alpha_1 \Delta T = \frac{1-\upsilon_2}{E_2}\sigma_2 + \alpha_2 \Delta T \tag{2.12}$$

$$\frac{1-\upsilon_2}{E_2}\sigma_2 + \alpha_2 \Delta T = \frac{1-\upsilon_3}{E_3}\sigma_3 + \alpha_3 \Delta T \tag{2.13}$$

Also, the force balance requires that:

$$\sum_{i=1}^{3} \sigma_i t_i = 0 \tag{2.14}$$

as the stress is independent of z-direction in the material i. Here, σ_i is the stress and t_i is the thickness of the material. By combining equation (2.12), (2.13) and (2.14), the expressions for the three unknowns σ_1, σ_2 and σ_3 can be found:

$$\sigma_1 = -\frac{\Delta T((\alpha_1-\alpha_2)\frac{E_2 t_2}{(1-\upsilon_2)} + (\alpha_1-\alpha_3)\frac{E_3 t_3}{(1-\upsilon_3)})}{t_1 + \frac{(1-\upsilon_1)}{(1-\upsilon_2)}\frac{E_2 t_2}{E_1} + \frac{(1-\upsilon_1)}{(1-\upsilon_3)}\frac{E_3 t_3}{E_1}} \tag{2.15}$$

$$\sigma_2 = -\frac{\Delta T((\alpha_2-\alpha_1)\frac{E_1 t_1}{(1-\upsilon_1)} + (\alpha_2-\alpha_3)\frac{E_3 t_3}{(1-\upsilon_3)})}{t_2 + \frac{(1-\upsilon_2)}{(1-\upsilon_1)}\frac{E_1 t_1}{E_2} + \frac{(1-\upsilon_2)}{(1-\upsilon_3)}\frac{E_3 t_3}{E_2}} \tag{2.16}$$

$$\sigma_1 = -\frac{\Delta T((\alpha_3-\alpha_2)\frac{E_2 t_2}{(1-\upsilon_2)} + (\alpha_3-\alpha_1)\frac{E_1 t_1}{(1-\upsilon_1)})}{t_3 + \frac{(1-\upsilon_3)}{(1-\upsilon_1)}\frac{E_1 t_1}{E_3} + \frac{(1-\upsilon_3)}{(1-\upsilon_2)}\frac{E_2 t_2}{E_3}} \tag{2.17}$$

To be able to apply this method to the CMTO-CCO-LAO system some approximations and assumptions must be made. The poisson ratio for all three materials is assumed to be 0.3 and the ferroelastic properties of LAO are not considered. The values for the Young's modulus of the materials are presented in Table 2.3.

Table 2.3: Young's modulus for CMTO, CCO and LAO.

Material	**Young's modulus [GPa]**	**Reference**
CMTO	205	[55]
CCO	66	[58]
LAO	287	[68]

The equations for the stress in a material i (i=1 CCO, i=2 LAO and i=3 CMTO) are therefore simplified to:

$$\sigma_1 = -\frac{\Delta T((\alpha_1 - \alpha_2)\frac{E_2 t_2}{0.7} + (\alpha_1 - \alpha_3)\frac{E_3 t_3}{0.7})}{t_1 + \frac{E_2 t_2}{E_1} + \frac{E_3 t_3}{E_1}} \tag{2.18}$$

$$\sigma_2 = -\frac{\Delta T((\alpha_2 - \alpha_1)\frac{E_1 t_1}{0.7} + (\alpha_2 - \alpha_3)\frac{E_3 t_3}{0.7})}{t_2 + \frac{E_1 t_1}{E_2} + \frac{E_3 t_3}{E_2}} \tag{2.19}$$

$$\sigma_3 = -\frac{\Delta T((\alpha_3 - \alpha_2)\frac{E_2 t_2}{0.7} + (\alpha_3 - \alpha_1)\frac{E_1 t_1}{0.7})}{t_3 + \frac{E_1 t_1}{E_3} + \frac{E_2 t_2}{E_3}} \tag{2.20}$$

Chapter 3

Experimental

3.1 Preparation of samples for spark plasma sintering (SPS)

3.1.1 Formation of single material samples

Nanosized powders of $Ca_3Co_4O_9$ (CCO), $Ca_{0.931}Mn_{0.98}Ta_{0.02}O_{3-\delta}$ (CMTO) and $LaAlO_3$ (LAO) were delivered by Ceramic Powder Technology AS (CerPoTech AS). Samples of CCO, CMTO and LAO were prepared by spark plasma sintering (SPS) under vacuum using a Dr Sinter SPS machine (MODEL 825). The inside of the carbon die (12 mm inner diameter) was covered in graphite sheets, a rectangle (4 cm x 3.8 cm) and 4 circles (Ø = 12 mm) were cut for each sample. The inside of the die wall was covered by inserting the graphite sheet rectangle and cutting the side (3.8 cm) for a perfect fit. The bottom piston was inserted carefully and two graphite circles were placed inside the die to cover it. CCO (1 g), CMTO (1 g) and LAO (1.5 g) respectively were homogeneously distributed inside the die, before inserting the last two graphite circles and top piston. The outside of the carbon die was wrapped in carbon felt which was tied in place using carbon tread for thermal insulation. SPS was manually performed applying a heating rate of approximately 88 ℃/min up to the sintering temperature of 880 ℃, while the pressure was increased to 75 MPa. The samples were subsequently cooled at a rate $>$50 ℃/min (power off, ”natural cooling”). Residence time for all samples was 2 min. Resulting geometry after SPS was typically discs (Ø = 12 mm and h = 2 mm).

After sintering, the density, open and closed porosity was assessed using the Archimedes'

method [69], in which the dry mass, mass in isopropanol and wet mass of the sample was measured.

The CCO pellet was polished and subjected to thermal etching at 830 ℃ to accentuate the grain boundaries before SEM investigations. The etching program can be seen in Figure 3.1

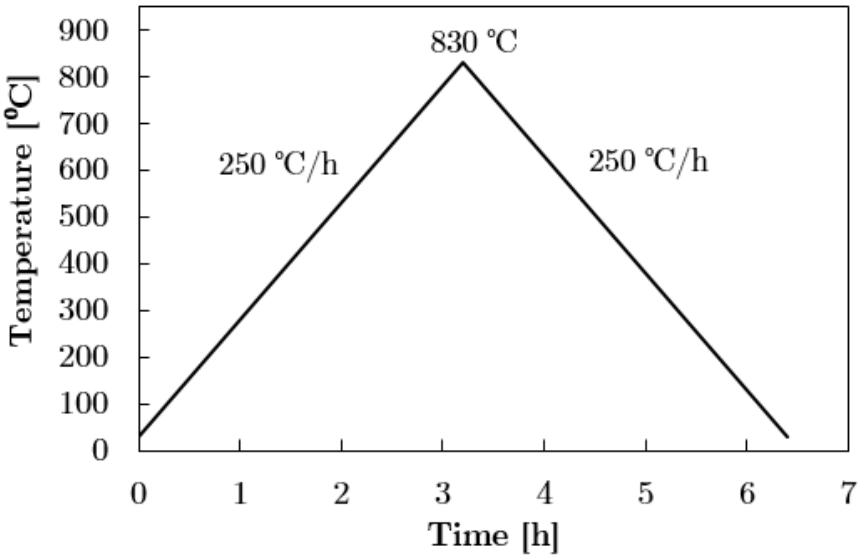

Figure 3.1: Thermal etching program used on CCO.

3.1.2 Formation of diffusion couples

Diffusion couples were prepared combining equal ratios of CCO and CMTO powders, CCO and LAO powders and CMTO and LAO powders (0.5 g). The die wall and pistons were covered with graphite sheets in the same manner as explained for the single material samples. Each powder was distributed homogeneously in the carbon die by rotating the die while subsequently using a weighing ship create a continuous flow of powder into the die. The bottom of the die was knocked gently against a flat surface before addition of a new powder to promote uniform and dense packing. The samples were prepared using manual control of the SPS with a heating rate of approximately 88 ℃/min up to a temperature of 850 ℃, while the pressure was increased to 75 MPa. The samples were subsequently cooled at a rate >50 ℃/min (power off, ”natural cooling”). Residence time at T_{SPS} for all samples was 2 min. An overview of the process parameters used

during SPS for all samples can be seen in Table 3.1.

Table 3.1: Process parameters used in SPS of single material samples and diffusion couples.

Sample	T_{SPS} (℃)	Residence time T_{SPS} (min)	Applied pressure (MPa)	Post sintering analysis		
				Density	XRD	SEM
LAO	880	2	75	x	x	x
CCO	880	2	75	x	x	x
CMTO	880	2	75	x	x	x
CMTO/CCO	850	2	75			x
CMTO/LAO	850	2	75			x
CCO/LAO	850	2	75			x

3.1.3 Device preparation

Formation of ceramic tapes

Green tapes of LAO were prepared by tape casting. The slurry for preparation of LAO tape was prepared using the method presented in Figure 3.2 and is described in detail in the following section. Surfactant Darvan C-N (0.25 g) and water (40.75 g) was weighed out in a glass beaker and ultrasonicated for 3 min. LAO powder (30 g) and zirconia balls (300 g) were added to a polyethylene bottle and water-surfactant mixture (approximately 25 g) was added using a pipette until no more dry powder was visible. The mixture was milled for 6 h using a ball mill. Polyethylene glycol (PEG) (1.50 g) was mortared and added to the polyethylene bottle along with polyvinyl alcohol 15 wt% (PVA) (43 g) and polypropylene glycol (0.40 g). The mixture was further milled for 24 h.

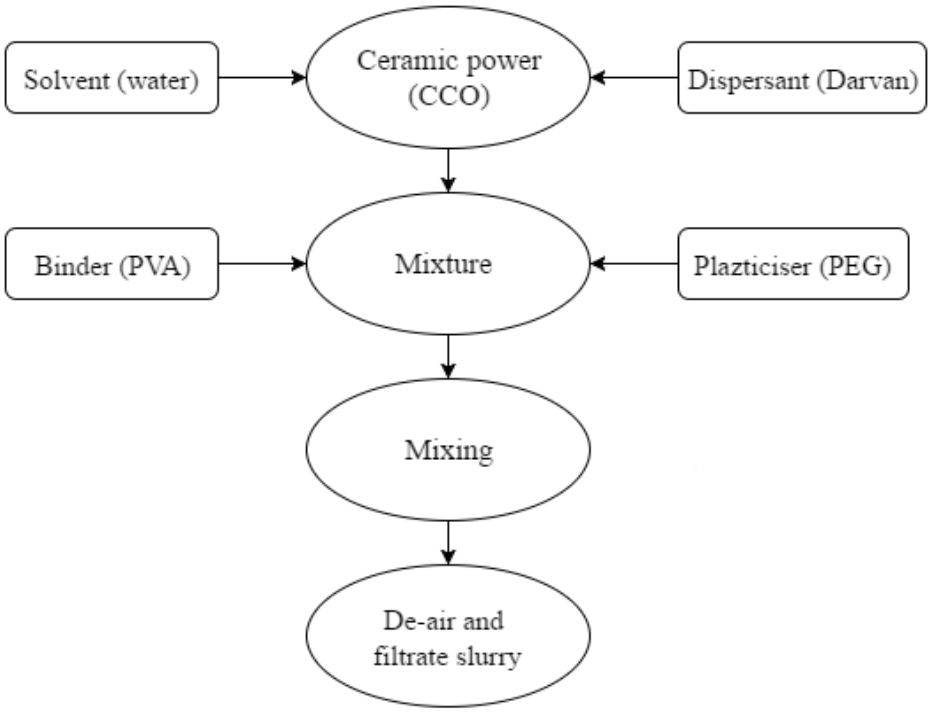

Figure 3.2: Schematic flow chart of slurry preparation

The ceramic slurry was continuously spread over a conveyor belt with the help of a doctor blade to form a flat, even layer (0.3 mm). The casted slurry was dried in a drying chamber for three days and the resulting tape was cut for further processing. The tape casting process utilized is illustrated in Figure 3.3.

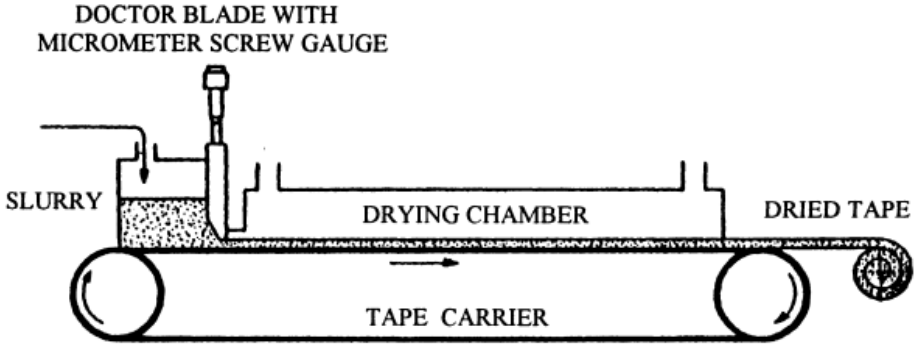

Figure 3.3: Schematic illustration of tape casting. Figure adapted from [70].

The tapes were laminated by layering eight pieces of tape on top of each other and spraying a thin layer of water in between each layer using an air brush. The tapes were pressed together using a hot press with a pressure of 0.5 MPa at 80 ℃. Semi-circles of laminated green tape (Ø = 12 mm) were prepared using a hole punch and scissors. The laminated tapes were heated in a Naberterm furnace to burn off the binder. The heating program for burning off binder can be seen in Figure 3.4.

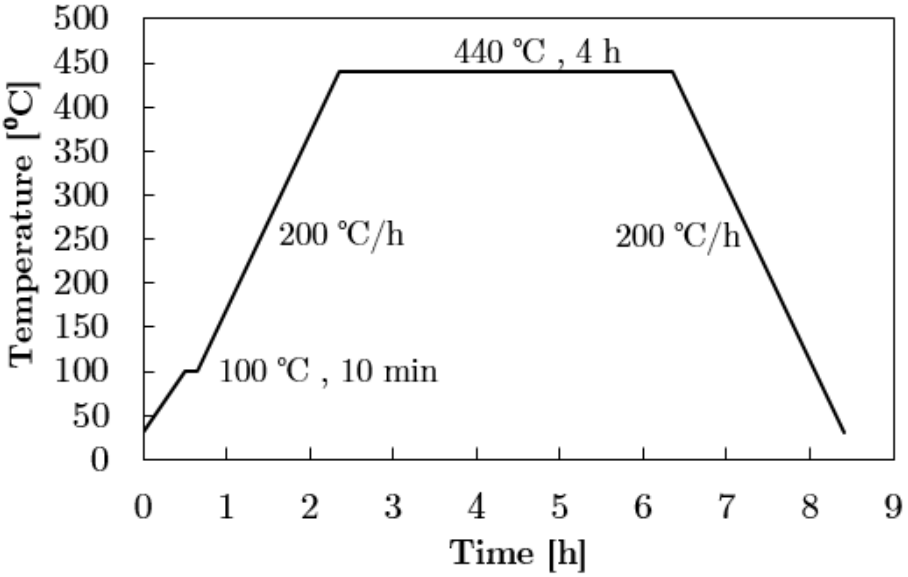

Figure 3.4: The heating program used to burn off binder in LAO tape.

Fabrication of TE devises by SPS

Single thermoelectric couples were prepared by stacking CCO powder, LAO tape and CMTO powder in a carbon die (Ø = 12 mm). The die wall and pistons were covered with graphite sheets in the same manner as explained for the single material samples. The CMTO powder was distributed homogeneously in the die by rotating the die while subsequently using a weighing ship create a continuous flow of powder into the die. The bottom of the die was knocked gently against a flat surface to create a completely flat powder surface of CMTO. A semi-circle of LAO tape was carefully placed on top of the CMTO powder using a pair of tweezers. Finally, CCO powder was added using the same method described for the CMTO powder creating a pn junction where the

CMTO and CCO powders were in contact. The bottom of the die was knocked against a flat surface a few times before inserting two graphite circles and the upper piston. A schematic illustration of the entire sample preparation can be seen in Figure 3.5. The parameters that were varied during processing are listed in Table 3.2. The samples were prepared using an automatic program in the SPS. The residence time at T_{SPS} was varied to investigate its effect on microstructure and interdiffusion between the materials. Figure 3.6 shows the pressure and temperature program for samples with residence time at 880 ℃ of 2 min and 5 min.

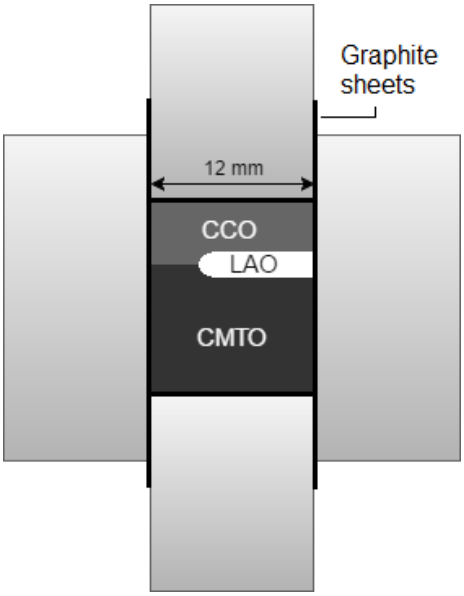

Figure 3.5: Schematic illustration of preparation of a single themoelectric couple in the carbon die using CMTO and CCO powders and LAO tape.

Table 3.2: Parameters varied during the processing of single thermoelectric couples in SPS

T_{SPS} (℃)	Pressure (MPa)	Residence time at T_{SPS} (min)	Amount CCO (g)	Amount CMTO (g)	Laminated LAO tape (#)
880	75	4	1	1	1
880	75	6	1	1	1
880	75	2	0.2	1.5	1
880	75	2	0.4	1.5	1
880	75	5	0.2	1.5	1
880	75	5	0.4	1.5	1
880	50	4	1	1	1
850	75	6	1	1	1
850	50	6	1	1	1
920	75	2	1	1	1
870	50	10	1	1	1
800	50	10	1	1	1

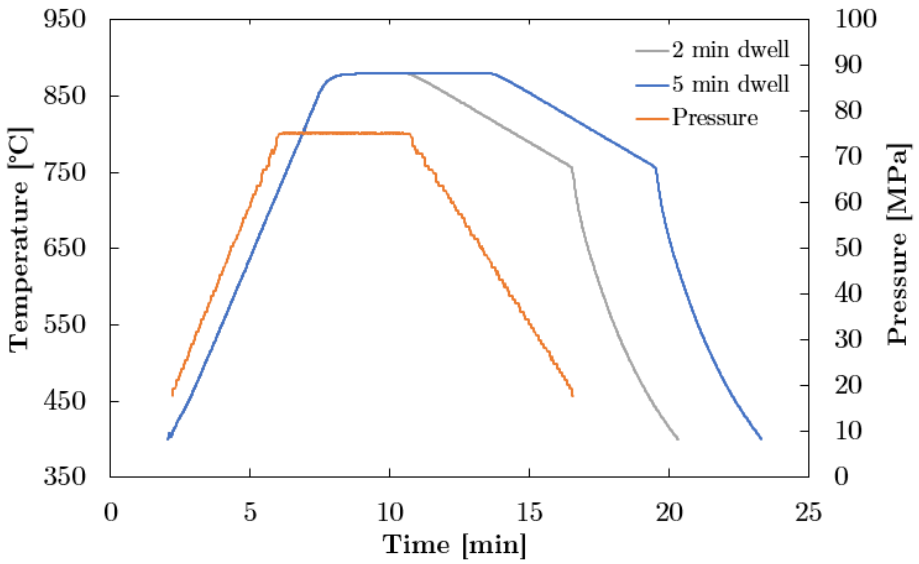

Figure 3.6: The SPS programme used to sinter single thermoelectric couples at 880 ℃ and 75 MPa with varying residence time of 2 min and 5 min. Heating rate is ∼ 85 ℃/h and cooling rate is ∼ 20 ℃/h down to 750 ℃ before natural cooling.

Characterization of the device

The obtained disc-shaped ceramic samples were cut by a diamond saw to produce the rectangular shape needed for measurements. Platinum wires were attached to the n- and p- type materials with gold paste in order to construct an external electrical circuit. Characterization the TE device was realized through a load-resistance dependent measurement under steady state conditions.

The oxide-based thermoelectric couple was characterized at high-temperature conditions in air. The hot side of the device was heated by a furnace up to 700 and 800 ℃, while the other side was cooled by an active cooler to establish a temperature gradient over the device obtaining a temperature drop of ΔT = 130 ℃. The temperature of the hot and cold side was measured by two Pt-Rh thermocouples. The generator was connected with a voltmeter and an amperemeter in parallel connection. After 1 hour the device was in equilibrium, and the variable resistor in the external circuit was switched and thereby different load resistances R_{load} were applied. The electrical current J and voltage U were measured varying R_{load} and Thot, with measuring steps lasting 3 min.

3.2 Characterization techniques

X-ray diffraction (XRD) was used to investigate the phase composition and purity of the materials. Diffractograms were obtained in the 2θ range of 10 - 75° in a Bruker D8 Advance DaVinci instrument using a Cu source and a step size of 0.02°. The obtained patterns were analysed in EVA software and compared against patterns found in the International Centre for Diffraction Data (ICDD) in order to obtain phase composition.

Particle size, particle morphology, fracture surface and microstructure were investigated on a field emission scanning electron microscope (SEM) Hitachi SU-6600. Product phases and their location in the samples was investigated using backscattered electrons (BSE) on a field emission SEM Hitachi SU-6600 and/or a Hiatchi S-3400N in-lens cold field emission scanning electron microscope. Energy-dispersive X-ray spectroscopy (EDS) was used to investigate phase composition and cationic interdiffusion between the different material interfaces. The parameters used for imaging of the different samples are given in Table 3.3.

Samples used for microstructure characterization and compositional analysis were cast in

epoxy and fine-polished. All samples were grinded starting with #1200 grit SiC paper and stepwise reducing grit size down to #4000 grit SiC paper. Further, the samples were polished in a Struers machine with diamond suspensions of 3 µm and 1 µm particles successively. TE couples with a residence time of 2 and 5 min were in addition etched in HNO_3 (68%) for 10 min after polishing to accentuate the grains in the CCO phase.

The coefficient of thermal expansion (TEC) of CMTO, LAO and CMTO was estimated in synthetic air using a dilatometer DIL 402 C from Netzsch.

Table 3.3: Parameters used in SEM imaging

Setting	**Signal carrier**	**Acc.voltage**	**Probe current**	**Sample base**	**Sample coating**
CTMO powder	SE	25 kV	40 nA	Carbon tape	Gold
CCO powder	SE	15 kV	40 nA	Carbon tape	Carbon
LAO powder	SE	15 kV	40 nA	Carbon tape	Carbon
CMTO pellet	SE	15 kV	60 µA	Carbon tape	Carbon
CCO pellet	SE	15 kV	60 µA	Carbon tape	Carbon
LAO pellet	SE	15 kV	60 µA	Carbon tape	Carbon
Diffusion couples	BSE	15 kV	60 µA	Aluminum foil	Carbon
TE-device	SE/BSE	15 kV	78 µA	Aluminum foil	Carbon

Chapter 4

Results

4.1 Single material characterization

Particle size and morphology of powders

Figure 4.1 shows a SEM micrograph of the CMTO powder used in this work. The CMTO powder consists mainly of small spherical particles well below 1 µm.

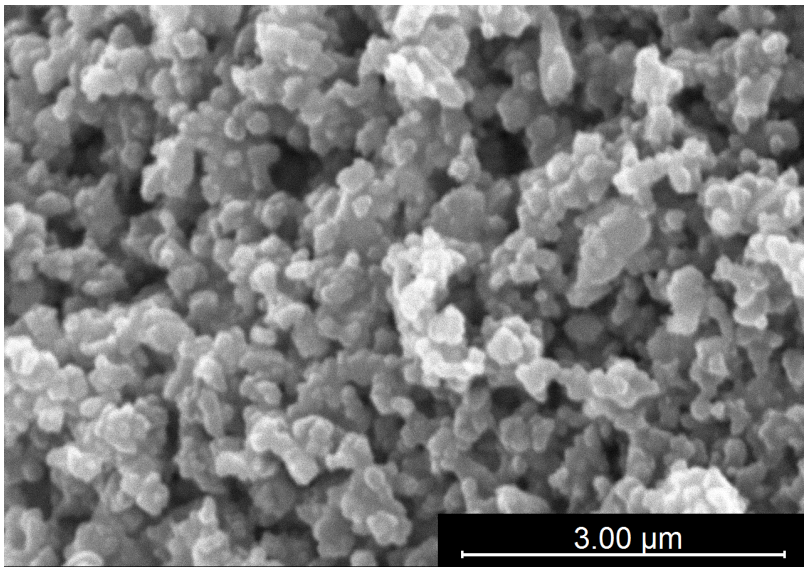

Figure 4.1: SEM micrograph of CMTO powder.

Figures 4.2a and 4.2b show micrographs of the LAO powder and CCO powder respectively showing that both powders consist of rounded particles below 1 µm.

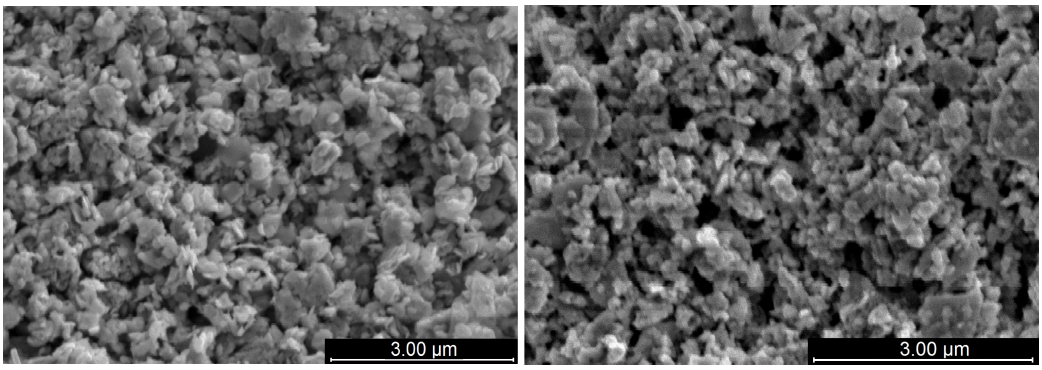

(a) (b)

Figure 4.2: SEM micrographs of the powders: (a) LAO and (b) CCO.

Phase composition

In the figures presented below the X-ray diffractograms of the as-received powders and pellets sintered by SPS at 880 ℃ with a pressure of 75 MPa and a holding time of 2 min are compared. The diffractogram of the CMTO powder (turquoise) in Figure 4.3 shows a secondary phase $CaMn_2O_4$ (PDF card 00-515-1998) in addition to the $CaMnO_3$ perovskite phase (PDF card 04-014-8192). The diffractogram of the CMTO pellet (purple) shows the same phase composition.

Figure 4.4 shows the diffractograms obtained of CCO. The diffractogram of the CCO pellet (light green) shows the presence of small amounts Co_3O_4 as a secondary phase (PDF card 04-001-8014) in addition to the main phase, $Ca_3Co_4O_9$ (PDF card 00-051-0311), which is not present in the diffractogram of the CCO powder (orange). This is most likely due to the fact that the sintering temperature of 880 ℃ is close the decomposition temperature of CCO. The local sintering temperature between the particles can be higher than 880 ℃ and cause partial decomposition of CCO.

The diffractogram of LAO powder (blue) and pellet (red) in Figure 4.5 show the same phase composition (PDF card 01-085-0848).

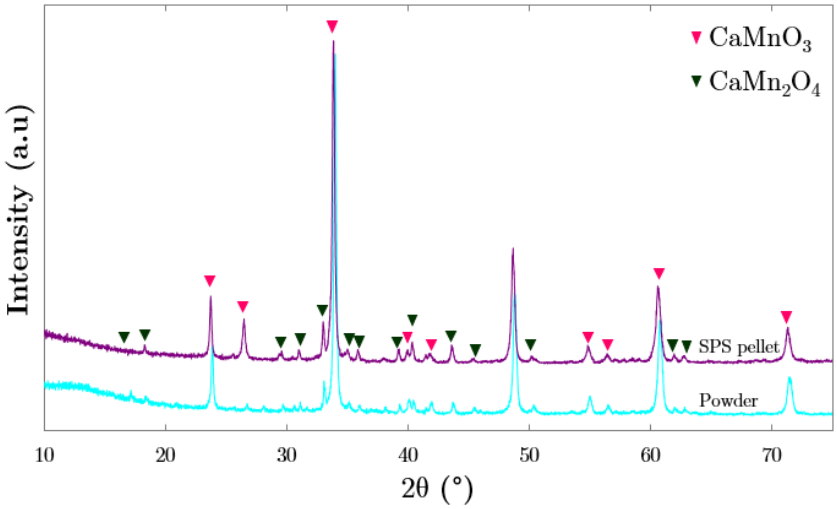

Figure 4.3: X-ray diffractogram of CMTO powder and pellet sintered by SPS at 880 ℃ with a pressure of 75 MPa and holding time of 2 min. References marked with triangles are $CaMnO_3$ (pink, PDF card 04-014-8192) and $CaMn_2O_4$ (green, PDF card 04-015-3975).

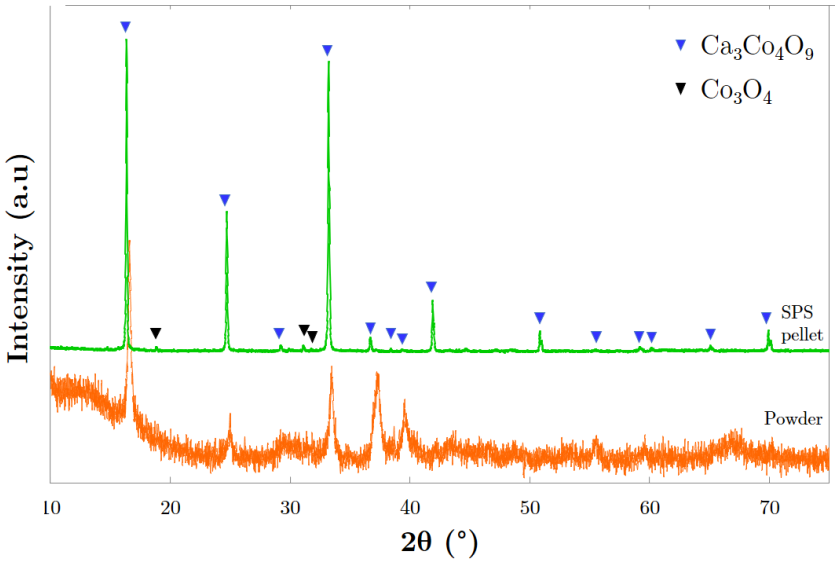

Figure 4.4: X-ray diffractogram of CCO powder and pellet sintered by SPS at 880 ℃ with a pressure of 75 MPa and holding time of 2 min. References marked with triangles are $Ca_3Co_4O_9$ (sky blue, PDF card 00-051-0311) and Co_3O_4 (black, PDF card 04-001-8014).

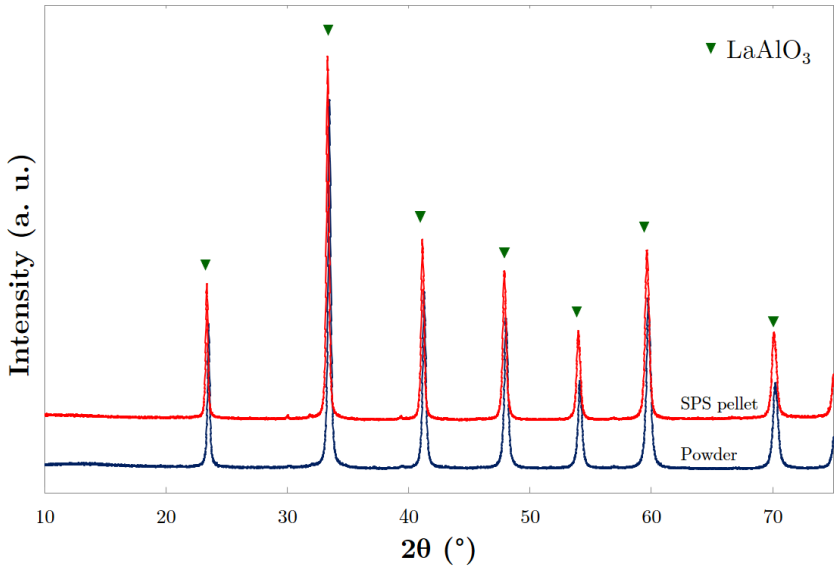

Figure 4.5: X-ray diffractogram of LAO powder and pellet sintered by SPS at 880 ℃ with a pressure of 75 MPa and holding time of 2 min. Reference marked with triangles is $LaAlO_3$ (green, PDF card 01-085-0848).

Density

For the p-type material CCO, 96 % of the theoretical density was achieved. The n-type CMTO and insulator LAO achieved densities of 69 % and 41 % respectively. Table 4.1 shows the measured values for the density of the bulk ceramics as well as calculated values for open porosity and closed porosity.

Table 4.1: Density using Archimedes method of pellets sintered by SPS at 880 ℃ and 75 MPa for 2 min.

Material	Density [%]	Open porosity [%]	Closed porosity [%]
CMTO	68.3	28.6	3.1
CCO	95.8	0.7	3.5
LAO	40.8	56.8	2.4

Fracture surface

SEM micrographs of the fracture surface of pellets sintered in SPS at 880 ℃, 75 MPa and 2 min residence time are presented in the following section.

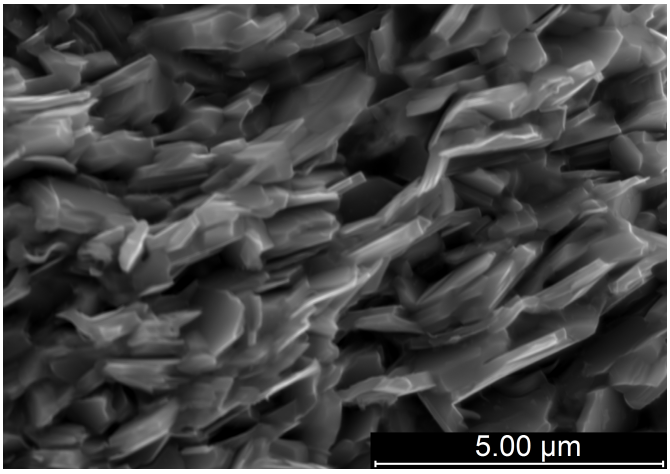

(a)

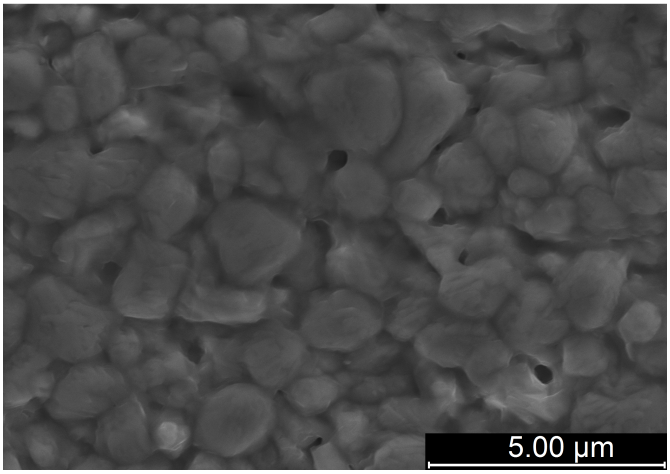

(b)

Figure 4.6: SEM micrographs of CCO sample sintered in SPS at 880 ℃ with a pressure of 75 MPa and residence time of 2 min: a) fracture surface and b) thermally etched surface. (pressing direction is unknown)

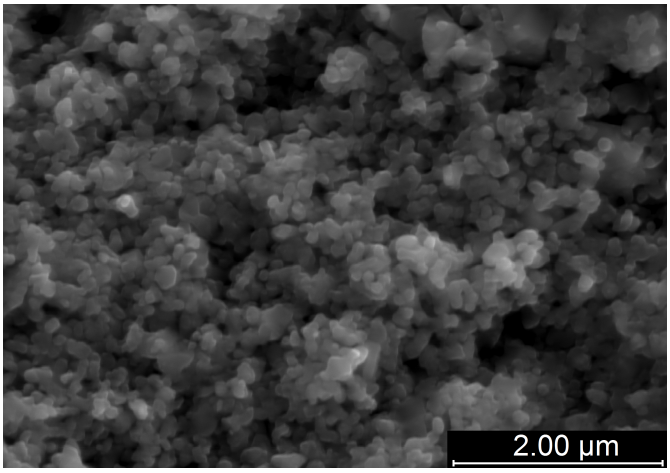

Figure 4.7: SEM micrograph of the fracture surface of CMTO sintered in SPS at 880 ℃ with a pressure of 75 MPa and residence time of 2 min.

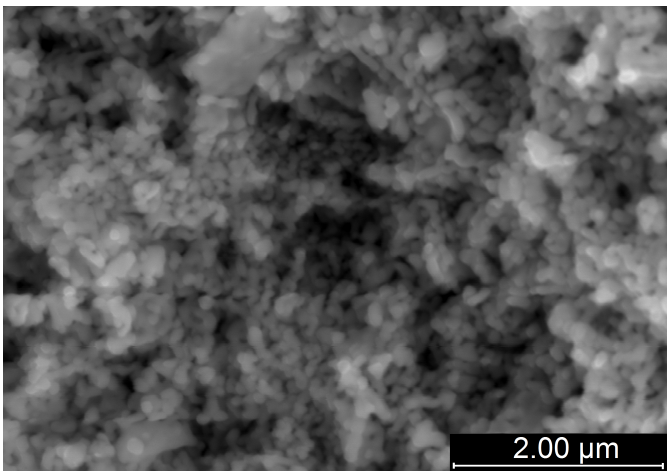

Figure 4.8: SEM micrograph of the fracture surface of LAO sintered in SPS at 880 ℃ with a pressure of 75 MPa and residence time of 2 min.

In Figure 4.6a the fracture surface of CCO can be seen. From the micrograph it is observed that CCO has sheet-like grains, this is expected due to the layered stucture of the oxide. A pronounced grain alignment is also visible. A SEM micrograph of a polished cross section of the CCO sample after thermal etching at 830 ℃ is shown in Figure 4.6b. Based on these results the grain size of

the CCO sample can be estimated to be 1.19 ± 0.41 µm.

The fracture surfaces of CMTO and LAO can be seen in Figure 4.7 and 4.8 respectively. The samples exhibit highly porous microstructures with small grains. A rough estimate of the grain size based on the SEM micrographs of the fracture surfaces is 0.14 ± 0.05 µm for CMTO and 0.13 ± 0.05 µm for LAO.

Thermal expansion coefficient

The thermal expansion coefficient (TEC) of CMTO, CCO and LAO was calculated by plotting values obtained using a dilatometer in the following relation:

$$\frac{\Delta L}{L_0} = \alpha_L \cdot \Delta T \tag{4.1}$$

Figure 4.9, 4.10 and 4.11 show the the variation in length over initial length as a function of temperature for the different materials. The thermal expansion coefficient was calculated from the measured values (dashed lines) for both heating and cooling. The estimated TEC values can be seen in Table 4.2.

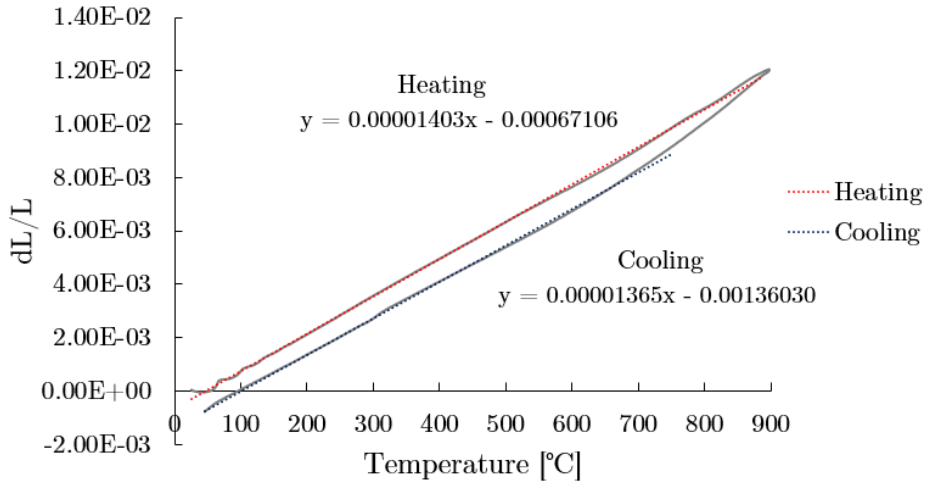

Figure 4.9: Thermal expansion coefficient (TEC): thermal expansion and shrinkage of CCO during heating (red) in the temperature range of 25 - 900 ℃ and cooling (blue) in the temperature range of 25 - 750 ℃.

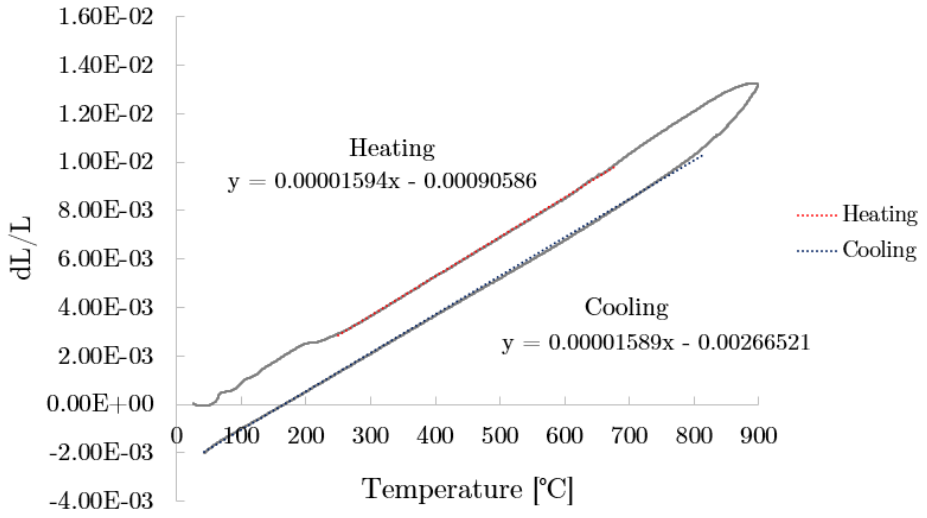

Figure 4.10: Thermal expansion coefficient (TEC): thermal expansion and shrinkage of CMTO during heating (red) in the temperature range of 250 - 650 ℃ and cooling (blue) in the temperature range of 25 - 800 ℃.

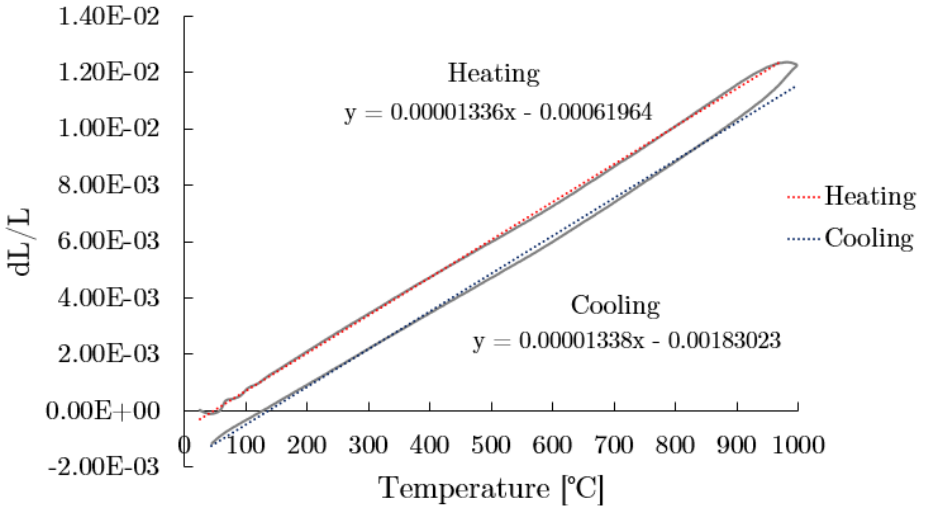

Figure 4.11: Thermal expansion coefficient (TEC): thermal expansion and shrinkage of LAO during heating (red) and cooling (blue) in the temperature range of 25 - 1000 ℃.

Table 4.2: Calculated TEC values for heating and cooling for CMTO, CCO and LAO.

Material	**TEC heating [K^{-1}]**	**TEC cooling [K^{-1}]**
CMTO	$15.9 \cdot 10^{-6}$	$15.9 \cdot 10^{-6}$
CCO	$14.0 \cdot 10^{-6}$	$13.7 \cdot 10^{-6}$
LAO	$13.4 \cdot 10^{-6}$	$13.4 \cdot 10^{-6}$

4.2 Diffusion couples

Results for diffusion couples made of two and two materials sintered in SPS at 850 ℃ with 2 min residence time and 75 MPa pressure are presented in the following section. In Figure 4.12a a micrograph of the CMTO and CCO junction can be seen, while Figure 4.12b shows EDS mapping of the junction. From the overview in Figure 4.12a good contact and no delamination between the materials is observed. However, a reaction layer is visible in the EDS maps in Figure 4.12b. The figure shows a region at the interface between CMTO and CCO which has a higher calcium content and lower manganese content compared to the CMTO phase. The thickness of the reaction layer is approximately 2.1 µm.

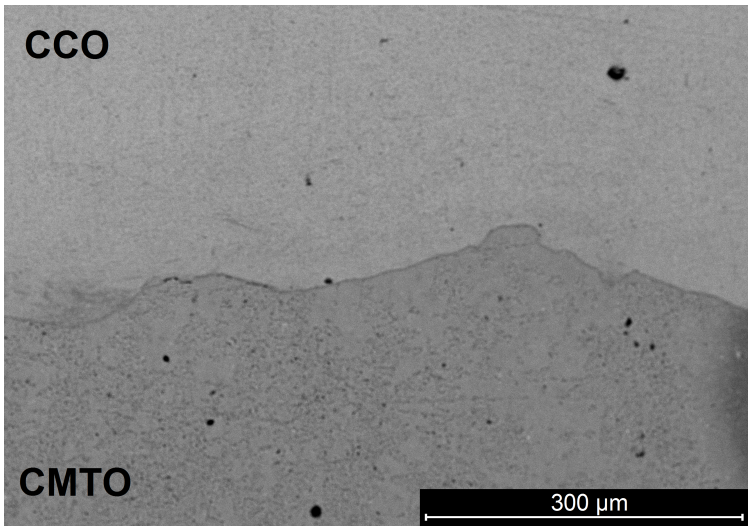

(a)

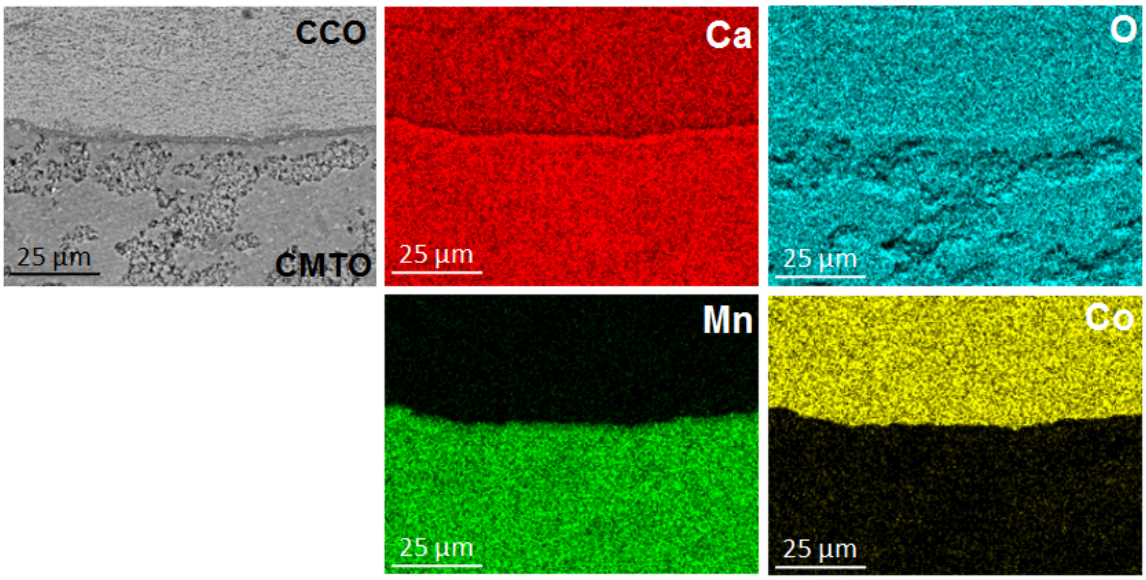

(b)

Figure 4.12: SEM images and EDS mapping of polished cross-section of diffusion couple composed of CCO and CMTO sintered by SPS at 850 ℃ and 75 MPa pressure for 2 min: a) BSE image with overview of interface and b) EDS mapping of CCO-LAO juction obtained from area depicted on the BSE image. K_α detected for calcium (Ca), cobalt (Co), manganese (Mn) and oxygen (O).

In Figure 4.13a a SEM micrograph of the polished cross-section of interface between CMTO and LAO can be seen. A large horizontal crack is visible across the junction with a width of $\sim$ 127 µm. There are also some small cracks observed in a vertical direction in the sample. EDS analysis of the CMTO-LAO junction, in Figure 4.13b, shows no indication of a reaction layer at the interface between the materials. The EDS maps show a sharp and clear interface without any changes in color gradient.

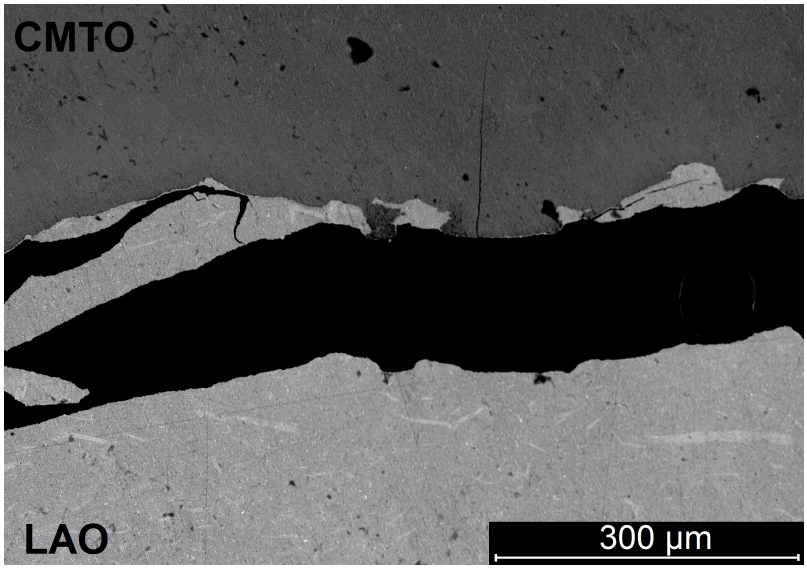

(a)

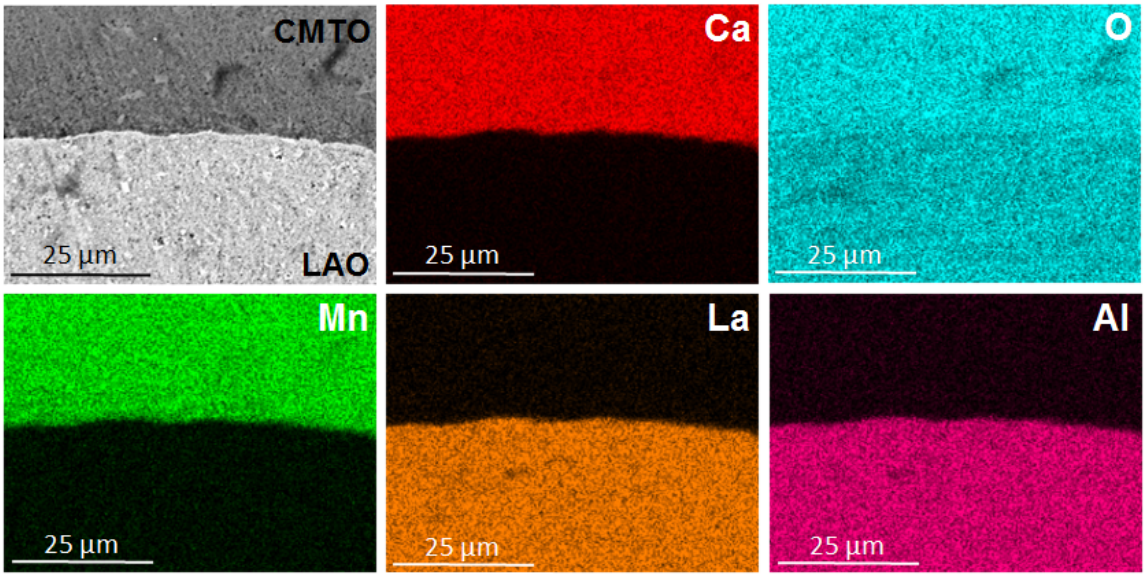

(b)

Figure 4.13: SEM images and EDS mapping of polished cross-section of diffusion couple composed of CMTO and LAO sintered by SPS at 850 ℃ and 75 MPa pressure for 2 min: a) BSE image with overview of interface and b) EDS mapping of CCO-LAO junction obtained from area depicted on the BSE image. L_α detected for lanthanum (La) and K_α for calcium (Ca), manganese (Mn), aluminium (Al) and oxygen (O).

Figure 4.14a shows a BSE image of a polished cross-section of the interface between CCO and LAO. From the micrograph a layer with a different phase composition than CCO and LAO is observed along the interface. The thickness of the layer varies in the range $\sim$ 16 - 55 µm. EDS mapping of the interface can be seen in Figure 4.14b. The results show that the layer is rich in cobolt and deficient in calcium compared to the CMTO phase. This is also confirmed by using EDS point analysis, see Figure 4.16c. Based on the results the layer is plausibly cobolt oxide, which is most likely due to decomposition of CCO close to the interface with LAO. [71]

EDS mapping of the CCO-LAO junction indicates a distribution of calcium (Ca) in both the CCO and LAO phase. This is further investigated by EDS spectra of both sides of the interface. The results from this analysis can be seen in Figure 4.16. The characteristic X-rays of Ca K_α = 3.69 are visible in both the spectrum acquired from the CCO phase and the spectrum acquired from the LAO phase. The amount of Ca in the LAO phase is 8.5 wt%, compared to 16.9 wt% in the in the CMTO phase, see Table 4.3. The detection of Ca in the LAO phase is most likely contamination due to the high porosity of the ceramic, and has occurred during the polishing step before SEM analysis. This is further confirmed by the linescan shown in Figure 4.15, where the wt% of Ca detected does not decrease with distance from the interface. Thus, diffusion of Ca from the CMTO phase to the LAO phase has not occurred.

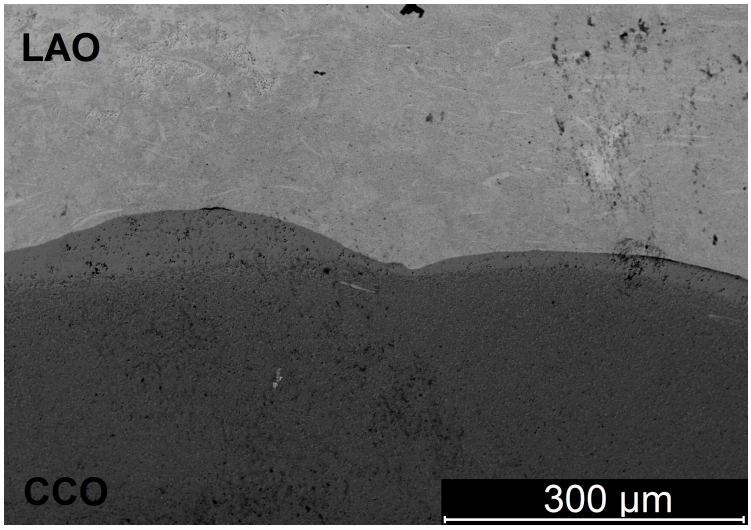

(a)

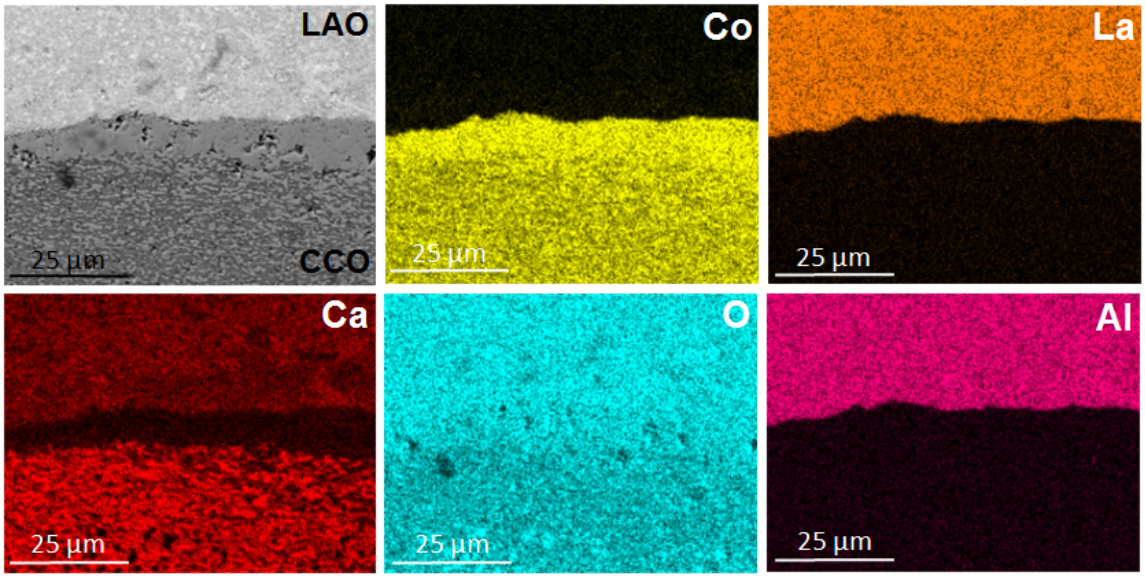

(b)

Figure 4.14: SEM images and EDS mapping of polished cross-section of diffusion couple composed of CCO and LAO sintered by SPS at 850 ℃ and 75 MPa pressure for 2 min: a) BSE image with overview of interface and b) EDS mapping of CCO-LAO junction obtained from area depicted on the BSE image. L_α detected for lanthanum (La) and K_α for calcium (Ca), cobalt (Co), aluminium (Al) and oxygen (O).

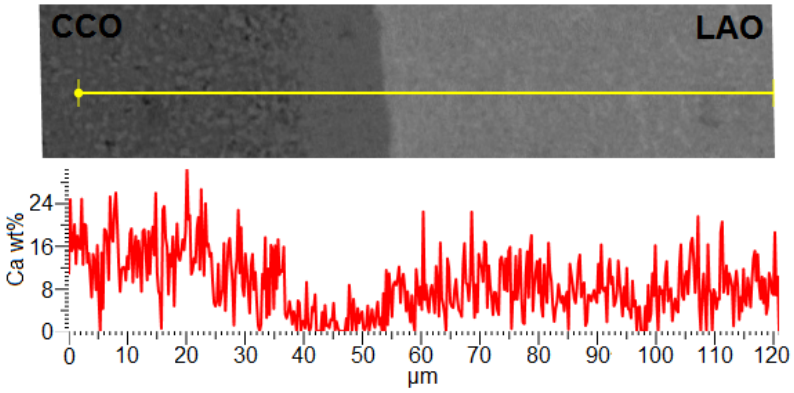

Figure 4.15: Linescan performed perpendicular to the reaction layer for the CCO-LAO diffusion couple sintered in SPS at 880 ℃ and 75 MPa for 2 min.

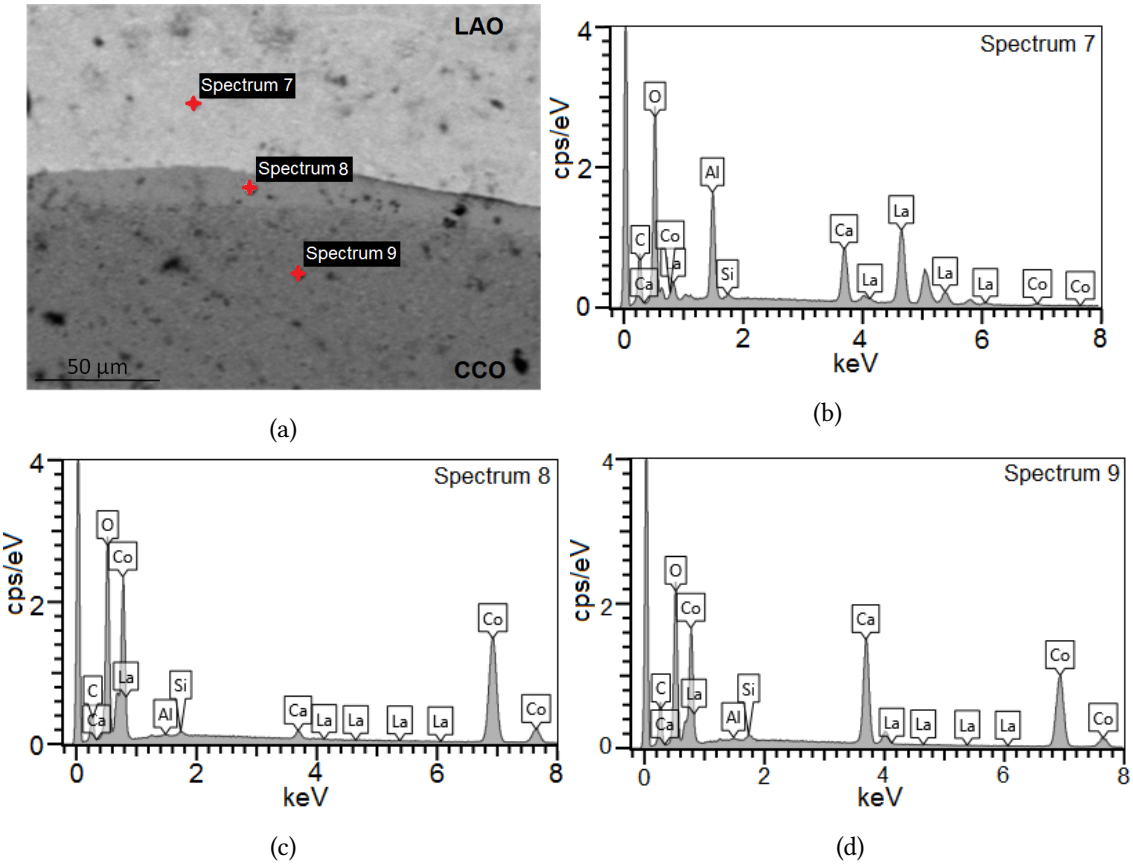

Figure 4.16: EDS point detection analysis on CCO-LAO material junction: (a) overview of where on the sample the spectra are acquired, (b) Spectrum 7, (c) Spectrum 8 and (c) Spectrum 9

Table 4.3: Weight % of Ca obtained from EDS spectra in Figure 4.16

In phase	**Spectrum**	**Wt% Ca**
LAO	Spectrum 7	8.5
Reaction layer	Spectrum 8	1.1
CCO	Spectrum 9	16.9

4.3 Processing of thermoelectric device

4.3.1 Residual stresses in multilayer systems

The processing of a thermoelectric single couple resulted in challenges with cracks in the SPS samples, especially in the CMTO phase. Therefore, a closer study the of stress development in a multilayered structure of CMTO, LAO and CCO was done. See Chapter 2.8 for detailed information. The results from this study are presented below.

Figure 4.17 shows how the stresses in the CMTO layer vary as a function of thickness of the CMTO layer and CCO layer. The calculations are based on Equation 2.20. The figure shows that the stresses in the CMTO layer decreases with increasing thickness of the layer. Also, decreasing the thickness of the CCO layer will reduce the stresses further.

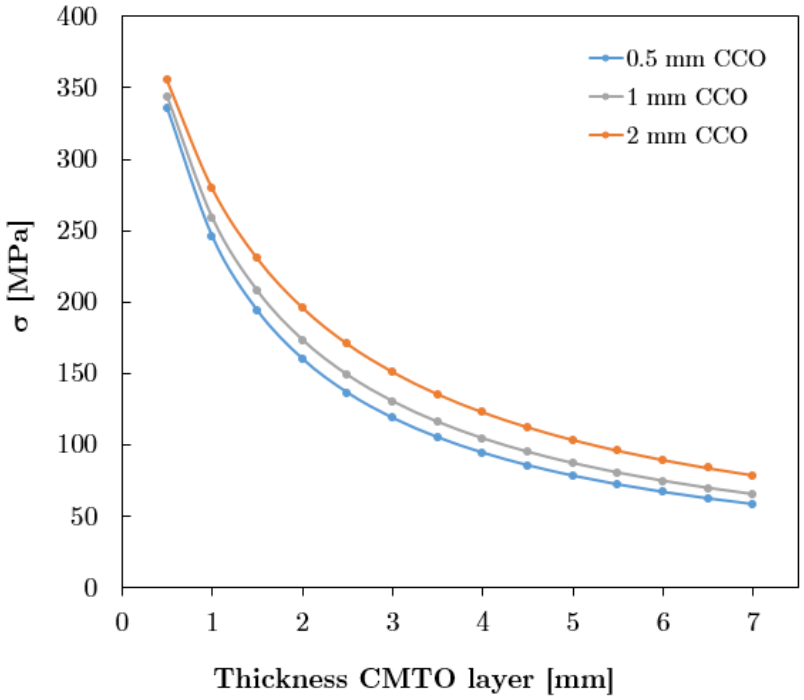

Figure 4.17: Tensile stresses developed in the CMTO layer as a function of the thickness of CMTO during cooling from 880 to 25 ℃ for three different thicknesses of CCO. The thickness of LAO is considered constant at 0.5 mm. The calculations are based on a multilayered structure illustrated in Figure 2.13.

4.3.2 Single thermoelectric couples

In this section the results obtained for thermoelectric devices prepared by SPS are presented. A number of trials were performed in order to determine the process parameters that were most beneficial for the development of a single thermoelectric couple. All tested processing routes in the SPS resulted in crack formation in the samples. A temperature of 880 ℃ and a pressure of 75 MPa was chosen as a basis for the further work.

Figure 4.18 shows SEM images of the polished cross-section of a single thermoelectric couple sintered by SPS with 2 min residence time. There are several cracks in the LAO phase which propagate through the CMTO phase. Some smaller cracks have also formed horizontally close to the pn junction (see Figure 4.18a). There are large cracks horizontally between the TE materials and insulator, but the p- and n- type materials are in good contact at the pn junction.

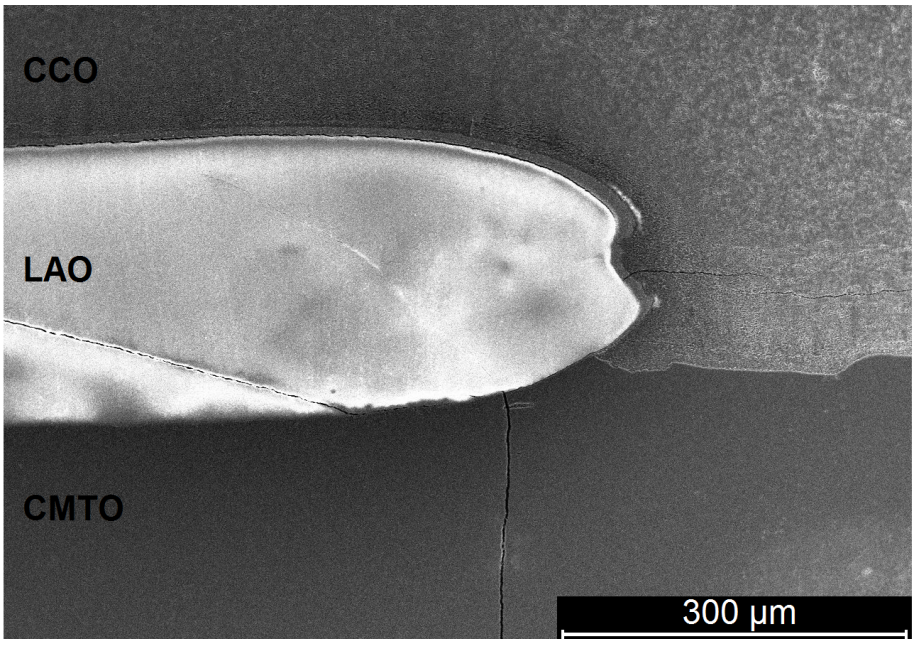

(a)

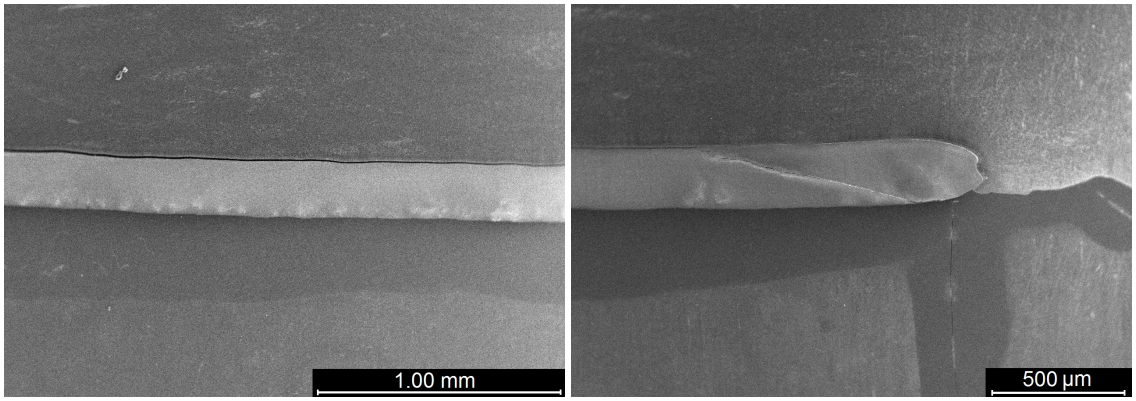

(b) (c)

Figure 4.18: SEM micrographs of the cross section of a single thermoelectric (TE) couple sintered by SPS at 880 ℃ and 75 MPa for 2 min: a) closeup of pn junction, b) overview close to the pn junction and c) overview of middle section of the TE couple.

Effect of residence time in SPS

The microstucture and the chemical compatibility between the phases were investigated using different residence time in the SPS. Figure 4.19a and 4.19b show SEM images of the microstructure of CCO in samples sintered with a residence time of 2 and 5 min respectively. Both residence times resulted in a dense CCO phase with some closed pores. No contrast between individual grains could be made visible by using SEM on the fine-polished cross-section. However, the SEM micrographs show round particles with a particle size varying up to 2 µm distributed in the CCO phase. EDS analysis and BSE imaging were used to identify the particles. The BSE image of CCO in Figure 4.19c, clearly shows different atomic number contrast. In this system it is therefore expected that the brightest phase is rich in cobalt. Point analysis was used on the particle and surrounding phase, see Figure 4.19c. The results from the point analysis in Table 4.4 confirm that the particles are rich in Co and have a much lower Ca content than the surrounding phase. The linescan in Figure 4.20 show how the Ca content drops and Co content rises abruptly in the bright particle. Comparing this to the findings of the XRD results in Figure 4.4, it is reasonable to assume the bright particles are Co_3O_4.

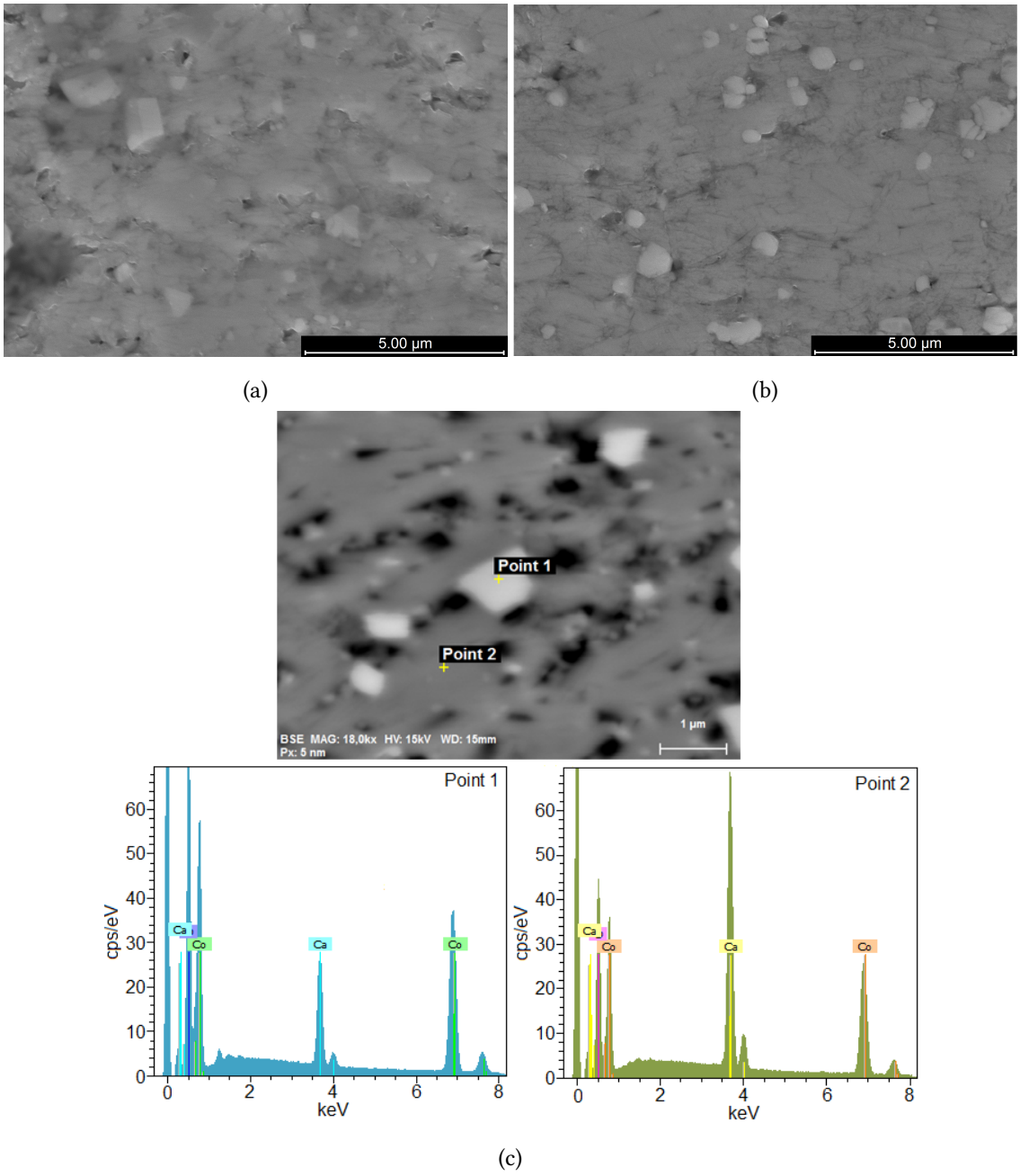

Figure 4.19: SEM micrographs and EDS analysis of CCO phase after sintering of thermoelectric couples by SPS at 880 ℃ and 75 MPa: a) 2 min residence time b) 5 min residence time and c) BSE image of CCO in sample with a residence time 2 min, along with EDS spectra obtained from point 1 and 2.

Table 4.4: Weight % of elements in CCO phase obtained from EDS spectra in Figure 4.19c.

Element	Atomic num.	Spectrum point 1 (wt%)	Spectrum point 2 (wt%)
Ca	20	8	25
Co	27	63	47
O	8	29	28

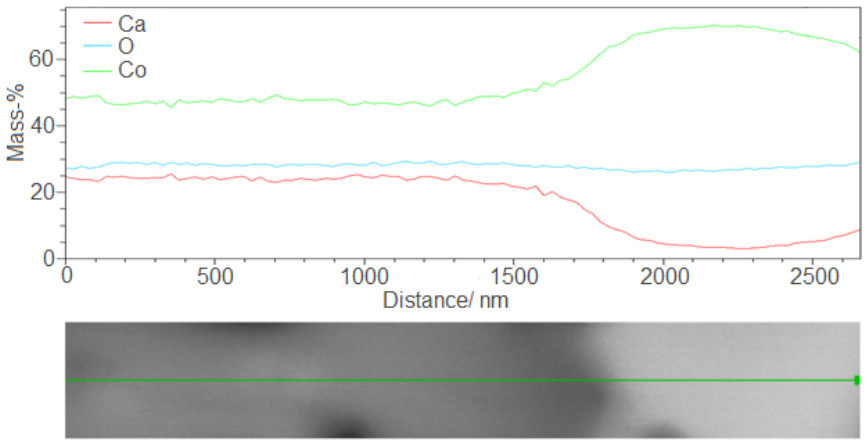

Figure 4.20: Linescan performed across particle (light grey) and matrix (dark grey) in CCO phase in thermoelectric couple sintered at 880 ℃ and 75 MPa for 2 min.

In an attempt to investigate the grain size of CCO, the fine-polished samples were chemically etched in nitric acid. The result can be seen in Figure 4.21a and 4.21b for TE couples with a residence time of 2 and 5 min respectively. After etching the layered structure of CCO is visible and both plate-like grains and rounded particles can be observed. A pronounced grain alignment perpendicular to the pressing axis is seen for both residence times. It is difficult to estimate the grain size based on the SEM micrographs, but it can be observed that the sample sintered for 5 min has slightly thicker and larger grains than the sample sintered for 2 min. In Figure 4.22, a BSE micrograph of the etched surface of the sample with a residence time of 5 min can be seen. From these results it is clear that the rounded particles seen between the plate-like CCO grains are Co_3O_4-particles, which were observed in Figure 4.19 as well.

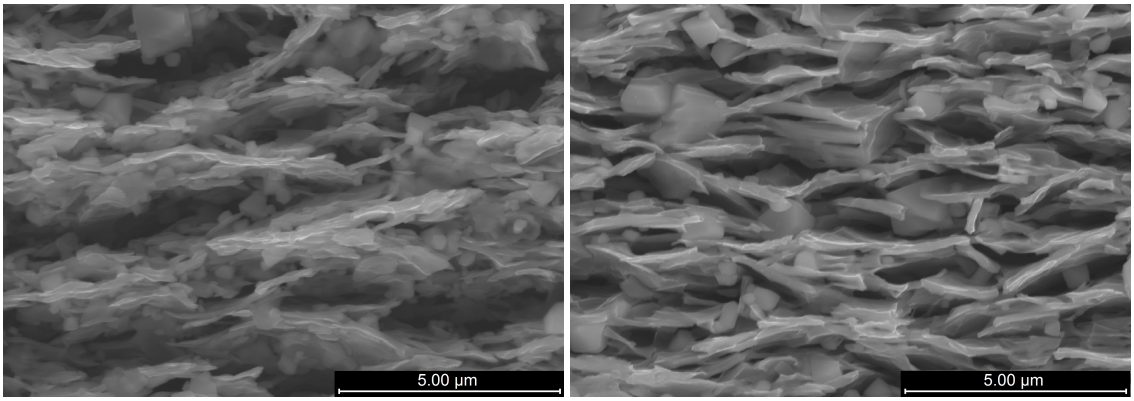

(a) (b)

Figure 4.21: SEM micrographs of etched CCO after sintering by SPS at 880 ℃ and 75 MPa: a) 2 min residence time and b) 5 min residence time. The pressing axis is perpendicular to the obtained micrographs.

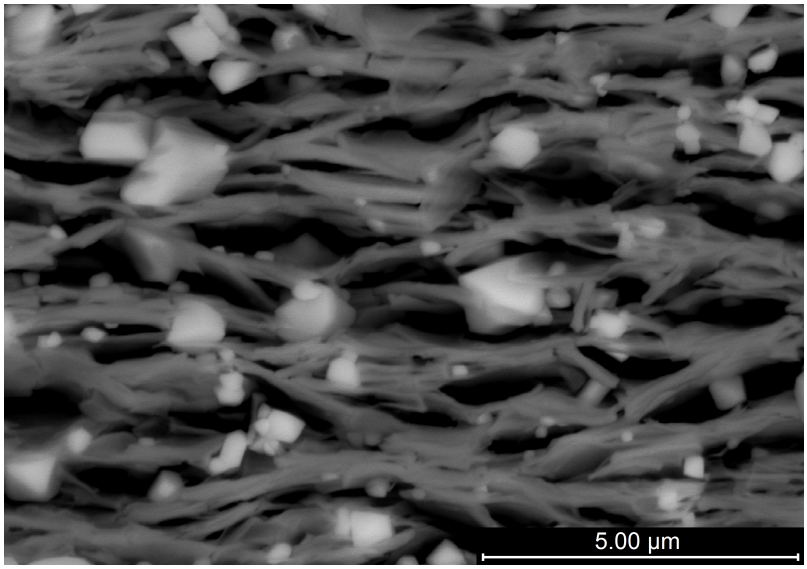

Figure 4.22: BSE micrograph of etched CCO sample sintered by SPS with residence time of 5 min at 880 ℃ and 75 MPa. The signal is obtained from the same area of the sample as the SEM image in Figure 4.21b.

In Figure 4.23, SEM images of the microstructure of LAO in samples sintered with a residence time of 2 and 5 min can be seen. From the figure it is clear that the LAO achieves a much lower density than CCO during sintering. The LAO ceramic has a high porosity and exhibits a submicron grain size for both the thermoelectric couple with a residence time of 2 min (Figure 4.23a) and the thermoelectric couple with a residence time of 5 min (Figure 4.23b). There is not any noticeable grain growth when comparing the samples with different residence time. A rough estimation of the grain size based on the SEM images is ~ 0.13 µm.

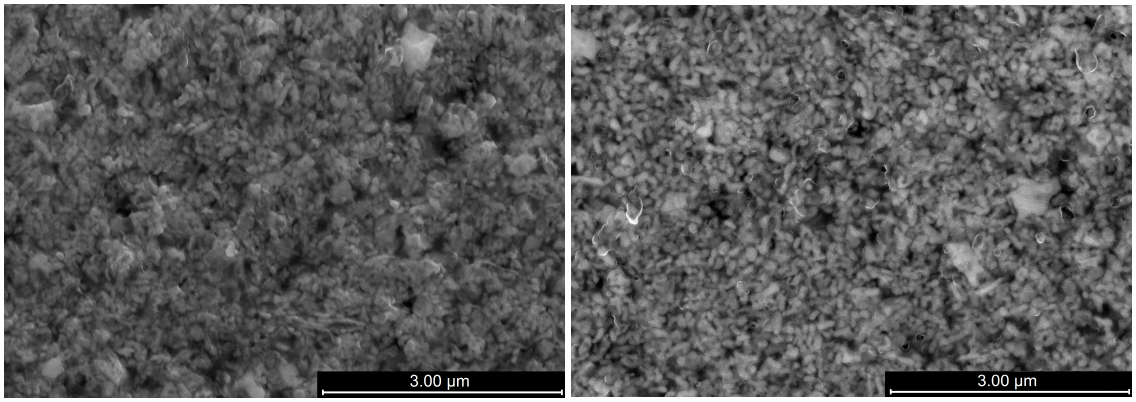

(a) (b)

Figure 4.23: SEM micrographs of LAO phase after sintering of thermoelectric couples by SPS at 880℃ and 75 MPa with: a) 2 min residence time and b) 5 min residence time.

Below, SEM images of the microstructure of CMTO in thermoelectric couples sintered with a residence time of 2 and 5 min are presented, see Figure 4.24. The CMTO ceramic also has a high porosity and interconnected pores. The grain size shows an insignificant change from 2 min (Figure 4.24a) to 5 min (Figure 4.24b) residence time. The CMTO grains are slightly larger than the LAO grains seen in Figure 4.23, but are still well below half a micron. A rough estimate gives a grain size about ~ 0.17 µm. This is slighty larger than the grain size of 0.15 µm calculated from the SEM micrograph of the fracture surface of CMTO in Figure 4.7.

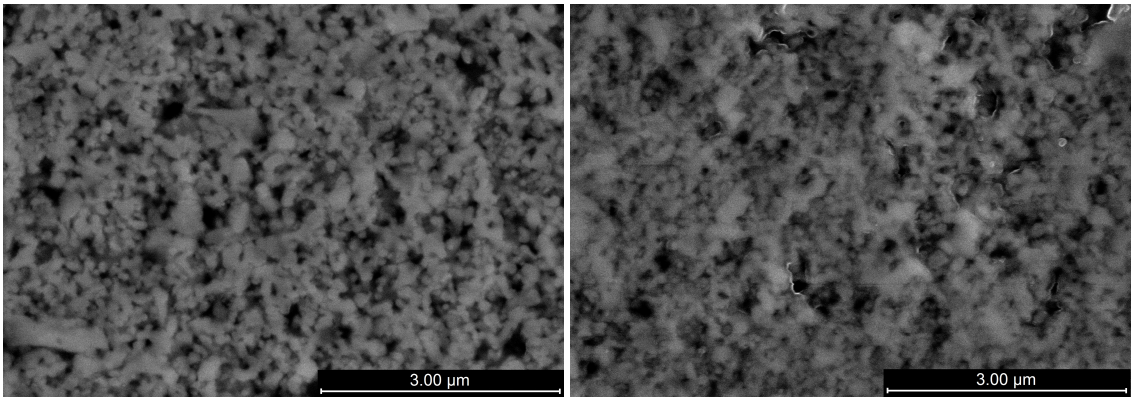

(a) (b)

Figure 4.24: SEM micrographs of CMTO phase after sintering of thermoelectric couples by SPS at 880 ℃ and 75 MPa with: a) 2 min residence time and b) 5 min residence time.

In the following sections EDS mapping of interfaces in the TE couples sintered at 880 ℃ and 75 MPa is presented. Figure 4.25 and 4.26 shows EDS mapping of the different material junctions for residence time of 2 min and 5 min respectively. Diffusion of tantalum is neglected due to the small amount present in the samples.

In this paragraph the results obtained for the TE couple sintered with 2 min residence time are presented. Figure 4.25a shows element maps obtained from the interface between CCO and LAO. From the element maps there is not any indication of a formed reaction layer at the interface between CCO and LAO. The EDS maps for calcium, aluminum, cobolt and lanthanum all show a uniform distribution close to the interface in comparison to the surrounding areas. However, EDS mapping performed at the interface between CCO and CMTO in Figure 4.25b) shows the presence of thin reaction layer. The figure shows a region at the interface between CMTO and CCO which has a high calcium content compared to the surrounding areas. This is the same phase observed in the diffusion couple sample of CCO and CMTO (Figure 4.12b), only much less pronounced. The EDS maps obtained from the interface between CMTO and LAO shows a sharp interface and no signal of interdiffusion can be assigned, see Figure 4.25c.

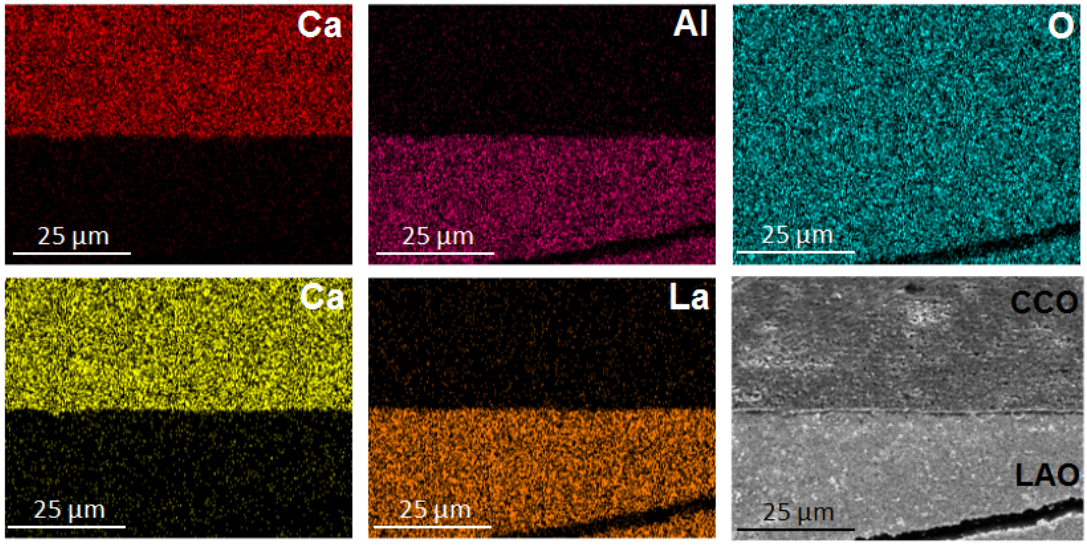
Ca
25 µm
Al
25 µm
O
25 µm
Ca
25 µm
La
25 µm
CCO
LAO
25 µm

(a)

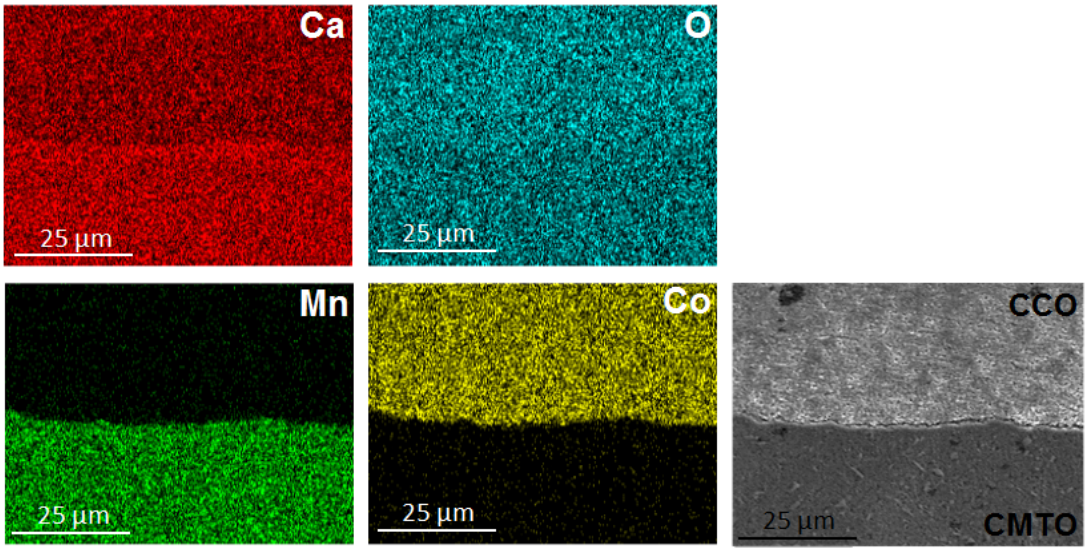
Ca
25 µm
O
25 µm
Mn
25 µm
Co
25 µm
CCO
25 µm
CMTO

(b)

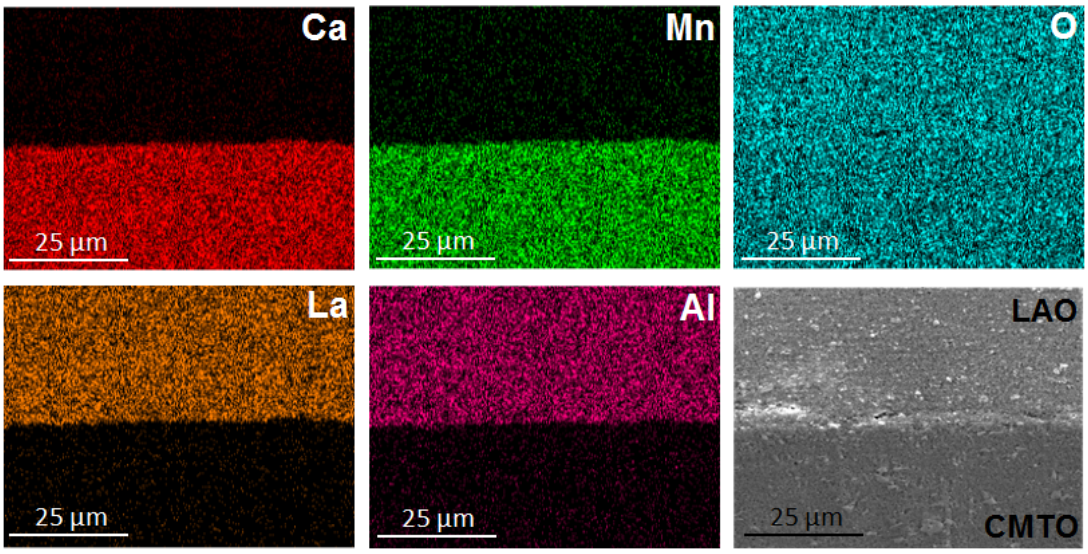

(c)

Figure 4.25: EDS mapping of material interfaces in sample sintered at 880 ℃ and 75 MPa for 2 min: a) CCO-LAO interface, b) CCO-CMTO interface and c) CMTO-LAO interface. L_α detected for lanthanum (La) and K_α for calcium (Ca), cobalt (Co), manganese (Mn), aluminum (Al) and oxygen (O).

The EDS mapping of the TE couple sintered in the SPS for 5 min (Figure 4.26) does not show the same results as the TE couple sintered for 2 min (Figure 4.25). In Figure 4.26a there is a region at the top of the LAO phase with a lower Ca content than in the CCO phase, which means that interdiffusion of Ca from CCO into the LAO phase has occurred. The reason for the difference between the samples is probably due to the different holding times. As diffusion will take time, interdiffusion of Ca is observed in the sample with the longest holding time. The diffusion couple in Figure 4.14b had a Co_3O_4-layer at the interface of CCO and LAO, but the same is not observed in the TE couples sintered for 2 and 5 min. Why this is the case is difficult to explain. The main difference between the diffusion couple and TE couples is that the diffusion couples are fabricated with LAO powder, while the TE couples are fabricated with LAO tape. The reaction area between powder-powder is larger than between powder-tape and can possibly have an effect on the decomposition of CCO. The LAO tape will have a higher density after sintering than the

LAO powder, and might also have an influence on what happens at the interface. The latter, is probably the reason why contamination of Ca in the LAO phase due to polishing only occurred in the diffusion couple.

There is not observed a reaction layer between CCO and CMTO in the TE couple sintered for 5 min (Figure 4.26b), like in the diffusion couple and the TE couple sintered for 2 min. The reason for this might be that the contact between the p- and n-type materials has been poor. From the element maps there is a small area along the interface where the signal is reduced, which means that the particles might not have been close enough to form a visible reaction layer. Except for this, no other changes in color gradient is seen.

The EDS element maps in Figure 4.26c shows a sharp interface between CMTO and LAO, and hence, there is no chemical interaction observed between CMTO and LAO in the sample sintered for 5 min either.

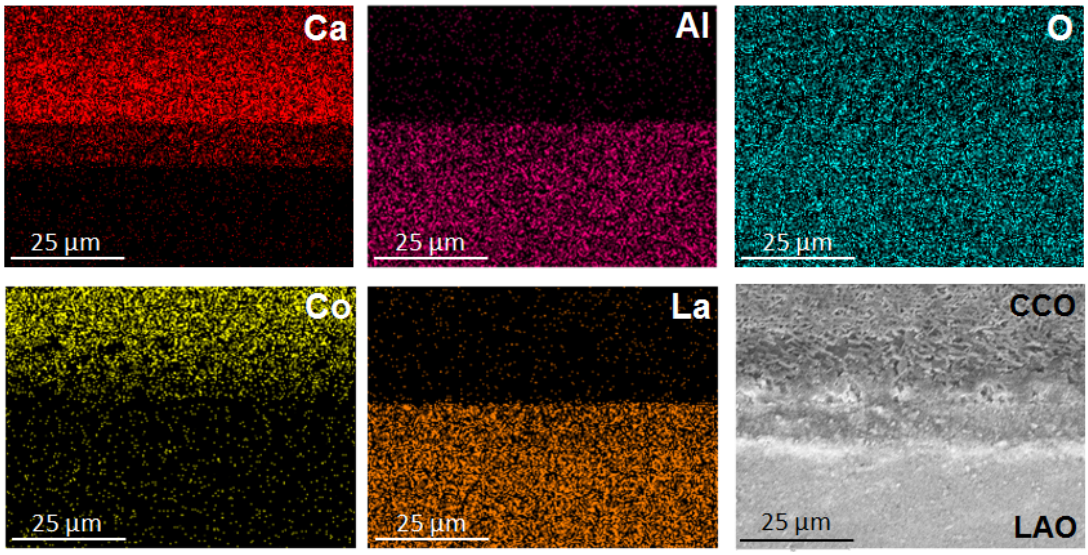

(a)

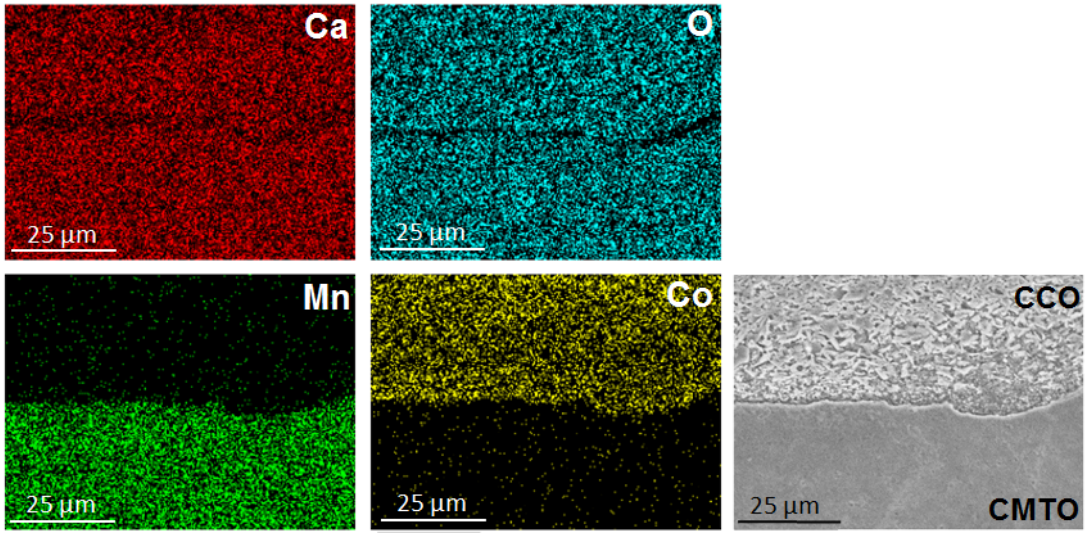

(b)

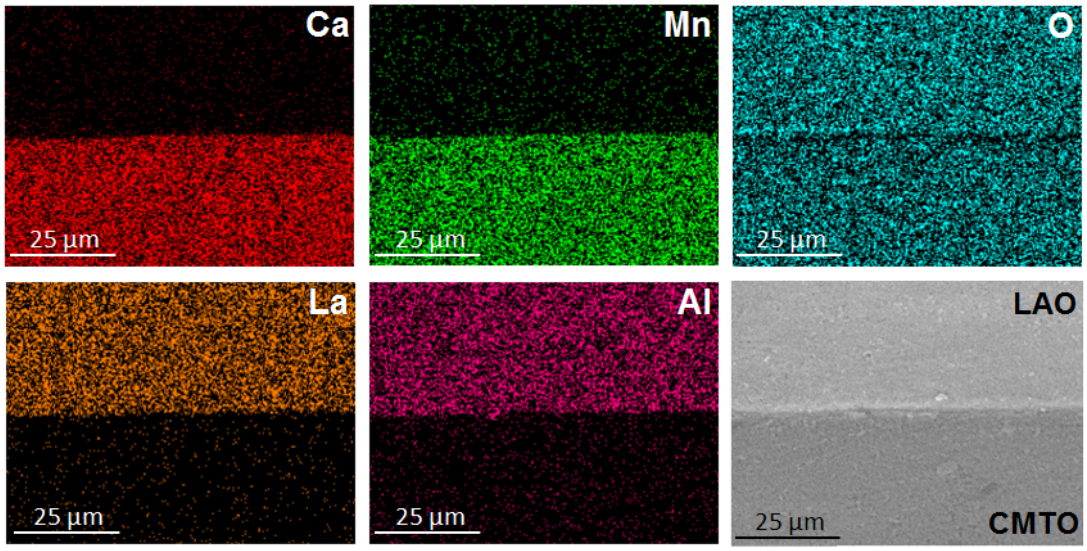

(c)

Figure 4.26: EDS mapping of material interfaces in sample sintered at 800 ℃ and 75 MPa for 2 min: a) CCO-LAO interface, b) CCO-CMTO interface and c) CMTO-LAO interface. L_α detected for lanthanum (La) and K_α for calcium (Ca), cobalt (Co), manganese (Mn), aluminum (Al) and oxygen (O).

4.3.3 Characterization of thermoelectric device

The results from characterization of the TEG are presented here. In Figure 4.27, the measured data points are fitted to continuous plots of U and P versus J. The maximum electrical power output, P_{max}, the associated electrical current, $J(P_{\text{max}})$, and voltage, $U(P_{\text{max}})$, can be estimated and read from the fitted data plots. The short-circuit current J_{SC} and open-circuit voltage U_{OC} can also be determined from Figure 4.27. The electrical resistance of the thermoelectric couple at 800 and 900 ℃ was calculated using Equation 2.8.

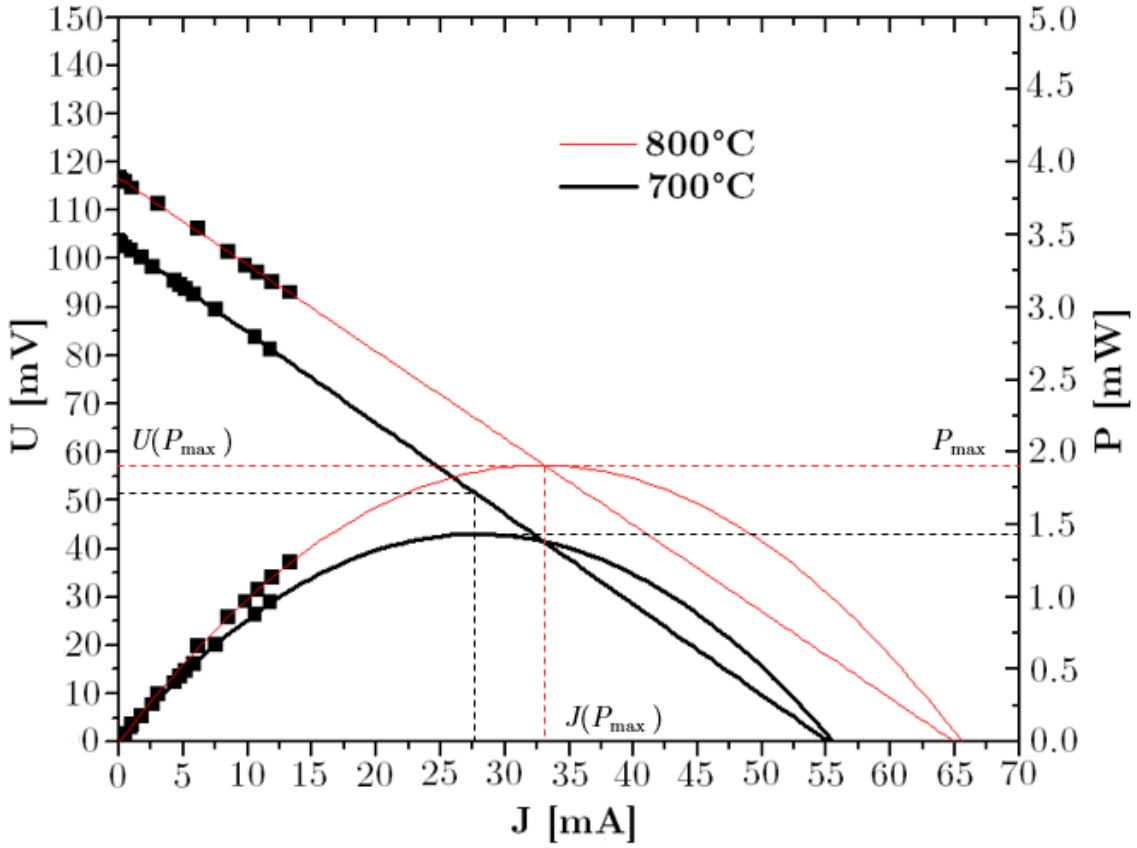

Figure 4.27: Fitted electrical power output P and voltage U as a function of the electrical current J at different applied T_{hot} temperatures (700 ℃ in black and 800 ℃ in red). $U(P_{\text{max}})$ and $J(P_{\text{max}})$ at different temperature conditions are indicated (dashed lines).

Table 4.5: Measured and calculated values of the thermoelectric couple at different temperature conditions.

T_{hot} (℃)	ΔT (℃)	U_{OC} (mV)	J_{SC} (mA)	R_{couple} (Ω)	P_{max} (mW)	$J(P_{\text{max}})$ (mA)	$U(P_{\text{max}})$ (mV)
700	100	105	56	1.90	1.45	28	52
800	100	116	66	1.77	1.90	33	56

Chapter 5

Discussion

5.1 Chemical stability

Good chemical compatibility between the materials is important for ensuring the long term stability of TE devices. The results show that co-sintering of two and two materials result in formation of product phases at the interface for two of the diffusion couples. A reaction layer is observed between CMTO and CCO at the pn-junction in Figure 4.12b. Based on previous work [72] the formed reaction layer is $Ca_3(Co_xMn_{2-x})O_6$ ($1 \leq x \leq 1.25$). There are three mobile species in the reaction, diffusion of Ca and Co from CCO into CMTO, and diffusion of Mn away from the interface. The formation of an interfacial layer indicates that the transport mechanism is surface diffusion. The thickness of the reaction layer is approximately 2.1 μm. At the interface between CCO and LAO, see Figure 4.14b and 4.14a, there is also observed a layer with a different phase composition. Based on the EDS results the phase is most likely Co_3O_4, which is due to partial decomposition of CCO. The thickness of the layer is varying and quite extensive, reaching 55 μm at the most.

The properties of the formed reaction layers will be of importance for the performance of thermoelectric device. The reaction layer formed at the pn junction will be the most detrimental to the performance of the device. If the reaction layer is non-conductive, it can stop the flow of electrons between the n- and p- type material. Experimental work [73] show that the $Ca_3(Co_xMn_{2-x})O_6$ has poor electrical conductivity when the Co/Mn ratio close to 1, see Figure 5.1.

It is therefore crucial that the reaction layer formed at the pn-junction is as thin as possible. EDS investigations of single TE couples showed a reaction layer at the pn-junction after 2 min, but not 5 min (Figure 4.25 and 4.26 respectively). Most likely there exists a reaction layer in the sample sintered for 5 min, only that the product phase domains at the interface are to small to acquire signals. The effect of residence time on the thickness of the reaction layer is therefore small. This is in accordance with previous work [72], where it was found that the thickness of the $Ca_3(Co_xMn_{2-x})O_6$ layer in conventionally sintered samples is only slightly affected by dwell time. It is proposed that the formed reaction layer works as a barrier for further reaction between the n- and p-type materials. These results are promising with respect to the operating conditions of a potential device, but it is necessary to verify the long-term stability of the pn junction under appropriate working conditions.

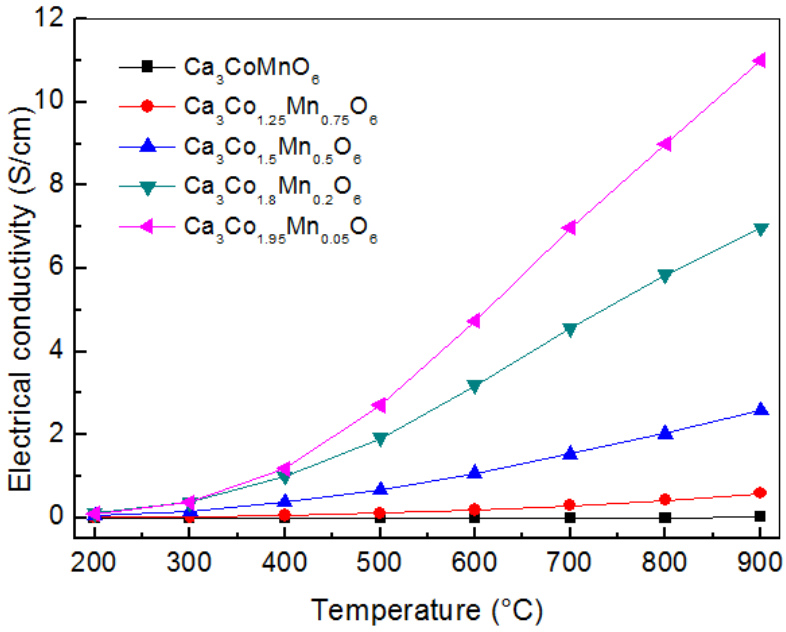

Figure 5.1: Electrical conductivity of interface compound $Ca_3(Co_xMn_{2-x})O_6$ [73].

EDS analysis of the CCO-LAO interface, gave different results for the diffusion couple and TE couples. In the diffusion couple Co_3O_4 was seen at the interface, while in the TE couples only interdiffusion of Ca into the LAO tape was seen. Considering that the device will be prepared

with LAO tape, the interdiffusion of Ca is not as cruical for the performance of the device. The interdiffusion happens into the top of the LAO tape, which means that the area of the thermoelectric material CCO is not reduced. However, a more comprehensive study of what is happening at the CCO-LAO interface should be executed. The formation of interfacial layers with different TEC than the adjacent phases can be very damaging to the device. For further work, the TEC of $Ca_3(Co_xMn_{2-x})O_6$, and possibly cobalt oxide, should be evaluated, as these layers may be present the interfaces at temperatures from 880 ℃.

The diffusion couple samples showed more chemical interaction than that found in the TE couples even though the sintering temperature was 850 ℃ compared to 880 ℃. The reason for this can be that the materials were in better contact in the diffusion couples. Only powder were used for sample preparation and the different particles can come in close contact at the interface. In sample preparation of the TE couples a fragile and stiff tape needs to be placed carefully on a powder bed and then be covered with another powder. Dips and inhomogeneities can lead to areas where the different material particles are further from each other. Another point is that the reaction area is much bigger when using powders.

5.2 Thermal and mechanical stability

Investigation of thermal properties of the materials is important in terms of evaluating the materials' adhesion and the quality of the interface contacts, for maintaining the mechanical stability of the pn assembly during formation and operation of the TE device. Thermal expansion mismatch between the materials in a TE device can cause severe stresses in the device. In systems where the device undergoes large thermal cycles, such as in automotive waste heat recovery systems, the thermal stresses can lead to degradation or breaking of the contacts between components. This can result in poor performance and even failure of the device. Hatzikraniotis et al. reported an increase in total electrical resistivity with number of thermal cycles and micro crack formation at the interface between thermoelectric pellets and interconnects. [74].

Figure 4.18 clearly shows that there are cracks in the device after sintering in the SPS. There are several possible reasons for the cracking in the samples. It is likely that the cracks are caused by stresses due to the TE mismatch between the three materials. The thermal expansion coefficients

of the materials can be seen in Table 5.1. The calculated TEC value for cooling for CCO was 13.7 $\cdot 10^{-6}$ K^{-1}, which is much lower than that recently reported by Bittner et al. (18.1 $\cdot 10^{-6}$ K^{-1}) [21]. The mismatch between CCO and CMTO is rather large with a difference of 2.2 $\cdot 10^{-6}$ K^{-1}. CCO and LAO show good compatibility in terms of thermal stability, with a mismatch of only 0.3 $\cdot 10^{-6}$ K^{-1}. The largest mismatch is seen between CMTO and LAO with a difference of 2.5 $\cdot 10^{-6}$ K^{-1}. Among the diffusion couples, this couple was the only pair that showed significant cracking, see Figure 4.12a. However, when all three materials are co-sintered, there are multiple cracks in the device, mainly in the CMTO and LAO phases. This is in good accordance with theory, the material with the highest TEC (in this case CMTO) will be in tension during cooling, and hence, most susceptible to cracking.

Table 5.1: The thermal expansion coefficient (TEC) of CMTO, LAO and CCO.

Materials	$\mathbf{TEC_{cooling}}$ **[K^{-1}]**
CMTO	15.9 $\cdot 10^{-6}$
LAO	13.4 $\cdot 10^{-6}$
CCO	13.7 $\cdot 10^{-6}$

The results are also in good agreement with the calculations presented in Section 4.3.1. Figure 5.2 show that the CMTO is in tension during cooling, but the stresses decrease with increasing thickness of CMTO. The stresses decrease exponentially, showing that the stresses in CMTO will never reach 0. The strength of the CMTO material is therefore crucial. The bending strength of CMTO has not been reported, but Noudem et al. [58] have reported the bending strength of a similar material, $Ca_{0.95}Sm_{0.05}MnO_3$, to be $\sim$ 140 MPa for a conventionally sintered (CS) sample and $\sim$ 300 MPa for a sample prepared by SPS. The tensile strength (TS) of the material can be considered to be approximately half of these values, 70 MPa and 150 MPa for samples sintered by SPS and CS respectively. An evaluation of the necessary sample thickness of CMTO can be made using these values for tensile stress as a basis. For processing purposes the thickness of the CCO layer should be above 1 mm. Presuming that the calculations in Figure 5.2 are correct, a sample thickness above 2.5 mm is sufficient to be able to resist the stresses developed during cooling in a sample sintered by SPS. However, for a conventionally sintered sample, the thickness

needs to be at least 6.5 mm. This is indicated in the figure. In this work, TE couples with a CMTO thickness of approximately 4 mm were fabricated and still showed significant cracking. It is therefore reasonable to assume that the tensile strength of CMTO is between 70-150 MPa, and most likely in the lower range. This means that the thickness of the CMTO layer needs to be somewhere above 5 mm to be able to resist the tensile stresses developed during cooling. The carbon dies used for processing in the SPS sets restrictions to the sample height, which can make processing of a TE device composed of this material system very challenging. Another consequence, which is not optimal, is that a large thickness of CMTO means a large area ratio between n- and p-type material.

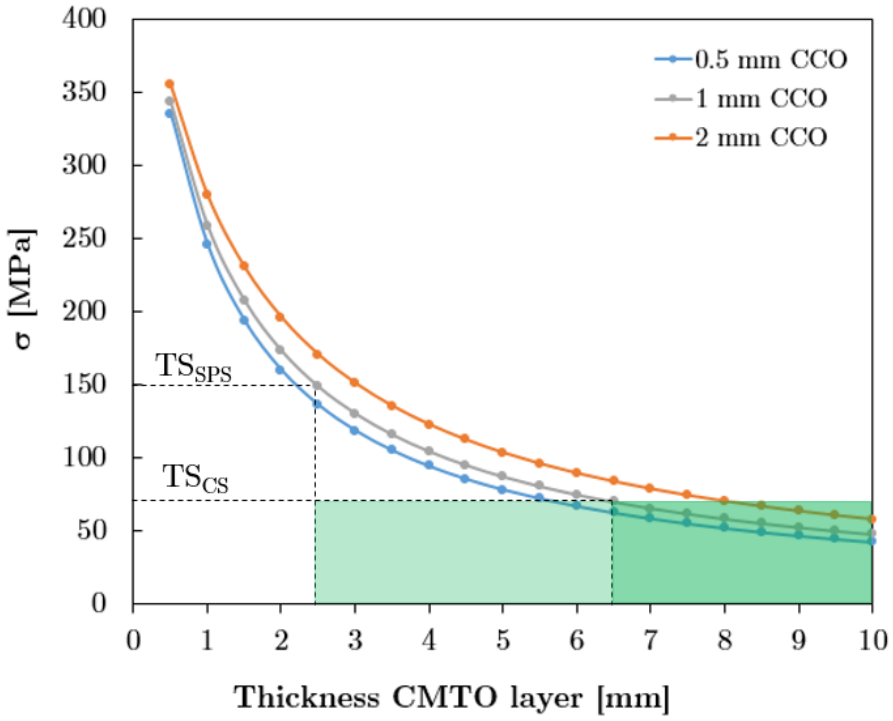

Figure 5.2: Tensile stresses developed in the CMTO layer as a function of the thickness of CMTO during cooling from 880 to 25 ℃ for three different thicknesses of CCO. The thickness of LAO is considered constant at 0.5 mm. Green areas mark thicknesses of CMTO sufficient to resist tensile stresses based on the tensile strengths of conventionally sintered samples (CS) and spark plasma sintered samples (SPS) of $Ca_{0.95}Sm_{0.05}MnO_3$[58].

One possible approach to mitigate this problem is to enhance the mechanical properties of the CMTO. Increasing the strength of CMTO will reduce the thickness necessary to resist cracking. Spark plasma sintering has been reported to significantly improve the mechanical properties of materials [58]. However, since significant cracking was seen in the devices sintered by SPS, other methods of strengthening are necessary.

Another approach is change the material system. An alternative insulator material should be considered, as the large differences in TEC between CMTO and LAO caused cracking so severe that the sintered SPS samples broke into pieces. There are several possible materials to be considered, among them MgO, $MgAl_2O_4$, several alkaline-earth perovskites and cerates. Possible insulating materials exhibiting dielectric properties are listed in Table 5.2 along with reported thermal expansion coefficient.

Table 5.2: TEC of dielectric insulators

Materials	**TEC [10^{-6} $\mathbf{K^{-1}}$]**	Temperature [K]	**Reference**
MgO	13	-	[75]
$MgAl_2O_4$	8	-	[75]
$SrTiO_3$	5	10 -150	[76]
$BaZrO_3$	7	25 - 1000	[77]
$SrZrO_3$	10	300 - 1000	[78]
$SrCeO_3$	11	300 - 1000	[78]

Using an insulator with a higher TEC than CMTO, will force the CMTO into compression and might give better results in terms of cracking. Unfortunately, insulators often have a low thermal expansion coefficient, evident from Table 5.2. The most promising alternative to LAO is MgO with a TEC of 13 K^{-1}, giving a thermal expansion mismatch with CMTO of $2.9 \cdot 10^{-6}$ K^{-1}. This is higher than the $TEC_{mismatch}$ using LAO, which means that LAO is the best fit for the CCO-CMTO system.

Another possible explanation for crack formation in the device can be stresses and strains in the materials due to changes in crystal structure. CMTO undergoes a phase transition from tetragonal to cubic above $\sim$ 896 ℃, as reported by Taguchi et al. [79]. The reducing atmosphere in

the SPS can contribute to reducing this temperature, so that the transition is happening at a lower temperature closer to 880 ℃. However, the samples sintered at 850 ℃ gave no significant improvement in terms of crack formation (no SEM images avalible) and the change in crystal structure is therefore most likely not the reason for the cracking. Also, the temperature dependence of CMTO thermal expansion in ambient atmosphere can be considered to be linear without any significant bends or breaks in the temperature range of 200 K to 900 K, as seen in Figure 4.10. The results show that the phase transitions seen in CMTO do not affect the TEC and further substantiate that the cracking is not due to phase transitions in CMTO.

Sample preparation is also a cruicial step in terms of crack formation. The sharp edges of the LAO tape can act as crack initiation sites and because completely dense packing of tape and powders is very difficult, pores and inhomogeneities in the sample can increase its susceptibility of cracking.

In addition to the cracks, the mechanical stability of the device is limited by the decomposition temperature of CCO. According to Woermann et al. [71] $Ca_3Co_4O_9$ decomposes at 926 ℃. Because of reducing conditions in the SPS machine co-sintering of the three materials is therefore performed at 880 ℃. The density of CCO is sufficient reaching a density of 95 % of theoretical value, but for LAO and CMTO a density of only 40.8 % and 68.3 % respectively is achieved (see Table 4.1). A consequence of the low sintering temperature is that the mechanical strength of the thermoelectric device is significantly reduced.

The use of TE devices in waste heat recovery sets high requirements to the robustness of the device. In operation the device will suffer large thermally induced stresses and strains, as well as thermal cycles which can cause mechanical fatigue. Satisfactory mechanical stability is therefore imperative. One of the main challenges in building an all oxide TE device is the co-sintering of three dissimilar materials. The crack formation in the samples can be detrimental to the mechanical integrity of the device. Also, the cracks can significantly reduce the electrical conductivity in the material and even result in short circuiting of the device. One of the foregoing challenges with this system will be to obtain sufficient mechanical integrity when forming a module composed of several TE couples. More knowledge on optimal processing and clever engineering is needed in order to minimize the cracking during co-sintering.

5.3 Microstructure characterization

The SEM micrographs of the CCO phase in Figure 4.19 shows a dense material with mostly isolated pores. No contrast between individual grains could be made visible by using SEM on the fine-polished cross-section. However, a prononced grain alignment was visible when investigating the fracture surface (Figure 4.6a) and chemically etched surface of CCO (Figure 4.21). This is also seen in previous work [54][80]. The grain alignment contributes to reducing the volume fraction of pores, hence improving the electrical conductivity. BSE imaging in Figure 4.22, revealed that cobolt-rich particles are distributed inside the CCO phase. The particles can be identified as Co_3O_4 based on XRD results in Figure 4.4 and are present due to the partial decomposition of CCO. As mentioned previously CCO decomposes to form CoO and $Ca_2Co_2O_6$ at 926 ℃. [71] The CoO is transformed to the more stable form of Co_3O_4 upon cooling to room temperature. There are two possible explanations for the decomposition of CCO. One is that decomposition of CCO happens at a lower temperature due to the reducing atmosphere in the SPS and the other is that the local temperature between the particles during sintering is higher than 880 ℃. Delorme et al. [81] studied the TE properties of $Ca_3Co_4O_9$-Co_3O_4 composites and found that the power factor decreases as the Co_3O_4 content increases. The Co_3O_4 phase is therefore a unwanted byproduct in the material system and a compromise needs to be made between secondary phases and achieved density.

The CMTO (Figure 4.24) and LAO (Figure 4.23) have high porosities with connected pore networks. The CMTO shows a grain size close to 0.17 µm, while the LAO grains are even smaller close to 0.13 µm. LAO ceramics are difficult to sinter below 1500 ℃ [82] and therefore little to no grain growth is observed for the sample sintered at 880 ℃ for 5 min compared to the one sintered for 2 min (see Figure 4.23). The same can be said for the CMTO phase, comparing residence time in the SPS for 2 min and 5 min does not indicate any grain growth. Ledezma [83] has reported the optimal sintering temperature of CMTO to be $\sim$ 915 ℃ according to the dilatometer curve in Figure 5.3, which is 35 ℃ higher than the temperature used in this work.

The results discussed above show good coherence with the density results presented for single material samples. The CCO ceramic obtained to the highest density, reaching 96% of theoretical density. The CMTO and LAO ceramic reaches 68 % and 41% respectively and a small grain size is therefore expected.

The density of LAO is not crucial for the performance of the device, but the the p- and n-type materials much reach sufficient density in order to benefit from their TE properties. The large number of pores will impair the electrical transport properties in the sample. The low density of LAO will however, be damaging to the mechanical stability of the device. The processing route of the TE device should be further developed in order to increase the density of CMTO and LAO in order to ensure the mechanical stability of the device.

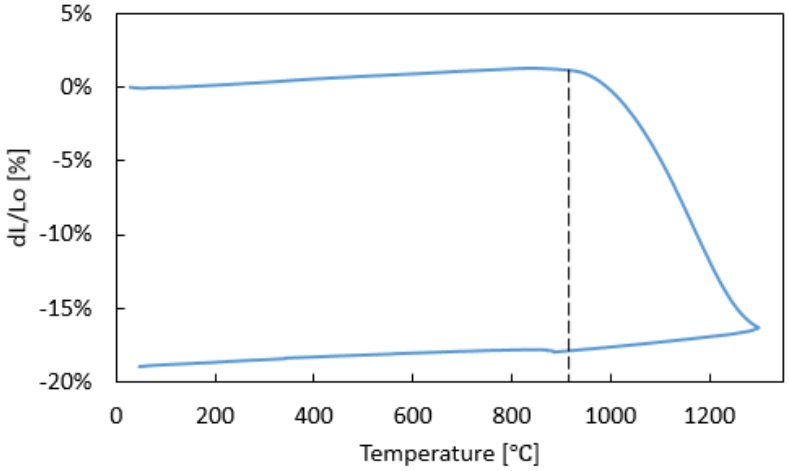

Figure 5.3: Dilatometer curve obtained for CMTO. [83].

5.4 Power output of the device

As oxide TE modules are a rather new field of research, it is difficult to compare work as processing routes, conditions and materials vary. Table 5.3 presents the number of pn couples and performance for the present oxide thermoelectric module. A selection of oxide modules studied by other researchers are also listed in Table 5.3. Most published research has been on pn couples connected by a metallic interconnector. Matsubara et al. [34] reported a generated power output of 63.5 mW under the thermal condition of hot side temperature T_{hot} = 773 ℃ and a temperature difference ΔT = 390 ℃ for a generator consisting of 8 pn couples. The utilized materials were Gd-doped $Ca_3Co_4O_9$ p-type legs and La-doped $CaMnO_3$ n-type legs, which is similar to the material used in this work. The generator fabricated by Matsubara et al. consists of several couples and

will therefore have a larger TE output. With the assumption that each couple contributes equally, a power output of 7.9 mW is achieved for one pn couple. Considering that TE couple fabricated in this work has a pn junction and no current collector, an output of 1.9 mW seems promising in terms of further development of a TE device based the CMTO-CCO system.

Table 5.3: Maximum power output of TE devices discussed in this work. More extensive information can be seen in Table 2.2.

Author	**Materials**	**pn couples**	**P_{max} [mW]**
This work	p- $Co_3Co_4O_9$ n- $Ca_{0.931}Mn_{0.98}Ta_{0.02}O_{3-\delta}$	1	1.9
Matsubara et al. [34]	p- $(Ca,Ga)_3Co_4O_9$ n- $CaMnO_3$	8	63.6
Shin et al. [10]	p- Li-doped NiO n- $BaPbO_3$	1	7.9
Feldhoff et al. [35]	p- $Ca_3Co_4O_9$ n- $Zn_{0.98}Al_{0.02}O$	5	0.55
Bittner et al. [21]	p- $Ca_3Co_4O_9$ n- $In_{1.95}Sn_{0.05}O_3$	5	4.8
Kanas [73]	p- $Co_3Co_4O_9$ n- $Ca_{0.931}MnO_{3-\delta}$	1	1.9

The first report of pn coupled oxide elements in a TE module was by Shin et al. [10] in 2001. π-shaped joints of sintered bodies of Li-doped NiO (p-type) and (Ba, Sr)PbO_3 (n-type) were fabricated. The TE performance of a single couple was 7.91 mW with the operating temperature difference of 552 K and the module consisting of four elements gave a maximum power output almost four times larger, 34.4 mW. The material system is different, but the construction of the TE couples is similar as the p- and n- type materials are connected in a junction. The measured output using CMTO and CCO is about four times less than that reported by Shin for a single couple. There are a number of possible reasons for this, but some worth highlighting is that the $Ba_xSr_{1-x}PbO_3$ solid solution is one of the best n-type oxide system reported, the temperature

difference between the hot and cold side is much larger than used for this work and the authors do not report any cracking in the π-shaped couple.

Recently Feldhoff et al. [35] measured a maximum power output of 0.55 mW utilizing p-type $Ca_3Co_4O_9$ and n-type $Zn_{0.98}Al_{0.02}O$. The single TE couple in this work with a pn junction performs about four times better than the generator fabricated by Feldhoff et al. consisting of five pn couples. Bittner et al. [21] presented work on a generator based on p- $Ca_3Co_4O_9$ and n-$In_{1.95}Sn_{0.05}O_3$ resulting in a power output of 4.8 mW, also consisting of five pn couples.

By far, the work done by Kanas [73] using a similar material system consisting of p-type $Ca_3Co_4O_9$ (CCO) and n-type $Ca_{0.931}MnO_3$ (CMO) is the best system to compare with. The TE single couple was also fabricated in a similar manner using SPS to co-sinter CMO powder, CCO powder and LAO green tape together. SPS has been reported to enhance the TE properties of materials [44], and using Kanas' work will give a more accurate basis for comparison. Cracks in the CMO phase was also observed.

A maximum power output of 0.18 mW was reported by Kanas using the same temperature conditions as in this work. See Figure 5.4. The obtained $P_{\max}$ for the CCO - CMTO system is significantly larger than that reported for the CCO - CMO system. The reason for the increased power output can be attributed to the thermoelectric properties of the n-type material. In a study by Xu et al. [31] Ta doping on the Mn-site of CMO was proven to decrease the room temperature resistivity with a order of two to three of magnitude. In general Ta-substitution affects the electrical conductivity in two ways: the large Ta-atom works as scattering centers and the carrier concentration is changed, hence improving the materials figure of merit. However, it should not be overlooked that the difference in $P_{\max}$ may be due to cracks in the device. The cracks in the devices are hard to see by the naked eye, but SEM investigations showed that the largest cracks were several micrometers wide. The number of cracks and the extent of them will vary in the different TE devices processed, and can have a large effect on the measured TE output.

Overall it can be concluded that the results for the all oxide TE module are very promising. Even with cracks in the sample and the introduction of a pn junction the module showed a P_{max} competitive to that of other oxide system. However, oxides have inferior TE properties to the conventional TE materials, so improvement of the figure of merit is needed. Doping of CCO is a possibility for this material system. Several authors have reported enhanced TE properties of

CCO by Ca-site substitution [84][85][86], Co-site substitution [87][88][89] and co-doping i.e the simultaneous substitution of both Ca and Co sites [90]. Also, efforts should be made in terms of optimization of the processing route in order to minimize cracking in the TE devices. There exists practically no previous work on the development of all oxide TE devices, and more research is necessary to further develop this very interesting field.

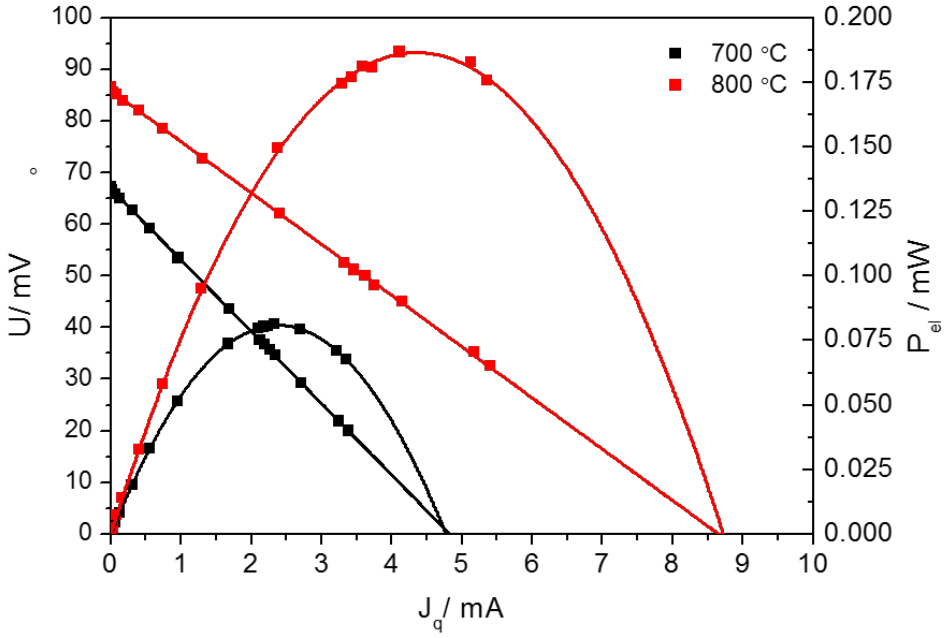

Figure 5.4: Fitted electrical power output P_{el} and voltage U as a function of the electrical current J_q at different applied T_{hot} temperatures (800 ℃ in red, 700 ℃ in black) for the $Ca_{0.931}MnO_3$ - $Ca_3Co_4O_9$ system. [73].

Chapter 6

Conclusions

An all oxide thermoelectric (TE) device consisting of n-type CMTO and p-type CCO semiconducting legs with LAO as an insulating layer in between has been successfully fabricated and characterized. This thesis describes the challenges that were posed in co-sintering the three different materials composing the single TE couple.

A novel method for fabrication of an all oxide TE device was developed. The method involves the use of the spark plasma sintering (SPS) method to co-sinter powders of CCO and CMTO with green tape of LAO. The developed method results in the formation of a pn junction and the properties of this junction will directly influence the performance of the device. Upon co-sintering at 850 ℃ and 880 ℃ chemical interaction between the materials was evident. Co-sintering p-type layered cobaltite and n-type perovskite resulted formation of a product phase $Ca_3(Co_xMn_{2-x})O_6$ ($1 \leq x \leq 1.25$) at the pn junction, while a cobolt oxide layer was formed at the interface between CCO and LAO due to decomposition of CCO.

The mechanical strength and stability of the device is limited by the sintering temperature of 880 ℃. The CCO ceramic sinters to the highest density, reaching 96% of theoretical density, while the CMTO and LAO ceramic reaches 68 % and 41% respectively. However, the CCO ceramic shows partial decomposition after SPS and a compromise must be made between density and phase purity. There were also some challenges due to thermal expansion mismatch between the materials. After sintering small cracks were observed in the samples, especially in the CMTO ceramic. The correlation between CMTO thickness and residual stresses in the sample was in-

vestigated through theoretic calculations. It was found that an increase in thickness caused a decrease in the stresses.

The device reached maximum electrical power output P_{max} = 1.9 mW at a hot-side temperature of 900 ℃ and a temperature difference of 130 ℃. P_{max} is dependent of hot side temperature and increases with increasing temperature. The present results will be helpful for development of oxide thermoelectric modules as power generation devices in the middle-to-high temperature region up to 900 ℃.

Bibliography

[1] W. R. Fahrner and S. Schwertheim. *Materials Science Foundations (monograph series) : Semiconductor Thermoelectric Generators (1).* CH: Trans Tech Publishers, 2009.

[2] Britannica Academic, Encyclopædia Britannica. *Global warming*. http://academic.eb.com/levels/collegiate/article/37044#, June 2016. Accessed 25 Sep. 2016.

[3] O. R Valmot. Enormt potensial for energisparing. *Teknisk Ukeblad*, (14):30–31, 2013.

[4] R. J. D Tilley. *Understanding Solids*. John Wiley & Sons, 2 edition, 2013.

[5] L. Han, Y. Jiang, S. Li, H. Su, Lan X., K. Qin, T. Han, H. Zhong, L. Chen, and D. Yu. High temperature thermoelectric properties and energy transfer devices of $Ca_3Co_{4-x}Ag_xO_9$ and $Ca_{1-y}Sm_yMnO_3$. *Journal of Alloys and Compounds*, 509(36):8970 – 8977, 2011.

[6] G. J Snyder and Toberer E. S. Complex thermoelectric materials. *Nature Publishing group*, 7:105–114, 2008. cited by 3825.

[7] D. M. Rowe. *CRC Handbook of Thermoelectrics*. CRC Press, 1995.

[8] D. Wang, L. Chen, Q. Wang, and J. Li. Fabrication and thermoelectric properties of $Ca_{3-x}Dy_xCo_4O_{9+\delta}$ system. *Journal of Alloys and Compounds*, 376(1-2):58–61, 2004. cited By 57.

[9] W. Wang, Y. Jiang, M. Niu, L. Wang, and B. Cao. Auto-ignition route to thermoelectric oxide $Na_xCo_2O_4$ powder with high compactibility. *Powder Technology*, 184(1):25–30, 2008. cited By 6.

[10] W. Shin, N. Murayama, K. Ikeda, and S. Sago. Thermoelectric power generation using Li-doped NiO and (Ba, Sr)PbO_3 module. *Journal of Power Sources*, 103(1):80 – 85, 2001.

[11] F.P. Zhang, X. Zhang, Q.M. Lu, J.X. Zhang, and Y.Q. Liu. Electronic structure and thermal properties of doped $CaMnO_3$ systems. *Journal of Alloys and Compounds*, 509(10):4171–4175, 2011. cited By 24.

[12] H. Ohta, K. Sugiura, and K. Koumoto. Recent progress in oxide thermoelectric materials: p-type $Ca_3Co_4O_9$ and n-type $SrTiO_3$. *Inorganic Chemistry*, 47(19):8429–8436, 2008. cited By 138.

[13] K. Wiik. NTNU, private communication, 2017.

[14] N. Mazur. *Microstructural design of $CaMnO_3$ and its thermoelectric proprieties*. Master's thesis, Norwegian University of Science and Technology, NTNU., 2015.

[15] D.M. Rowe and G. Min. Evaluation of thermoelectric modules for power generation. *Journal of Power Sources*, 73(2):193 – 198, 1998.

[16] J. H. Goldsmith. *INTRODUCTION TO THERMOELECTRICITY*. Springer, 2010.

[17] California Institute of Technology. *Brief History of Thermoelectrics*. http://www.thermoelectrics.caltech.edu/thermoelectrics/history.html#top, 2016. Accessed 9 Oct. 2016.

[18] D. M. Rowe. *Thermoelectrics handbook: macro to nano*. CRC press, 2005.

[19] S. Walia, S. Balendhran, H. Nili, S. Zhuiykov, G. Rosengarten, Q. H. Wang, M. Bhaskara, S. Sriram, M. S Strano, and K. Kalantar-zade. Transition metal oxides – thermoelectric properties. *Progress in Materials Science*, 58(8):1443 – 1489, 2013.

[20] J. P Heremans. Thermoelectricity: The ugly duckling. *Macmillan Publishers Limited*, 508:327–328, 2014.

[21] M. Bittner, B. Geppert, N. Kanas, S. P Singh, K. Wiik, and A. Feldhoff. Oxide-based thermoelectric generator for high-temperature application using p-type $Ca_3Co_4O_9$ and n-type $In_{1.95}Sn_{0.05}O_3$ legs. *Energy Harvesting and Systems*, 2016.

[22] W. M. Yim and F. D. Rosi. Compound tellurides and their alloys for peltier cooling-a review. *Solid-State Electronics*, 15:1121 – 1140, 1972.

[23] A. Nag and V. Shubha. Oxide thermoelectric materials: A structure–property relationship. *Journal of Electronic Materials*, 43(4):962–977, 2014.

[24] M. S. Dresselhaus, G. Chen, M. Y. Tang, R.G. Yang, H. Lee, D. Z. Wang, Z. F. Ren, J.P. Fleurial, and P. Gogna. New directions for low-dimensional thermoelectric materials. *Advanced Materials*, 19(8):1043–1053, 2007.

[25] D. T. Crane and L. E. Bell. Design to maximize performance of a thermoelectric power generator with a dynamic thermal power source. *J. Energy Resour. Technol.*, 131:012401–012401–8, 2009.

[26] J. He, Y. Liu, and R. Funahashi. Oxide thermoelectrics: The challenges, progress, and outlook. *Journal of Materials Research*, 26(15):1762–1772, Aug 2011.

[27] I. Terasaki, Y. Sasago, and K. Uchinokura. Large thermoelectric power in $NaCo_2O_4$ single crystals. *Phys. Rev. B*, 56:R12685–R12687, Nov 1997.

[28] K. Koumoto, R. Funahashi, E. Guilmeau, Y. Miyazaki, A. Weidenkaff, Y. Wang, and C. Wan. Thermoelectric ceramics for energy harvesting. *Journal of the American Ceramic Society*, 96(1):1–23, 2013.

[29] B. Zhan, J. Lan, Y. Liu, Y. Lin, Y. Shen, and C. Nan. High temperature thermoelectric properties of dy-doped $CaMnO_3$ ceramics. *Journal of Materials Science & Technology*, 30(8):821 – 825, 2014.

[30] Q. Zhou and B. J Kennedy. Thermal expansion and structure of orthorhombic $CaMnO_3$. *Journal of Physics and Chemistry of Solids*, 67(7):1595 – 1598, 2006.

[31] G. Xu, R. Funahashi, Q. Pu, B. Liu, R. Tao, G. Wang, and Z. Ding. High-temperature transport properties of Nb and Ta substituted $CaMnO_3$ system. *Solid State Ionics*, 171(1):147–151, 2004.

[32] Y. Zhou, I. Matsubara, R. Funahashi, G. Xu, and M. Shikano. Influence of Mn-site doped with Ru on the high-temperature thermoelectric performance of $CaMnO_{3-\delta}$. *Materials research bulletin*, 38(2):341–346, 2003.

[33] T. Paulauskas and R. F. Klie. Characterization of thermoelectric $Ca_3Co_4O_9$ microstructure using transmission electron microscopy. *Journal of Undergraduate Research*, 5(1), 2011.

[34] I. Matsubara, R. Funahashi, T. Takeuchi, S. Sodeoka, T.i Shimizu, and K. Ueno. Fabrication of an all-oxide thermoelectric power generator. *Applied Physics Letters*, 78(23):3627–3629, 2001.

[35] A. Feldhoff and B. Geppert. A high-temperature thermoelectric generator based on oxides. *Energy Harvesting and Systems*, 1(1-2):69–78, 2014.

[36] P. Tomeš, R. Robert, M. Trottmann, L. Bocher, M. H. Aguirre, A. Bitschi, J. Hejtmánek, and A. Weidenkaff. Synthesis and characterization of new ceramic thermoelectrics implemented in a thermoelectric oxide module. *Journal of Electronic Materials*, 39(9):1696–1703, 2010.

[37] S. Urata, R. Funahashi, and T. Mihara. Power generation of p-type $Ca_3Co_4O_9$/n-type $CaMnO_3$ module. In *2006 25th International Conference on Thermoelectrics*, pages 501–504, Aug 2006.

[38] R. Funahashi, M. Mikami, T. Mihara, S. Urata, and N. Ando. A portable thermoelectric-power-generating module composed of oxide devices. *Journal of Applied Physics*, 99(6), 2006.

[39] S. Choi, K. Lee, Lim C., and W. Seo. Oxide-based thermoelectric power generation module using p-type $Ca_3Co_4O_9$ and n-type $(ZnO)_7In_2O_3$ legs. *Energy Conversion and Management*, 52(1):335 – 339, 2011.

[40] T. Kuroki, K. Kabeya, K. Makino, T. Kajihara, H. Kaibe, H. Hachiuma, H. Matsuno, and A. Fujibayashi. Thermoelectric generation using waste heat in steel works. *Journal of Electronic Materials*, 43(6):2405–2410, 2014.

[41] M. Omori. Sintering, consolidation, reaction and crystal growth by the spark plasma system (sps). *Materials Science and Engineering: A*, 287(2):183 – 188, 2000.

[42] M. Tokita. Mechanism of spark plasma sintering. In *Proceeding of NEDO International Symposium on Functionally Graded Materials*, volume 22, pages 1–13. Japan, 1999.

[43] M. B. Shongwe, S. Diouf, M. O. Durowoju, and P. A. Olubambi. Effect of sintering temperature on the microstructure and mechanical properties of Fe–30% Ni alloys produced by spark plasma sintering. *Journal of Alloys and Compounds*, 649:824–832, 2015.

[44] J. Yamamoto, Y. Shimizu, H. Ohtani, K. Shiozaki, and K. Sakaki. Thermoelectric properties of fesi thermoelectric element produced by utilizing the MA/SPS process. *Journal of the Japan Society of Powder and Powder Metallurgy*, 50(11):931–936, 2003.

[45] J-F. Li, K. Wang, B-P. Zhang, and L-M. Zhang. Ferroelectric and piezoelectric properties of fine-grained $Na_{0.5}K_{0.5}NbO_3$ lead-free piezoelectric ceramics prepared by spark plasma sintering. *Journal of the American Ceramic Society*, 89(2):706–709, 2006.

[46] Y. Aman, V. Garnier, and E. Djurado. Influence of green state processes on the sintering behaviour and the subsequent optical properties of spark plasma sintered alumina. *Journal of the European Ceramic Society*, 29(16):3363–3370, 2009.

[47] J. R. Blackford. Sintering and microstructure of ice: a review. *Journal of Physics D: Applied Physics*, 40(21):R355, 2007.

[48] Z. A. Munir, U. Anselmi-Tamburini, and M. Ohyanagi. The effect of electric field and pressure on the synthesis and consolidation of materials: a review of the spark plasma sintering method. *Journal of Materials Science*, 41(3):763–777, 2006.

[49] K. R. Anderson, J. R. Groza, M. Fendorf, and C. J. Echer. Surface oxide debonding in field assisted powder sintering. *Materials Science and Engineering: A*, 270(2):278–282, 1999.

[50] M. Tokita. Development of large-size ceramic/metal bulk FGM fabricated by spark plasma sintering. In *Materials science forum*, volume 308, pages 83–88. Trans Tech Publ, 1999.

[51] G. Xie, O. Ohashi, M. Song, K. Mitsuishi, and K. Furuya. Reduction mechanism of surface oxide films and characterization of formations on pulse electric-current sintered Al–Mg alloy powders. *Applied Surface Science*, 241(1–2):102 – 106, 2005. The 9th International Symposium on Advanced Physical Fields.

[52] D. M. Hulbert, A. Anders, D. Dudina, J. Andersson, D. Jiang, C. Unuvar, U. Anselmi-Tamburini, E. J. Lavernia, and A. K. Mukherjee. The absence of plasma in "spark plasma sintering". *Journal of Applied Physics*, 104(3):033305, 2008.

[53] Z. Shen, M. Johnsson, Z. Zhao, and M. Nygren. Spark plasma sintering of alumina. *Journal of the American Ceramic Society*, 85(8):1921–1927, 2002.

[54] Y. Liu, Y. Lin, Z. Shi, C-W. Nan, and Z. Shen. Preparation of $Ca_3Co_4O_9$ and improvement of its thermoelectric properties by spark plasma sintering. *Journal of the American Ceramic Society*, 88(5):1337–1340, 2005.

[55] J. G. Noudem, D. Kenfaui, S. Quetel-Weben, C. S. Sanmathi, R. Retoux, and M. Gomina. Spark plasma sintering of n-type thermoelectric $Ca_{0.95}Sm_{0.05}MnO_3$. *Journal of the American Ceramic Society*, 94(8):2608–2612, 2011.

[56] J-F. Li, K. Wang, B-P. Zhang, and L-M. Zhang. Ferroelectric and piezoelectric properties of fine-grained $Na_{0.5}K_{0.5}NbO_3$ lead-free piezoelectric ceramics prepared by spark plasma sintering. *Journal of the American Ceramic Society*, 89(2):706–709, 2006.

[57] P. Angerer, LG. Yu, K. A. Khor, and G. Krumpel. Spark-plasma-sintering (sps) of nanostructured and submicron titanium oxide powders. *Materials Science and Engineering: A*, 381(1):16–19, 2004.

[58] J. G. Noudem, D. Kenfaui, D. Chateigner, and M. Gomina. Granular and lamellar thermoelectric oxides consolidated by spark plasma sintering. *Journal of electronic materials*, 40(5):1100–1106, 2011.

[59] W. Li, A. Feingold, P. Palanisamy, and G. Lorenz. Co-sintering zirconia electrolyte and insulator tapes for sensor applications. *Journal of the American Ceramic Society*, 95(12):3815–3820, 2012.

[60] S-H. Lee, G. L. Messing, and M. Awano. Sintering arches for cosintering camber-free sofc multilayers. *Journal of the American Ceramic Society*, 91(2):421–427, 2008.

[61] J. de Jong, N. E. Benes, G. H. Koops, and M. Wessling. Towards single step production of multi-layer inorganic hollow fibers. *Journal of Membrane Science*, 239(2):265 – 269, 2004.

[62] N. Vicente, A. Fedrizzi, N. Bazzanella, F. Casari, F. Buccioti, and A. Molinari. Microstructure of interface of SPS co-sintered and sinter bonded cp2-Ti and Co–28Cr–6Mo. *Powder Metallurgy*, 56(2):143–148, 2013.

[63] A. Mercier, K. Zehani, G. Chaplier, A. Pasko, V. Loyau, and F. Mazaleyrat. Spark plasma sintering co-sintered monolithic transformers for power electronics. *IEEE Transactions on Magnetics*, 52(5):1–4, May 2016.

[64] S. Faaland. *Heterogeneous ceramic interfaces in solid oxide fuel calls and dense oxygen permeable membranes*. PhD thesis, Norwegian University of Science and Technology, NTNU, 2000.

[65] G. Dreier and S. Schmauder. T-stress related to thermal residual stresses in bimaterials. *Scripta Metallurgica et Materialia*, 28(1):103 – 108, 1993.

[66] A. V. Virkar, J. L. Huang, and R. A. Cutler. Strengthening of oxide ceramics by transformation-induced stress. *Journal of the American Ceramic Society*, 70(3):164–170, 1987.

[67] S. Suresh, A.E. Giannakopoulos, and M. Olsson. Elastoplastic analysis of thermal cycling: Layered materials with sharp interfaces. *Journal of the Mechanics and Physics of Solids*, 42(6):979 – 1018, 1994.

[68] X. Luo and B. Wang. Structural and elastic properties of $LaAlO_3$ from first-principles calculations. *Journal of Applied Physics*, 104(7):073518, 2008.

[69] ISO 5017:2013. *Dense shaped refractory products – Determination of bulk density, apparent porosity and true porosity*, 2013. The International Organization for Standardization (ISO).

[70] A. Tok, F. Boey, and K. Khor. Tape casting of high dielectric ceramic composite substrates for microelectronics application. *Journal of Materials Processing Technology*, 89:508–512, 1999.

[71] E. Woermann and A. Muan. Phase equilibria in the system CaO-cobalt oxide in air. *Journal of Inorganic and Nuclear Chemistry*, 32(5):1455–1459, 1970. cited By 102.

[72] S. H. Kolobekken. $Ca_{0.931}Mn_{0.98}Ta_{0.02}O_{3-\delta}$-$Ca_3Co_4O_9$ *pn-junction of oxide-based thermoelectric generators for waste heat harvesting*, 2016. Specialization project, Norwegian University of Science and, NTNU.

[73] N. Kanas. Development of all-oxide ceramic thermoelectric module. THELMA project, NTNU, private communication, 2017.

[74] E. Hatzikraniotis, K. T. Zorbas, I. Samaras, Th. Kyratsi, and K. M. Paraskevopoulos. Efficiency study of a commercial thermoelectric power generator (teg) under thermal cycling. *Journal of Electronic Material*, 39(9):2112–2116, 2010.

[75] F. Kennard, R. Bradt, and V. Stubican. Mechanical properties of the directionally solidified mgo-mgal2o4 eutectic. *Journal of the American Ceramic Society*, 59(3-4):160–163, 1976.

[76] S. Tsunekawa, H. F. J. Watanabe, and H. Takei. Linear thermal expansion of $SrTiO_3$. *physica status solidi (a)*, 83(2):467–472, 1984.

[77] S. Yamanaka, K. Kurosaki, T. Maekawa, T. Matsuda, Kobayashi S-I, and M. Uno. Thermochemical and thermophysical properties of alkaline-earth perovskites. *Journal of Nuclear Materials*, 344(1–3):61 – 66, 2005. Proceedings of the 11th International Symposium on Thermodynamics of Nuclear Materials.

[78] S. Yamanaka, K. Kurosaki, T. Oyama, H. Muta, M. Uno, T. Matsuda, and S-I. Kobayashi. Thermophysical properties of perovskite-type strontium cerate and zirconate. *Journal of the American Ceramic Society*, 88(6):1496–1499, 2005.

[79] H. Taguchi, M. Nagao, T. Sato, and M. Shimada. High-temperature phase transition of $CaMnO_{3-\delta}$. *Journal of Solid State Chemistry*, 78(2):312–315, 1989.

[80] J. G. Noudem, M. Prevel, A. Veres, D. Chateigner, and J. Galy. Thermoelectric $Ca_3Co_4O_9$ ceramics consolidated by spark plasma sintering. *Journal of electroceramics*, 22(1-3):91–97, 2009.

[81] F. Delorme, P. Diaz-Chao, E. Guilmeau, and F. Giovannelli. Thermoelectric properties of $Ca_3Co_4O_9$-Co_3O_4 composites. *Ceramics International*, 41(8):10038–10043, 2015.

[82] C-L. Huang, R-J. Lin, and H-L. Chen. Microwave dielectric properties and microstructures of CuO- and ZnO-doped $LaAlO_3$ ceramics. *Materials Research Bulletin*, 37(3):449 – 457, 2002.

[83] K. Ledezma. Sintering and thermoelectric properties of $Ca_{0.931}Mn_{0.98}Ta_{0.02}O_{3-\delta}$, 2016. Specialization project, Norwegian University of Science and, NTNU.

[84] Y. Wang, L. Xu, Y. Sui, X. Wang, J. Cheng, and W. Su. Enhanced electron correlation in rare-earth doped $Ca_3Co_4O_9$. *Applied Physics Letters*, 97(6):062114, 2010.

[85] G. Tang, Z. H. Wang, X. N. Xu, L. Qiu, and Y. W. Du. Evidence of spin-density-wave transition and enhanced thermoelectric properties in $Ca_{3-x}Ce_xCo_4O_{9+\delta}$. *Journal of Applied Physics*, 107(5):053715, 2010.

[86] S. Li, R. Funahashi, I. Matsubara, K. Ueno, S. Sodeoka, and H. Yamada. Synthesis and thermoelectric properties of the new oxide materials $Ca_{3-x}Bi_xCo_4O_{9+\delta}$ ($0.0 < x < 0.75$). *Chemistry of materials*, 12(8):2424–2427, 2000.

[87] Y. Wang, Y. Sui, X. Wang, W. Su, and X Liu. Enhanced high temperature thermoelectric characteristics of transition metals doped $Ca_3Co_4O_{9+\delta}$ by cold high-pressure fabrication. *Journal of Applied Physics*, 107(3):033708, 2010.

[88] B. C. Zhao, Y. P. Sun, and W. H. Song. Magnetic and transport properties in the Ti doped cobaltite $Ca_3Co_{4-x}Ti_xO_9$ ($0 \leqslant x \leqslant 0.8$) single crystals. *Journal of applied physics*, 99(7):073906, 2006.

[89] L. Xu, F. Li, and Y. Wang. High-temperature transport and thermoelectric properties of $Ca_3Co_{4-x}Ti_xO_9$. *Journal of Alloys and Compounds*, 501(1):115–119, 2010.

[90] W. Yang, H. Qian, J. Gan, W. Wei, Z. Wang, and G. Tang. Effects of Lu and Ni substitution on thermoelectric properties of $Ca_3Co_4O_{9+\delta}$. *Journal of Electronic Materials*, 45(8):4171–4176, 2016.

Appendices

Appendix A

Calculation of density

The density of CCO, LAO and CMTO was calculated using Archimedes method. The bulk density was calculated from:

$$\rho_b = \frac{m_1}{m_3 - m_2} \cdot \rho_{liq} \tag{A.1}$$

where m_1 is the mass of the dry pellet, m_2 in the mass of the pellet immersed in isopropanol, m_3 is the mass of the pellet wetted in isopropanol and ρ_{liq} is the density on the immersion liquid, in this case isopropanol.

The open porosity (vol%) was calculated from:

$$\pi_a = \frac{m_3 - m_1}{m_3 - m_2} \cdot 100 \tag{A.2}$$

and the true porosity (vol%) from:

$$\pi_t = \frac{\rho_t - \rho_b}{\rho_t} \cdot 100 \tag{A.3}$$

where ρ_t in the theoretical density of the material.

Table A.1: The density calculations in this work are based on the following obtained masses and temperatures of isopropanol.

Material	$\mathbf{m}_1$ **[g]**	$\mathbf{m}_2$ **[g]**	$\mathbf{m}_3$ **[g]**	T_{iso} [℃]
CMTO	0.7678	0.6335	0.8217	17.1
CCO	0.6521	0.5384	0.6529	17.0
LAO	0.5197	0.4532	0.6072	16.2